THÈSE DE DOCTORAT

Présentée à

L'UNIVERSITÉ DE LILLE



L'école doctorale: ENGSYS Sciences de l'ingénierie et des systèmes

L'unité de recherche: CNRS-IEMN

Dans la spécialité: Micro-nanosystèmes et Capteurs

par

Zhihao Wu

Design and Scalable Fabrication of High-Performance Flexible Micro-Supercapacitors via Laser Processing and Defect Engineering

Conception et fabrication de microsupercondensateurs flexibles haute performance par traitement laser et ingénierie des défauts

Soutenue le 22 Septembre 2025 devant le composé de:

Dr. Mihaela BAIBARAC	Rapporteur	National Institute of Materials Physics
Dr. Manjusha SHELKE	Rapporteur	National Chemical Laboratory
Prof. Sorin MELINTE	Examinateur	Universite Catholique de Louvain
Prof. Yamin LEPRINCE-WANG	Examinateur	Université Gustave Eiffel
Prof. Henri HAPPY	Président du jury	Université de Lille, CNRS-IEMN
Dr. Rabah Boukherroub	Directeur de thèse	Université de Lille, CNRS-IEMN
Prof. Sabine Szunerits	Co-directeurs de thèse	Université de Lille, CNRS-IEMN

Abstract **6**
Résumé **9**
Acknowledgments **12**
General introduction **14**
Chapter I. Introduction **18**
I.1. Introduction (Background) 18
I.2. Development and Evolution of Supercapacitors 19
I.2.1. Types of Supercapacitors 21
I.2.1.1. Electric Double-Layer Capacitors (EDLCs) 22
I.2.1.2. Pseudocapacitors 23
I.2.1.3. Hybrid Supercapacitors 23
I.2.2. Charge Storage Mechanisms 24
I.3. Typical Fabrication Techniques for Supercapacitors 26
I.3.1. Laser-Induced Graphene (LIG) Technique 27
I.3.2. Printing Technologies 27
I.3.3. Electrochemical Synthesis 28
I.3.4. Solution-Based and Sol–Gel Methods 28
I.3.5. Hydrothermal/Solvothermal Synthesis 28
I.3.6. Vapor-Phase Deposition (CVD, ALD) 29
I.4. Electrode Materials 30
I.4.1. Carbon-Based Materials 30
I.4.1.1. Carbon Nanotubes (CNTs) 31
I.4.1.2. Graphene 32
I.4.1.3. Carbon Nanofibers (CNFs) 35
I.4.2. MXenes 36
I.4.3. Conductive Polymers 39
I.4.4. Transition Metal Oxides and Hydroxides 41
I.4.4.1. Ruthenium Dioxide (RuO_2) 42
I.4.4.2. Manganese Dioxide (MnO_2) 43

I.4.4.3. Layered Double Hydroxides (LDHs) 44
I.5. Opportunities and Challenges....46
I.6. Objectives 47
References....48
Chapter II. Materials and Characterization Techniques....59
II.1. Reagents and Materials 59
II.2. Instrumentation....59
II.2.1 CO_2 Laser Processing System 59
II.2.2 Freeze Dryer....61
II.3. Characterization 62
II.3.1 Scanning Electron Microscopy (SEM) 62
II.3.2 Transmission Electron Microscopy (TEM)....63
II.3.3 X-ray Diffraction (XRD)....64
II.3.4 X-ray Photoelectron Spectroscopy (XPS)....67
II.3.5 Contact Angle Measurements 69
II.3.6 Electrical Conductivity Measurements 70
II.4. Electrochemical Performance Parameters....71
II.4.1. Electrode and Electrolyte 72
II.4.2. Cyclic Voltammetry (CV)....73
II.4.3. Galvanostatic Charge–Discharge (GCD)....74
II.4.4. Electrochemical Impedance Spectroscopy (EIS) 75
II.4.4. Ragone Plot Analysis 76
II.4.5. Cycling Stability Evaluation 77
References....78
Chapter III: Mask-Assisted Spray Deposition of Additive-Free MXene on Laser-Induced Graphene for Flexible Symmetric Micro-Supercapacitors....79
III.1. Abstract....79
III.2. Introduction....80
III.3. Experimental Section....82
III.3.1. Experimental Materials....82
III.3.2. Preparation of Delaminated Multilayer $Ti_3C_2T_x$ (D-MXene) 83

III.3.3. Preparation of Few-Layer $Ti_3C_2T_x$ Nanosheets (FL-MXene).....83
III.3.4. Fabrication of Flexible Symmetric MXene Micro-Supercapacitors.....83
III.3.4.1. Preparation and Patterning of Laser-Induced Graphene (LIG).....83
III.3.4.2. Preparation of Gel Electrolyte 84
III.3.4.3. Assembly of MXene-Based Symmetric Micro-Supercapacitors.....84
III.3.5. Material Characterization.....85
III.3.6. Electrochemical Characterization 86
III.4. Results and Discussion 87
III.4.1. Fabrication of Flexible Symmetric MXene-Based Micro-Supercapacitors...87
III.4.2. Morphological and Structural Characterization.....90
III.4.3. Patterning and Electrode Configuration.....93
III.4.4. Electrochemical Performance 98
III.4.5. Application Demonstration of MXene-Based MSCs 105
III.5. Conclusion 110
References.....111
Chapter IV: High-Performance Flexible Micro-Supercapacitors Based on Laser-Induced Graphene Integrated with Hydrogen Vacancy-Rich CoNi Layer Double Hydroxide 116
IV.1. Abstract.....116
IV.2. Introduction.....117
IV.3. Experimental Section.....121
IV.3.1. Fabrication of LIG-CoNi-$LDH_{(v)}$//LIG-FeOOH AMSC 121
IV.3.1.1. Synthesis and fabrication of laser-induced graphene (LIG) 121
IV.3.1.2. Preparation of LIG-CoNi-LDH 121
IV.3.1.3. Electrochemical activation of LIG-CoNi-LDH (LIG-CoNi-$LDH_{(v)}$)122
IV.3.1.4. Fabrication of LIG-FeOOH 122
IV.3.1.5. Fabrication of flexible asymmetric micro-supercapacitor (AMSC).122
IV.3.2. Electrochemical Characterization.....123
IV.4. Results and Discussion 127
IV.5. Conclusion 153
References.....154

Chapter V: Conclusions and Perspectives 161
V.1 Conclusions 161
V.2 Perspectives 163
Publications 165

Abstract

The rapid development of renewable energy technologies necessitates efficient energy storage systems to address the intermittent and unstable nature of solar and wind energy sources. Among emerging storage solutions, micro-supercapacitors (MSCs) stand out as promising candidates for next-generation miniaturized energy storage devices, due to their superior power density and cycling stability. My thesis work is focused on the design and characterization of high performance and flexible micro-supercapacitors through cost-effective approaches.

Chapter I introduces the fundamental mechanisms of supercapacitors, methodologies for synthesizing nano- and micro-structured supercapacitors, and a concise overview of active electrode materials along with their intrinsic properties. Recent strategies aimed at enhancing the power density, energy density, and cycling stability of supercapacitors are also reviewed. To address existing challenges, I have analyzed and proposed key solutions including the integration of laser processing and mask-assisted spray-coating techniques, enabling scalable and diversified production of supercapacitors. Additionally, defect engineering (hydrogen vacancies) was employed to enhance the electrochemical performance of active materials, consequently improving the energy density of supercapacitors.

Chapter II details the experimental procedures and characterization techniques employed throughout the research.

Chapter III presents the fabrication of flexible planar MSCs based on MXene using a mask-assisted spray-coating method coupled with laser processing. Utilizing cost-effective and scalable laser techniques, porous interdigitated laser-induced graphene (LIG) structures were successfully constructed on polyimide substrates. The ease and versatility of spray-coating enabled rapid fabrication of MXene-based supercapacitors on various substrates and large-scale production of MSC arrays to meet practical demands. Notably, the additive-free MXene ink formulation, containing no binary solvent systems, offered environmentally friendly characteristics with excellent electrochemical performance at milligram-scale MXene loadings. This versatile direct ink spraying technique highlights the significant potential of additive-free MXene inks for scalable production and integration into printed electronic components.

Chapter IV introduces an innovative asymmetric micro-supercapacitor (AMSC) design employing laser-induced graphene electrodes functionalized with hydrogen vacancy-rich cobalt-nickel layered double hydroxide (CoNi-$LDH_{(v)}$). Cost-effective laser processing and electrodeposition techniques were combined to create porous interdigitated LIG structures functionalized with CoNi-$LDH_{(v)}$ as cathode and FeOOH as anode materials. The resulting LIG-CoNi-$LDH_{(v)}$//LIG-FeOOH AMSCs demonstrated enhanced electrochemical properties, including a wide operating voltage window (0-1.8 V) in PVA/LiCl gel electrolyte, superior areal capacitance of 38.28 mF cm^{-2}, volumetric capacitance of 5.60 F cm^{-3} at 0.25 mA cm^{-2}, robust mechanical durability, and remarkable cycling stability with 92% capacitance retention over 10,000 cycles. Furthermore, the device exhibited excellent compatibility with various cations (Li^+, Na^+, K^+, and Ca^{2+}) in neutral electrolytes. Integration with solar cells and commercial LED

devices demonstrated practical feasibility for flexible, self-powered electronics. This research provides promising avenues for enhancing MSC performance via defect engineering and hybrid materials integration, promoting scalable and economically viable energy storage solutions.

Résumé

Le développement rapide des technologies d'énergie renouvelable nécessite des systèmes de stockage d'énergie efficaces pour remédier à la nature intermittente et instable des sources d'énergie solaire et éolienne. Parmi les solutions de stockage émergentes, les micro-supercondensateurs (MSCs) se distinguent comme des candidats prometteurs pour les dispositifs de stockage d'énergie miniaturisés de la prochaine génération en raison de leur densité de puissance et de leur grande stabilité. Mon travail de thèse porte sur la conception et la caractérisation de micro-supercondensateurs flexibles et performants en utilisant des approches simples et bas coût.

Le chapitre I présente les mécanismes fondamentaux des supercondensateurs, les méthodes de synthèse des supercondensateurs nanostructurés et microstructurés, ainsi qu'un aperçu concis des matériaux d'électrodes actives et de leurs propriétés intrinsèques. Les stratégies récentes visant à améliorer la densité de puissance, la densité d'énergie et la stabilité des cycles des supercondensateurs sont également passées en revue. Pour relever les défis actuels, j'ai analysé et proposé des solutions clés, notamment l'intégration du traitement laser et des techniques d'enduction par pulvérisation assistée par masque, permettant une production diversifiée de supercondensateurs. De plus, l'ingénierie des défauts (défauts d'hydrogène) a été utilisée pour améliorer les performances électrochimiques des matériaux actifs, ce qui a permis d’augmenter la densité énergétique des supercondensateurs.

Le chapitre II détaille les procédures expérimentales et les techniques de caractérisation utilisées pour la réalisation de mon travail de thèse.

Le chapitre III décrit la fabrication de MSC planaires flexibles à base de MXènes à l'aide d'une méthode de revêtement par pulvérisation assistée par masque couplée à un traitement laser. En utilisant des techniques laser, des structures poreuses interdigitées de graphène induit par laser (LIG) ont été obtenues avec succès sur des substrats de polyimide. La facilité et la polyvalence de l'enduction par pulvérisation ont permis la fabrication rapide de supercondensateurs à base de MXènes sur divers substrats et la production à grande échelle de réseaux de MSCs pour répondre aux demandes pratiques. Notamment, la formulation de l'encre au MXène sans additif, ne contenant aucun système de solvant binaire, présentait des caractéristiques respectueuses de l'environnement avec d'excellentes performances électrochimiques à des charges de MXène de l'ordre du milligramme. Cette technique polyvalente de pulvérisation directe d'encre met en évidence le potentiel significatif des encres au MXène sans additif pour une production à la carte et une intégration dans les composants électroniques imprimés.

Le chapitre IV présente une conception innovante d'un micro-supercondensateur asymétrique (AMSC) à base d'électrodes de graphène (LIG) fonctionnalisées avec de l'hydroxyde double stratifié cobalt-nickel (CoNi-$LDH_{(v)}$) riche en défauts d'hydrogène. Des techniques de traitement laser et d'électrodéposition ont été combinées pour créer des structures LIG interdigitées poreuses fonctionnalisées avec du CoNi-$LDH_{(v)}$ comme cathode et du FeOOH comme anode. Les AMSCs LIG-CoNi-$LDH_{(v)}$//LIG-FeOOH qui en résultent présentent des propriétés électrochimiques améliorées, notamment une large fenêtre de tension de fonctionnement (0-1,8 V) dans l'électrolyte gel PVA/LiCl, une

capacité surfacique supérieure de 38,28 mF cm^{-2}, une capacité volumétrique de 5,60 F cm^{-3} à 0,25 mA cm^{-2}, une durabilité mécanique robuste et une bonne stabilité avec une rétention de capacité de 92 % sur 10 000 cycles. En outre, le dispositif présente une excellente compatibilité avec divers cations (Li^+, Na^+, K^+ et Ca^{2+}) dans des électrolytes neutres. L'intégration avec des cellules solaires et des dispositifs LED commerciaux a démontré la faisabilité pratique d'une électronique flexible et auto-alimentée. Cette recherche offre des pistes prometteuses pour l'amélioration des performances des MSCs via l'ingénierie des défauts et l'intégration de matériaux hybrides, favorisant ainsi des solutions de stockage d'énergie évolutives et économiquement viables.

Acknowledgments

This doctoral research was conducted at the Institute of Electronics, Microelectronics and Nanotechnology (IEMN), within the Nano-BioInterfaces (NBI) group. During this period, I also had the opportunity to engage in academic exchange at the International Joint Laboratory for Micro/Nano Manufacturing and Measurement Technologies at Xi'an Jiaotong University (China). Though three years may seem brief in the grand scheme of life, they have been among the most unforgettable and valuable years of my journey. During this time, I experienced significant growth in my research and innovation capabilities, and this would not have been possible without the generous support and guidance from my mentors and friends. Their encouragement helped me regain confidence and enriched my academic and personal experiences.

First and foremost, I would like to express my deepest gratitude to my supervisors, Dr. Rabah Boukherroub and Prof. Sabine Szunerits, for their patient guidance and unwavering support over the past three years. Under their mentorship, I acquired invaluable experience in experimental techniques and deepened my knowledge in chemistry and materials science. Working under their supervision has truly been a rewarding and enjoyable experience. I would also like to sincerely thank my Master's supervisors, Prof. Guodong Zhang and Prof. Longcheng Tang in China, who first introduced me to the field of scientific research. Without their early guidance and continuous support, I would not have embarked on this academic path.

My heartfelt thanks go to Dr. Min Li at Xi'an Jiaotong University for her strong support and assistance during my exchange period. Her help with experimental facilities and technical insights was essential in enabling the smooth and continuous progress of my project. I am also grateful to all my colleagues and collaborators for their support, insightful discussions, and knowledge sharing. It has been an honor to work alongside Zhaohui Zhang, Yi Zhang, Zhiran Yu, Yunchu Zeng, Yuanyuan Miao, Yisha Chen, Michele, Tomasz Swebocki, Shakila Behzadifar, Inès De Hoon, Teresa Rodrigues, Asmaa, Go Inoue, and many others. I would like to thank my dear friends Mingwei Tang, Yu Zhou, Tao An, Haihong Li, and all those who have supported and encouraged me along the way.

I am especially grateful to the China Scholarship Council (CSC) for granting me the opportunity to pursue my Ph.D. studies in France.

Last but not least, I am profoundly thankful to my family, especially my beloved parents. From childhood to this moment, their unconditional love, support, and encouragement have always been my foundation. Their integrity, diligence, resilience, patience, and humility will continue to inspire me throughout life. I would also like to thank my sister, Xiaoli Wu, who has always been a beacon in my life—guiding and supporting me whenever I felt lost or confused. Special thanks to my dear friends Hongliang Wu and Weiding Wang for their long-standing encouragement and support. I am equally thankful to all other friends who have cared for and believed in me throughout this journey.

General introduction

To address the increasing demand for high-performance, miniaturized energy storage devices in the era of flexible electronics and the Internet of Things (IoT) systems, this thesis explores the scalable fabrication and electrochemical optimization of micro-supercapacitors (MSCs) based on laser-induced graphene (LIG). Supercapacitors, known for their fast charge–discharge behavior and outstanding cycling stability, are gaining traction as complementary systems to batteries in various applications. However, challenges such as low energy density and poor material utilization efficiency persist, particularly in flexible microdevices. In response, this research integrates advanced laser processing, additive-free ink formulation, and defect-engineered nanomaterials to construct highly conductive, mechanically robust, and energy-efficient MSC platforms.

This thesis is divided into five chapters, as follows:

Chapter I provides a fundamental overview of the electrochemical energy storage mechanisms and recent progress in supercapacitor research, particularly emphasizing the roles of carbon-based and transition metal-based electrode materials. The underlying physics of electric double-layer capacitance and pseudocapacitance are discussed, alongside a review of emerging materials such as MXenes, conductive polymers, and layered double hydroxides (LDHs). Fabrication techniques including laser-induced graphene (LIG) formation, electrochemical synthesis, and printing technologies are introduced, highlighting their compatibility with flexible and integrated device manufacturing.

Chapter II details the materials, instrumentation, and characterization methods employed throughout this work. Special attention is given to the use of a CO_2 laser system for direct patterning of LIG electrodes, enabling precise interdigitated geometries without the need for masks or chemical etchants. Additionally, a commercial freeze dryer was used to process delaminated MXene into few-layer dispersions, preserving their two-dimensional morphology and surface terminations critical for electrochemical performance. Comprehensive material and device characterizations were conducted using scanning electron microscopy (SEM), transmission electron microscopy (TEM), X-ray diffraction (XRD), X-ray photoelectron spectroscopy (XPS), contact angle analysis, and electrochemical testing (cyclic voltammetry (CV), galvanostatic charge–discharge (GCD), electrochemical impedance spectroscopy (EIS)), forming the analytical foundation of the study.

Chapter III presents a scalable and programmable fabrication strategy for flexible symmetric MXene-based MSCs by combining LIG electrode patterning with mask-assisted spray deposition of additive-free MXene inks. The device structure enables enhanced wettability, interfacial adhesion, and charge transport across the LIG–MXene interface. The optimized LIG-MXene-5 device achieved an areal capacitance of 43.80 mF cm^{-2} and demonstrated stable output under various series–parallel configurations. The integration of MSC arrays with solar cells and LED indicators further validates the system's applicability in flexible, self-powered electronics. The versatility of this approach was confirmed on biodegradable paper substrates, underscoring its potential in sustainable electronics.

Chapter IV extends the performance boundaries of MSCs through defect engineering of transition metal hydroxide-based electrodes. An asymmetric micro-supercapacitor (AMSC) was constructed using hydrogen vacancy-rich CoNi-LDH as the positive electrode and FeOOH as the negative electrode. These pseudocapacitive materials were electrodeposited onto LIG substrates via a low-cost, scalable process. The resulting LIG-CoNi-$LDH_{(v)}$//LIG-FeOOH device exhibited a wide voltage window of 1.8 V, enhanced areal capacitance of 38.28 mF cm^{-2}, and remarkable cycling stability of 92% retention over 10,000 cycles. Additionally, the device demonstrated effective operation in multi-cationic neutral electrolytes, and its integration with a solar cell–LED system further confirmed its practical utility in on-chip power supplies and portable electronics.

Chapter V provides a comprehensive summary of the two projects presented in this thesis and offers forward-looking perspectives on the future development of advanced supercapacitors. These concluding insights are grounded in the broader context of flexible micro-supercapacitors (MSCs), which have emerged as vital components for powering wearable electronics, flexible devices, and integrated self-powered systems. Despite their promise, flexible MSCs still face critical challenges in simultaneously achieving high energy density, mechanical flexibility, and long-term cycling stability. This thesis addresses these issues through a systematic investigation of advanced fabrication strategies that integrate laser-induced graphene (LIG) with electrochemically active nanomaterials to optimize device performance.

The research is structured into two interrelated and progressively developed projects. The first project (Chapter III) introduces a scalable and programmable fabrication approach that combines laser patterning with mask-assisted spray coating of additive-free

MXene inks onto LIG electrodes. This strategy enables efficient electrode formation with enhanced wettability, conductivity, and surface interaction. However, due to the symmetric configuration and reliance on physically adsorbed MXene nanosheets, limitations remain in voltage window extension, energy density, and mechanical durability.

To overcome these constraints, the second project (Chapter IV) proposes a refined asymmetric MSC architecture incorporating defect-engineered nanomaterials. By employing electrochemical deposition to integrate hydrogen vacancy-rich CoNi layered double hydroxides (CoNi-LDH$_{(v)}$) onto the LIG scaffold, the design achieves a widened operational voltage window (up to 1.8 V) and significantly improved pseudocapacitive performance. Optimized deposition parameters ensure strong interfacial bonding and superior mechanical robustness, thereby enhancing device reliability under bending and long-term cycling conditions.

Together, these two projects highlight a coherent and iterative design strategy for advancing flexible energy storage systems. The work not only addresses key bottlenecks in current MSC technologies, but also lays the groundwork for scalable, durable, and high-performance solutions suitable for next-generation electronic applications.

Chapter I. Introduction

I.1. Introduction (Background)

In recent years, the explosive growth of global population, accelerating industrialization, and surging energy consumption have led to the overexploitation of fossil fuels, resulting in severe resource depletion, elevated greenhouse gas emissions, worsening air pollution, and increasingly frequent climate anomalies [1-3]. These escalating issues have prompted an urgent demand for the development of efficient, eco-friendly, and sustainable energy production and storage systems. Among various energy storage technologies, electrochemical energy storage devices—particularly batteries and supercapacitors (SCs)—have garnered significant attention, due to their complementary roles in next-generation energy infrastructure [4].

Supercapacitors, as emerging energy storage devices, bridge the gap between conventional capacitors and batteries by combining high power density with moderate energy density. Their distinctive charge storage mechanisms endow them with remarkable electrochemical performance across a wide range of applications. Unlike batteries that rely on bulk-phase redox reactions, supercapacitors store energy through physical ion adsorption (electric double-layer capacitors) or fast surface redox reactions (pseudocapacitors), thereby avoiding drastic structural changes in the electrode materials during charge/discharge cycles [5]. This feature enables supercapacitors to deliver ultra-long cycle life—often exceeding one million cycles—while minimizing safety concerns such as thermal runaway and electrolyte decomposition [6,7].

Thanks to these advantages, supercapacitors are well-suited for high-frequency charge/discharge applications, such as regenerative braking systems in electric vehicles and output smoothing in renewable energy systems. However, despite their fast response and long lifespan, limitations, such as relatively low energy density and narrow operating voltage window, still hinder their broader adoption. To overcome these bottlenecks, current research is focused on increasing the specific surface area of electrode materials, enhancing pseudocapacitive behavior, and optimizing electrode–electrolyte compatibility to expand the operational voltage range. These strategies are considered fundamental to the development of high-performance supercapacitors [8].

I.2. Development and Evolution of Supercapacitors

For modern electronic devices that require uninterrupted power throughout the day, batteries remain the primary energy source, while supercapacitors are favored for applications demanding rapid charging and discharging. Supercapacitors (SCs), also known as ultracapacitors or electrochemical capacitors, offer significantly higher capacitance than conventional capacitors by utilizing electrode materials with extremely large specific surface areas, far exceeding those achievable with traditional dielectric materials. Despite their relatively lower energy storage per unit mass or area compared to batteries, supercapacitors are distinguished by their ability to deliver much higher power density and exceptional cycling stability [9].

In conventional capacitors, two conductive electrodes are separated by a dielectric layer. Upon application of an external voltage, opposite charges accumulate on the surfaces of the electrodes, with the dielectric playing a crucial role in charge separation

and electric field formation, thereby enabling energy storage. The capacitance (C) is defined as the ratio of stored charge (Q) to applied voltage (V) [10], Eq. 1 :

$$C = Q/V \quad \text{Eq.1}$$

Furthermore, the capacitance of a parallel plate capacitor is directly proportional to the electrode surface area (A) and inversely proportional to the separation distance (D), as expressed in Eq.2 [10]:

$$C = (\epsilon_0 \epsilon_r A)/D \quad \text{Eq.2}$$

Where ϵ_r is the relative permittivity of the dielectric material, and ϵ_0 is the vacuum permittivity constant.

The energy storage capability (E) of a capacitor is related to both the capacitance and the square of the voltage, given by Eq. 3 [10]:

$$E = \frac{1}{2} CV^2 \quad \text{Eq.3}$$

Both energy density and power density are critical parameters that characterize capacitor performance, typically normalized by device volume or mass.

Unlike conventional capacitors, supercapacitors store charge through electrochemical processes occurring at or near the electrode surface. In electric double-layer capacitors (EDLCs), charge is stored by the physical adsorption of electrolyte ions on high-surface-area carbon-based electrodes. This purely non-faradaic mechanism is governed by ion

accumulation at the electrode–electrolyte interface without electron transfer, resulting in high reversibility and rapid response. Characteristic electrochemical techniques for evaluating EDLC behavior include cyclic voltammetry (CV), which often yields near-rectangular curves, and galvanostatic charge–discharge profiles with linear voltage-time behavior. In contrast, pseudocapacitors utilize fast and reversible redox reactions at the electrode surface or near-surface region to store charge, leading to faradaic contributions that enhance both specific capacitance and energy density. This pseudocapacitive behavior bridges the gap between EDLCs and batteries, offering higher power and energy densities, as well as prolonged cycle life. Representative pseudocapacitive materials include transition metal oxides such as Co_3O_4 and RuO_2, as well as certain nitrides and carbides, which exhibit superior charge storage characteristics due to their redox-active nature [10].

Overall, the evolution from conventional capacitors to supercapacitors has been driven by the need for energy storage technologies that offer both high power output and enhanced energy capacity. The synergy between EDLC and pseudocapacitive mechanisms provides a versatile platform for the development of next-generation energy storage devices.

I.2.1. Types of Supercapacitors

Supercapacitors are generally classified into three main categories: electric double-layer capacitors (EDLCs) [11], pseudocapacitors [12], and hybrid capacitors [13]. These types reflect the dominant charge storage mechanisms involved. Charge transfer at the interface between electrode and electrolyte plays a crucial role, particularly in faradaic processes such as redox reactions. Interestingly, non-faradaic mechanisms do not involve

electron transfer; instead, surface charge is stored through physical adsorption, with no chemical reactions taking place [14].

I.2.1.1. Electric Double-Layer Capacitors (EDLCs)

In EDLCs, charge is stored via the electrostatic separation of ions at the Helmholtz double layer formed at the interface between a conductive electrode and an electrolyte [15]. The capacitance in these devices originates from the physical adsorption of ions onto the surface of electrode materials (**Figure I.1a**). To achieve high capacitance, electrode materials must exhibit not only excellent electrical conductivity but also large accessible surface area. Thus, material selection is critical to EDLC performance.

The effective charge separation distance in the double layer is typically on the nanometer scale. Nanostructured carbon-based materials with high specific surface areas (SSA) are ideal for this purpose. These include graphene and its derivatives, activated carbon (AC), carbon nanotubes (CNTs), carbon nanohorns, carbon fibers, carbon cloth, and porous carbon [16]. EDLCs typically display a linear voltage-time profile during discharge, and the stored energy is proportional to the square of the voltage. The capacitance of EDLCs is analogous to that of classical capacitors and can be described by Eq.4 [10]:

$$C = (\epsilon_0 \epsilon_r A)/d \qquad \text{Eq.4}$$

where ϵ_r is the relative permittivity of the double layer, ϵ_0 is the vacuum permittivity, A is the electrode surface area, and d is the effective thickness of the double layer.

Since EDLCs rely on electrostatic charge storage without faradaic reactions, they offer rapid charge/discharge capabilities and outstanding cycle life—often far exceeding that of batteries. Additionally, since the electrolyte solvent does not participate in the storage mechanism, EDLCs avoid many of the degradation mechanisms associated with battery electrolytes [17].

I.2.1.2. Pseudocapacitors

In pseudocapacitors, charge storage occurs *via* fast and reversible surface redox reactions. These processes involve ion adsorption, intercalation, or diffusion into the electrode structure, often accompanied by changes in oxidation states of the electrode material. This faradaic charge transfer can reach up to 2.7 electrons per atom at the surface, significantly higher than in EDLCs (**Figure I.1b**).

Pseudocapacitive materials include conducting polymers and transition metal compounds such as oxides, nitrides, sulfides, and hydroxides. These materials contribute additional capacitance through redox activity, often resulting in energy densities 10–100 times greater than those of EDLCs. However, the slower faradaic processes in pseudocapacitors generally lead to lower power densities. Additionally, volume changes during cycling can compromise mechanical stability and reduce lifetime [18].

I.2.1.3. Hybrid Supercapacitors

Hybrid supercapacitors combine EDLC and pseudocapacitive (or even battery-type) mechanisms, typically using asymmetric electrode configurations (**Figure I.1c**). Rather than simple physical mixing, successful hybrids require the careful design of nanoscale or microscale architectures that allow efficient chemical exchange between components [19].

Hybrid systems may pair an EDLC electrode with a pseudocapacitive or battery-type electrode, creating devices that benefit from both high energy density and enhanced power performance. This synergistic integration enables higher electrochemical performance by combining fast kinetics from EDLCs with high-capacity storage from faradaic materials [20,21].

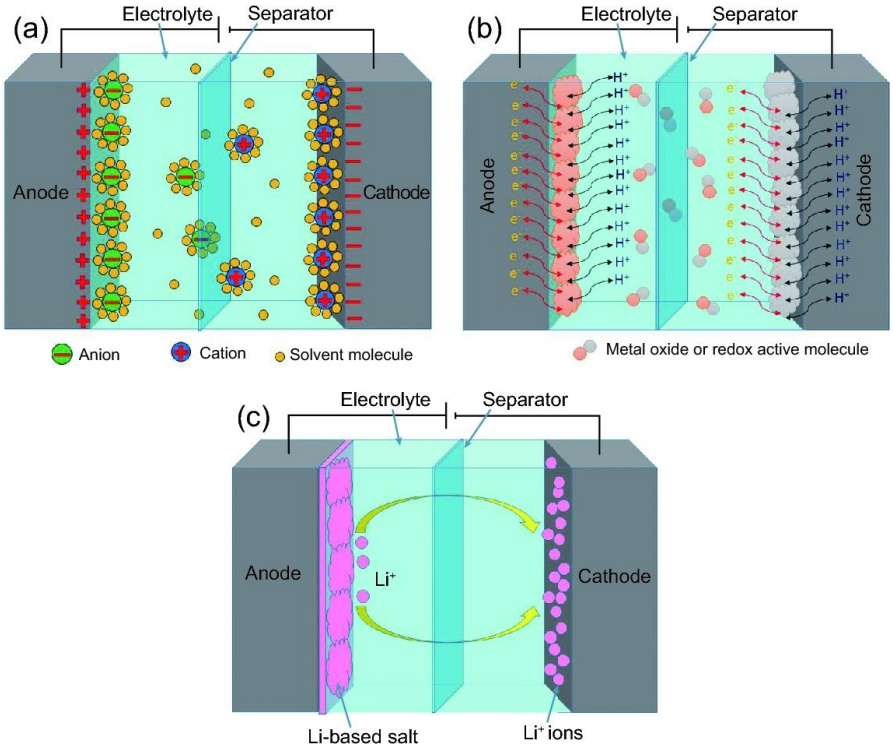

Figure I.1. Schematic representation of (**a**) electrical double-layer capacitor (EDLC), (**b**) pseudocapacitor (PC) and (**c**) hybrid supercapacitor (HSC) [8].

I.2.2. Charge Storage Mechanisms

The operation of supercapacitors is governed by three primary charge storage mechanisms (**Figure I.2**): (1) Double-Layer Formation: In EDLCs, an electric double layer forms at the electrolyte/electrode interface, often referred to as the Helmholtz layer [22]. Models such as the Gouy–Chapman–Stern theory describe this structure. Activated

carbon is commonly used due to its high surface area, enabling capacitive storage in the Farad range, far beyond the microfarad or picofarad levels of traditional capacitors. (2) Pseudocapacitive Redox Reactions: As proposed by Trasatti, pseudocapacitors store charge through reversible surface redox reactions involving transition metal oxides. These reactions promote partial charge transfer between the electrode and electrolyte [23]. Even when fully charged, such electrodes remain active in both oxidation and reduction states. Cation adsorption and reduction lower the oxidation state of the active material, and the reverse occurs during discharge. (3) Ion Intercalation and Diffusion [24]: In this mechanism, typical of pseudocapacitive materials, electrolyte ions rapidly intercalate into the electrode structure. The process is diffusion-controlled and characterized by two features: high reversibility during charge/discharge and voltage-dependent charge storage. Together, these mechanisms enable the design of supercapacitors with tailored performance for specific applications, balancing energy density, power output, and cycling stability.

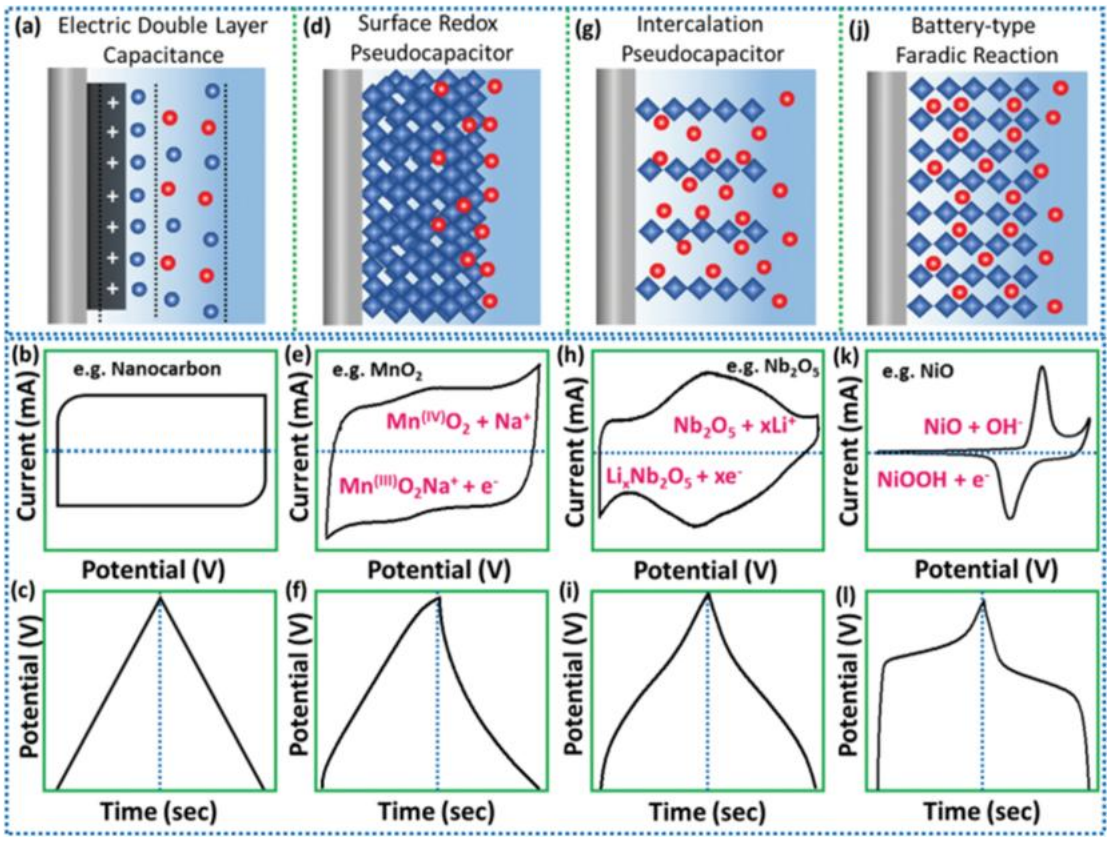

Figure I.2. Schematic illustration of electrochemical characteristics for different energy storage mechanisms, along with their representative cyclic voltammetry (CV) and galvanostatic charge–discharge (GCD) curves: (**a–c**) electric double-layer capacitance (EDLC); (**d–f**) surface redox capacitance; (g–i) capacitive intercalation; and (**j–l**) faradaic battery-type behavior [25].

I.3. Typical Fabrication Techniques for Supercapacitors

To meet the diverse requirements of high-performance supercapacitors in terms of energy density, power output, and device integration, a wide array of fabrication strategies has been developed for constructing nano-/microstructured electrode materials. These methods can be broadly categorized into six types, encompassing both top-down patterning and bottom-up chemical synthesis approaches. Each method offers distinct advantages and is well-suited for different application scenarios [26].

I.3.1. Laser-Induced Graphene (LIG) Technique

Since its introduction in 2014, laser-induced graphene (LIG) has attracted significant attention due to its high efficiency, low cost, and facile processing [27,28]. In this technique, a laser beam locally irradiates solid precursors, inducing rapid thermal transformation and directly generating 3D porous graphene-like carbon structures [29-31]. This one-step approach enables both patterning and material conversion without the need for cleanroom facilities. More importantly, the morphology, conductivity, and surface area of the resulting LIG can be precisely tuned by adjusting laser parameters (e.g., wavelength, scan speed), precursor composition, and ambient atmosphere [32-35]. LIG has been widely applied in flexible electronics, including wearable sensors and heaters, with electrode materials for supercapacitors emerging as a key area of focus [36,37].

I.3.2. Printing Technologies

Printing technologies have recently emerged as scalable and solution-processable approaches for flexible electronics and energy storage devices. Representative techniques include screen printing, inkjet printing, and extrusion printing [38-40]. By formulating functional inks and combining them with tailored structural designs, patterned electrodes can be deposited on diverse substrates such as paper, textiles, and polymer films. Printing offers high precision, adaptability, and suitability for mass production [41]. Optimizing ink rheology, surface wettability, and deposition behavior is essential for achieving high-resolution, conductive patterns—making this method especially attractive for fabricating flexible, high-energy-density supercapacitors [42-45].

I.3.3. Electrochemical Synthesis

Electrochemical methods are widely employed due to their simplicity, eco-friendliness, and high tunability [46]. These methods rely on redox reactions, electrolysis, ion intercalation, or deposition processes under electric fields to grow or modify active materials on electrode surfaces. Parameters such as potential, current density, electrolyte type and concentration, reaction time, and temperature can be tailored to control composition, crystallinity, morphology, and electrochemical performance [47]. Compared to high-temperature or chemical reduction methods, electrochemical synthesis often occurs at room temperature under mild conditions, making it cost-effective for large-scale production. It is particularly effective for synthesizing graphene sheets, metal oxides, conductive polymers, and their composites—key components in supercapacitor research.

I.3.4. Solution-Based and Sol–Gel Methods

Traditional wet chemical approaches such as co-precipitation and sol–gel techniques are extensively used to synthesize uniform metal oxides and their composites [48]. The hydrolysis and condensation steps in the sol–gel process enable precise control over stoichiometry, crystal structure, and pore architecture, making it an efficient route for constructing 3D porous scaffolds in electrode materials [49-51].

I.3.5. Hydrothermal/Solvothermal Synthesis

These methods utilize sealed, high-temperature, high-pressure conditions to induce crystal growth and structural ordering. They are ideal for synthesizing nanostructures such as nanorods, nanosheets, and hollow spheres from metal oxides and sulfides.

Reaction temperature, time, and precursor ratios can be finely adjusted to control morphology. This approach is particularly effective for producing high-surface-area materials like Co_3O_4, MnO_2, and $Ni(OH)_2$, which are widely used as pseudocapacitive materials [52-54].

I.3.6. Vapor-Phase Deposition (CVD, ALD)

Chemical vapor deposition (CVD) and atomic layer deposition (ALD) are vital techniques for fabricating high-quality thin films. CVD enables the growth of highly crystalline materials such as graphene and carbon nanotubes, offering excellent electrical conductivity. ALD, on the other hand, allows atomic-level deposition of ultrathin films on complex substrates, commonly used for interface engineering and protective coatings. Despite requiring sophisticated equipment, these methods are essential for device miniaturization and performance optimization [55,56].

Currently, the synthesis of supercapacitor materials is evolving toward multi-modal strategies, such as combining LIG with printing or electrochemical synthesis with hydrothermal processing [57]. Emerging trends include *in situ* device integration (e.g., monolithic LIG electrodes) [58,59], environmentally benign and energy-efficient fabrication [60], and transfer-printable processes tailored for flexible/wearable applications [61]. The ultimate goal is to simultaneously enhance energy density, power capability, and cycling stability while maintaining cost-effectiveness and manufacturing simplicity, paving the way for the industrial and consumer deployment of supercapacitors [62].

I.4. Electrode Materials

Supercapacitors primarily consist of electrodes and electrolytes, with the properties and nanostructural design of the electrode materials directly influencing the performance of devices across various applications. To achieve high-performance supercapacitors, it is essential to disperse materials at the nanoscale. In recent years, various nanomaterials with excellent dispersibility and electrochemical activity have been widely employed in the development of flexible and micro-supercapacitors. The following section systematically introduces representative nanomaterial systems suitable for supercapacitor fabrication.

I.4.1. Carbon-Based Materials

Carbon-based materials have demonstrated extensive adaptability in energy storage devices, due to their structural diversity and excellent chemical compatibility. They can form stable covalent bonds with various elements or other carbon allotropes, endowing them with high strength, density, and superior chemical stability [63-65]. In recent years, the controllable construction of carbon materials has provided a foundation for device design across a range of applications, particularly in energy and environmental sectors. Among them, graphene and carbon nanotubes (CNTs) play pivotal roles in tackling global climate issues and reducing greenhouse gas emissions. Developing green and efficient energy storage technologies using such materials is a key path toward achieving sustainable energy systems [66-68].

I.4.1.1. Carbon Nanotubes (CNTs)

Carbon nanotubes (CNTs) consist of rolled-up single or multiple layers of graphene into hollow one-dimensional tubular structures, where carbon atoms are arranged in a hexagonal lattice. The diameter of single-walled CNTs can be as small as 0.7 nm, whereas multi-walled CNTs can reach up to 100 nm in diameter, with lengths ranging from micrometers to millimeters. The ends of CNTs are typically capped with hemispherical fullerene-like structures [69].

CNTs exhibit outstanding thermal conductivity, electrical conductivity, mechanical strength, and chemical stability, along with high specific surface area and excellent energy storage capacity. These attributes make CNTs highly promising electrode materials for supercapacitors. Moreover, their radial dimensions lie in the nanoscale, and axial lengths extend to the microscale, making them quintessential one-dimensional quantum materials. In multi-walled CNTs, the interlayer spacing between concentric graphene tubes is approximately 0.34 nm, with typical overall diameters ranging from 2–20 nm [70].

Thanks to their superior electrochemical performance, CNTs have garnered significant attention in flexible energy storage applications. For instance, Kim et al. developed high-performance planar stacked micro-supercapacitor arrays with excellent flexibility and water resistance by printing CNT-based inks, which are suitable for wearable electronics (**Figure I.3**) [71].

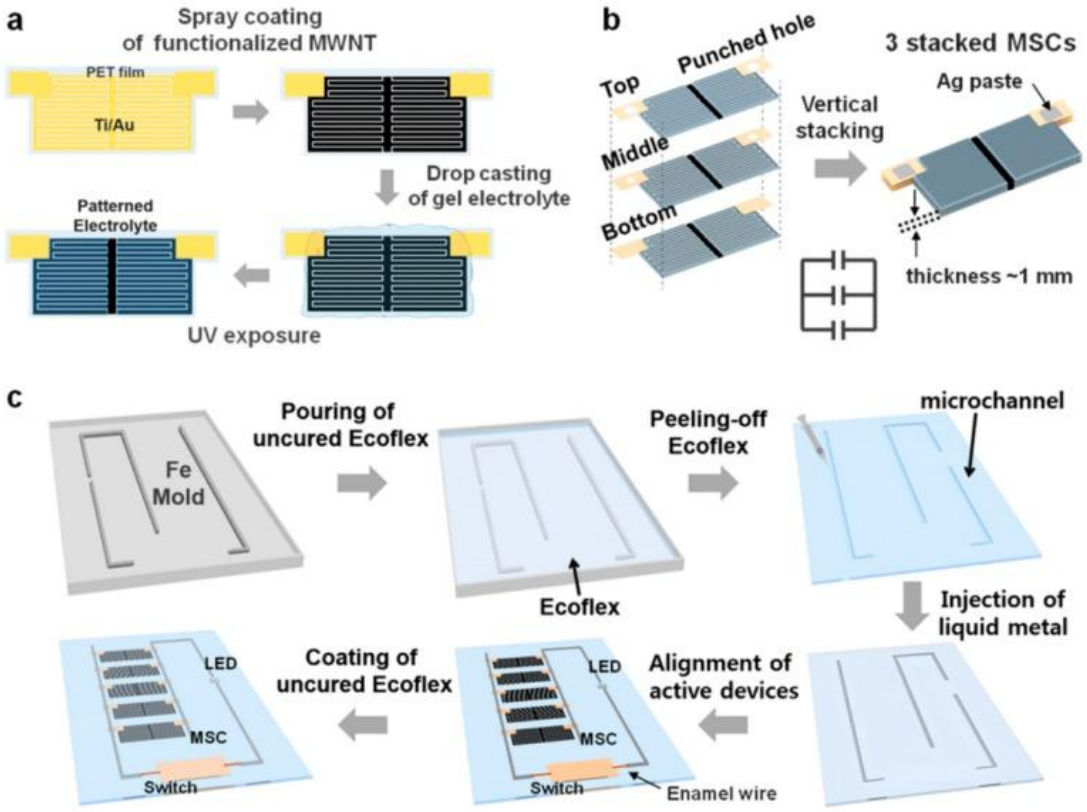

Figure I.3. Schematic illustration of spray printing CNT-based ink for the fabrication of micro-supercapacitors. (**a**) A single MSC device directly spray-printed onto the substrate; (**b**) A stacked configuration of three spray-printed MSCs; (**c**) An array of MSCs spray-printed on the substrate [71].

I.4.1.2. Graphene

Graphene is an allotrope of carbon composed of sp^2-hybridized carbon atoms arranged in a two-dimensional honeycomb lattice, forming a quasi-2D material with a single-atom-layer thickness. Owing to its exceptional conductivity, mechanical strength, and thermal stability, graphene is considered a revolutionary material across diverse fields such as energy storage, micro/nanofabrication, materials science, biomedicine, and flexible electronics [72].

In electrochemical energy storage, graphene offers a high theoretical specific surface area (up to 2630 $m^2\ g^{-1}$), excellent electrical conductivity, and abundant charge storage sites, making it a prominent candidate for supercapacitor electrodes. Literature reports indicate an intrinsic capacitance of ~21 mF cm^{-2} for monolayer graphene, with a theoretical EDLC capacitance up to 550 F g^{-1} if the surface area is fully utilized [73].

Due to its flexible, thin-layered structure, graphene is well-suited for wearable and portable storage devices. For example, Abdelkader et al. screen-printed graphene oxide (GO) inks onto textile substrates and reduced them *in situ* via electrochemical methods to fabricate flexible solid-state supercapacitor electrodes (**Figure I.4**). Strong interfacial adhesion between GO inks and textiles ensured excellent mechanical stability under repeated bending and cycling, with robust electrochemical performance even after 10,000 charge-discharge cycles [74].

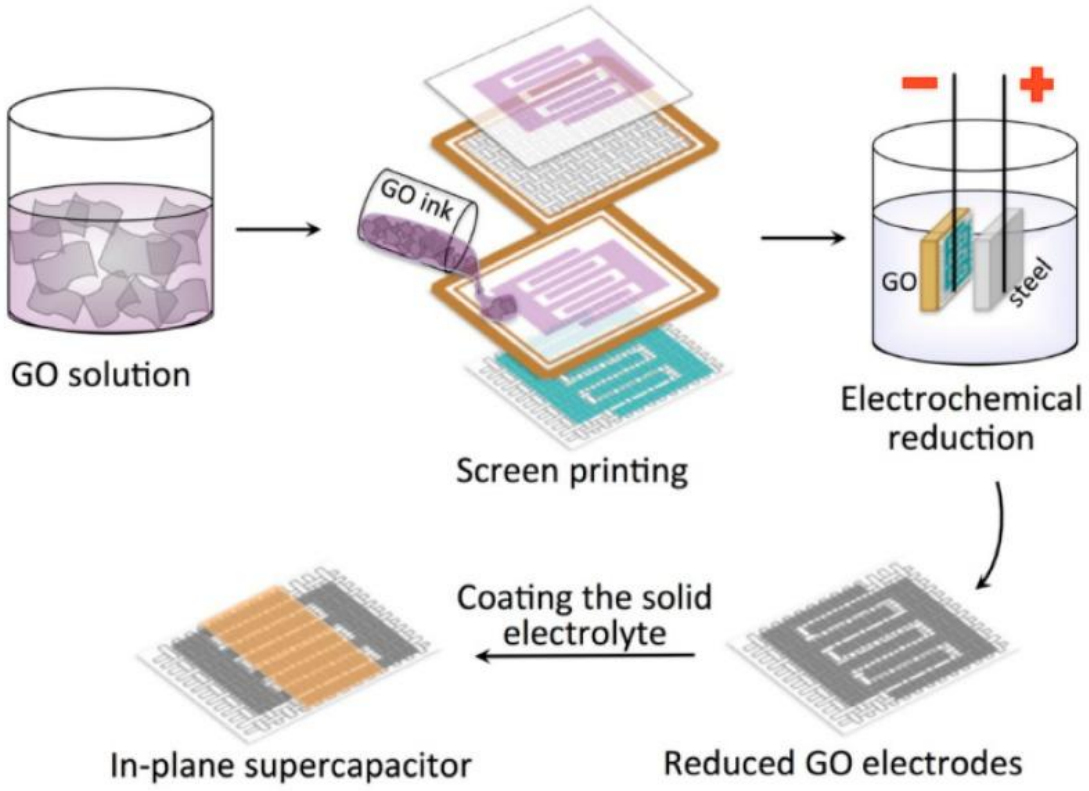

Figure I.4. Fabrication of planar supercapacitors via screen printing of graphene oxide (GO) ink on fabric substrates, followed by electrochemical reduction to form reduced graphene oxide (rGO) electrodes [74].

However, strong van der Waals forces between graphene nanosheets often lead to agglomeration and restacking, hindering the full utilization of their surface area and resulting in actual capacitance values far below theoretical limits. To overcome this limitation, researchers have extensively explored composite strategies by integrating graphene with conductive polymers or metal oxides to enhance conductivity and improve overall storage performance. For example, Liu et al. employed extrusion printing to fabricate GO/polyaniline (PANI) composite ink-based micro-supercapacitors, extending the voltage window from 0.8 to 1.2 V and significantly enhancing energy density (from 3.36 to 4.83 mWh cm^{-3}) and power density (from 9.82 to 25.3 W cm^{-3}) [75]. Additionally, graphene inks have been used for direct printing of 3D structures. Li et al. applied such inks in 3D extrusion printing of flexible micro-supercapacitors, achieving excellent specific capacitance, cycling stability, mechanical flexibility, and integration compatibility with microelectronic systems (**Figure I.5**) [76].

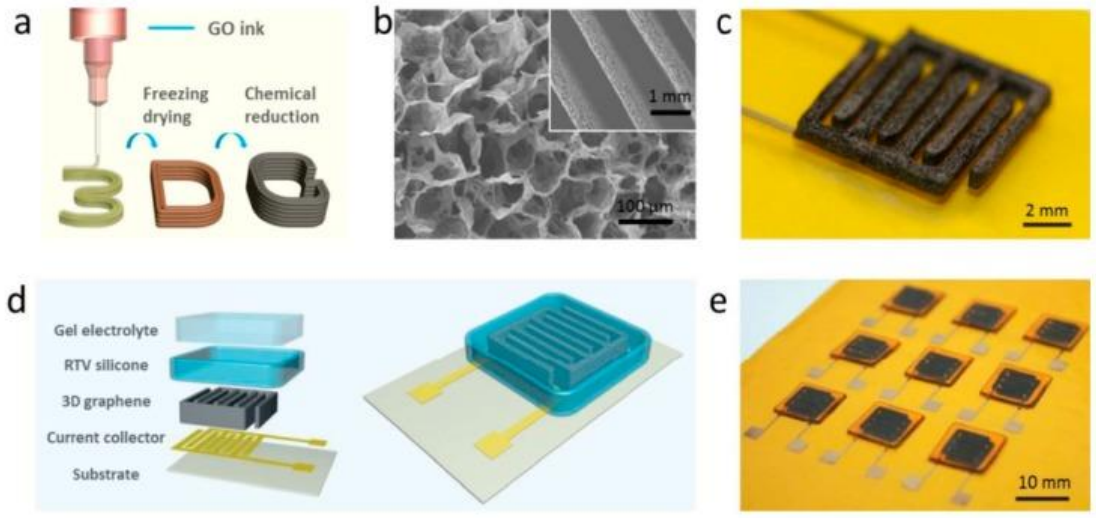

Figure I.5. Schematic illustration of the fabrication process for 3D-printed micro-supercapacitors: (**a**) 3D printing of graphene oxide (GO) ink; (**b**) SEM image of the printed graphene electrode; (**c**) Interdigitated 3D electrode structure; (**d**) Assembly of a 3D micro-supercapacitor; (**e**) Array of the printed 3D micro-supercapacitor devices [76].

I.4.1.3. Carbon Nanofibers (CNFs)

Carbon nanofibers (CNFs), similar to CNTs, are composed of graphene layers. However, CNFs typically exhibit tapered or cup-stacked curled structures instead of hollow cylindrical forms. This unique morphology imparts high mechanical strength, thermal and electrical conductivity, and electromagnetic shielding properties. CNFs are graphite microcrystalline materials with fibrous structures and high carbon content (>90%), characterized by graphitic carbon layers aligned along the fiber axis. This ordered arrangement endows them with high tensile strength, modulus, low density, and favorable conductive/thermal properties [77].

In energy storage, the 3D porous architecture of CNFs facilitates electrolyte penetration and ion transport, especially through open mesopores and micropores, enhancing ion adsorption and desorption. Their excellent thermal resistance, low thermal expansion coefficient, and outstanding chemical stability enable structural integrity under high temperatures or corrosive conditions. For example, Noh et al. fabricated high-performance supercapacitors by compositing CNFs with MnO_2, achieving an areal capacitance of 4.86 mF cm^{-2} and an expanded working voltage window up to 2.0 V, while maintaining high mechanical strength (**Figure I.6**) [78].

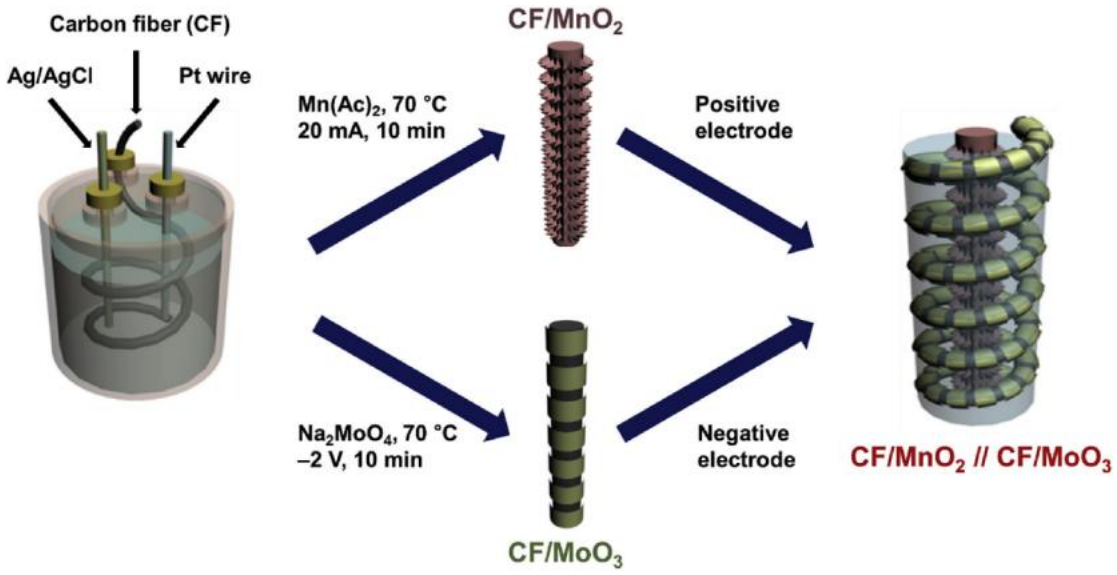

Figure I.6. Schematic illustration of the assembled all-solid-state fiber-shaped asymmetric supercapacitor (ASC), comprising CF/MnO_2 as the positive electrode and CF/MoO_3 as the negative electrode [78].

Nonetheless, CNFs generally possess dense structures, limited porosity, and low specific surface areas (<10 $m^2\ g^{-1}$), which constrain their electrochemical performance as electrode materials. Therefore, surface activation, chemical oxidation, and physical etching are commonly employed to enhance their surface area and interfacial charge storage capabilities, thereby improving energy storage performance [78].

I.4.2. MXenes

MXenes represent a class of two-dimensional materials composed of transition metal carbides, nitrides, or carbonitrides, typically expressed by the general formula $M_{n+1}X_nT_x$ (n = 1–3), where M denotes an early transition metal (e.g., Ti, V, Nb, Mo), X refers to carbon and/or nitrogen, and T_x represents surface terminal groups (such as —O, —OH, or —F). These materials are generally synthesized by selective chemical etching of the A-layer from their corresponding MAX phase precursors ($M_{n+1}AX_n$, where A is a group

IIIA or IVA element), as illustrated in **Figure I.7**. In 2011, Gogotsi's group pioneered the preparation of MXenes by etching Ti_3AlC_2 with hydrofluoric acid, yielding $Ti_3C_2T_x$—one of the earliest reported MXenes [79]. Since then, the MXene family has expanded rapidly, with variants, such as Ti_2C, Nb_2C and Ti_3CN, being developed through modified etching methods (e.g., NH_4HF_2) and novel transition metal combinations [80-82]. Structurally, MXenes can be categorized into solid-solution types (random M-layer distribution) and ordered configurations (e.g., alternating or double-layered metal arrangements), with the latter predicted to be energetically more favorable in certain compositions [83].

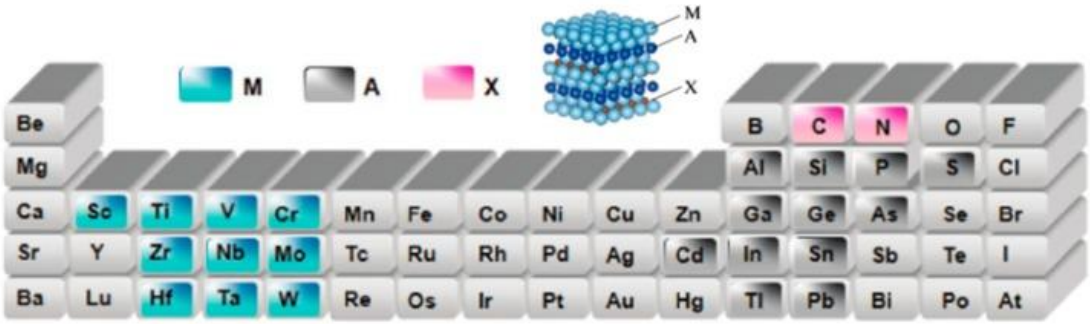

Figure I.7. Periodic table highlighting possible constituent elements for the MAX phases. Reproduced from [79].

In energy storage applications, MXenes have demonstrated outstanding charge storage capabilities, due to their intrinsic layered architecture and high surface hydrophilicity [84]. Their ultrathin 2D morphology provides a large specific surface area and metallic conductivity, facilitating rapid ion diffusion and electron transport. Furthermore, their surface terminations promote efficient intercalation/deintercalation of cations (e.g., Li^+, Na^+, Mg^{2+}), thereby contributing to notable pseudocapacitive behavior [85,86]. For instance, a Ti_2CT_x//activated carbon asymmetric supercapacitor exhibited an extended working voltage window of 1.0–3.5 V in 1 M $LiPF_6$ organic electrolyte, delivering an

energy density of 30 Wh kg^{-1} with robust rate capability and excellent cycling performance at 10C [87].

Flexible MXene films are typically fabricated via vacuum filtration or layer-by-layer assembly of colloidal dispersions (**Figure I.8a, b**). Additive-free, binderless, and freestanding $Ti_3C_2T_x$ films obtained by filtering aqueous dispersions have demonstrated high electrical conductivity, hydrophilicity, and volumetric capacitance up to 340 F cm^{-3}, with a specific surface area of ~98 m^2 g^{-1}—comparable to high-grade carbon materials [88,89]. Moreover, by etching Ti_3AlC_2 with a LiF-HCl mixture, followed by hydration and swelling, researchers have produced flexible $Ti_3C_2T_x$ films with thicknesses around 10 μm (**Figure I.8c**). The assembled symmetric devices, operated in H_2SO_4 electrolyte, achieved impressive volumetric and gravimetric capacitances of 900 F cm^{-3} and 245 F g^{-1}, respectively, and retained nearly 100% capacitance after 10,000 cycles [90].

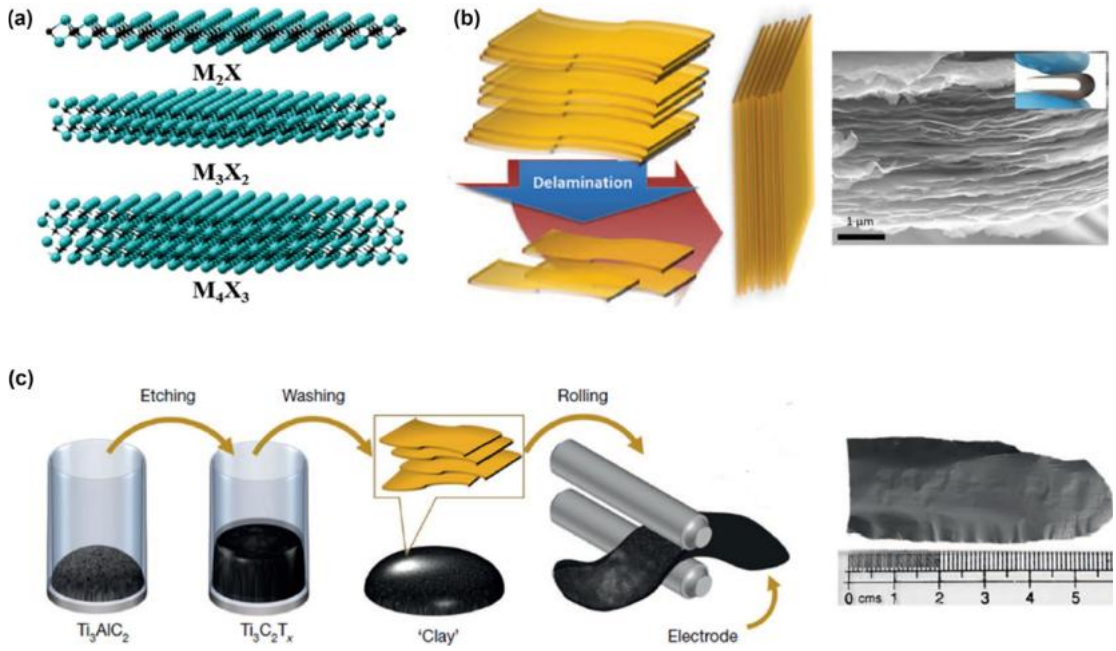

Figure I.8. (**a**) Schematic representations of MXene structures with different stoichiometries: M_2X, M_3X_2, and M_4X_3 [88]. (**b**) Illustration of the fabrication process for

a free-standing Ti_3C_2 electrode via delamination and vacuum-assisted filtration, along with photographs of the resulting electrode [89]. (**c**) Schematic synthesis route of $Ti_3C_2T_x$ clay derived from $Ti_3AlC_2T_x$, which can be processed into a flexible, free-standing film by mechanical rolling [90].

Despite their excellent electrochemical performance, MXene-based electrodes often suffer from restacking of nanosheets, which restricts ion accessibility and limits the full utilization of available active sites. To mitigate these limitations, various strategies have been proposed, including constructing three-dimensional porous frameworks, introducing interlayer spacers, forming composites with conductive additives, and tuning surface terminal groups [91]. Additionally, increasing efforts have been directed toward the development of stretchable and bendable MXene-based energy storage devices, utilizing scalable techniques, such as printing, lamination and spray-coating, to enable their integration into next-generation wearable electronics [92,93].

I.4.3. Conductive Polymers

Conductive polymers, a class of organic macromolecules with conjugated structures, have garnered extensive attention in recent years as promising electrode materials for supercapacitors, due to their excellent electrical conductivity, electrochemical activity, and favorable processability. Since the groundbreaking discovery in 1977 that doping could significantly enhance the electrical conductivity of polyacetylene [94]—challenging the long-standing perception of organic polymers as insulators—research into representative conductive polymers such as polypyrrole (PPy), polyaniline (PANI), and polythiophene (PTi) has rapidly expanded [95,96]. The energy storage mechanism of conductive polymers is primarily based on fast and reversible doping/de-doping

processes, characteristic of pseudocapacitive behavior. Their amorphous molecular networks contain numerous voids that can accommodate relatively large electrolyte ions and enable bulk charge storage, thus substantially increasing their specific capacitance. Compared to traditional carbon-based materials, conductive polymers typically exhibit higher theoretical capacitance values [97]. Furthermore, in contrast to metal oxides, they demonstrate faster electrochemical response, superior mechanical flexibility, and are particularly suited for the development of wearable and miniaturized energy storage devices [98].

In addition to their electrochemical advantages, conductive polymers possess excellent mechanical flexibility, reversible redox behavior, and favorable optoelectronic properties. Their compatibility with solution-based processes also makes them ideal for low-cost fabrication techniques such as printing, inkjet deposition, and template-assisted assembly [99-102]. With advances in nanofabrication, increasing research efforts have focused on engineering nanostructured conductive polymers to enhance charge transport kinetics and cycling stability [103-105]. For example, Chi et al. utilized inkjet printing to deposit a graphene hydrogel (GH) composite electrode containing PANI nanostructures onto pre-treated graphene paper (GP), as illustrated in **Figure I.9**. The π-π stacking interactions between the GH framework and nanostructured PANI facilitated intimate interfacial contact, significantly improving the electrode's conductivity, specific capacitance, and cycling durability [106]. The resulting flexible paper-based supercapacitor exhibited an impressive energy density of 24.02 Wh kg^{-1} at a power density of 400.33 W kg^{-1}, demonstrating outstanding overall electrochemical performance.

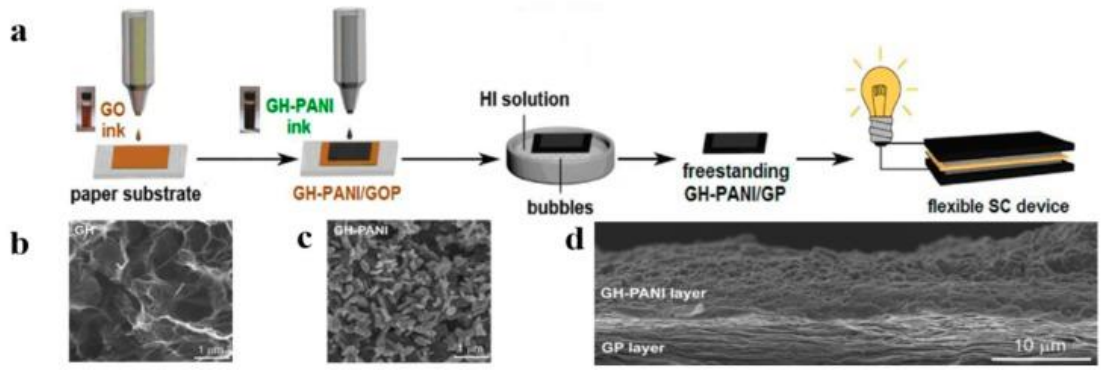

Figure I.9. (**a**) Schematic illustration of the fully printed fabrication process for a paper-based supercapacitor; (**b**) Graphene hydrogel (GH) exhibiting a porous 3D network; (**c**) Coral-like nanostructured polyaniline (PANI) grown on the GH framework; (**d**) Layered assembly of graphene paper and nanocomposite electrodes [106].

In summary, conductive polymers have emerged as highly promising candidates for flexible and micro-scale supercapacitors, owing to their tunable molecular structures, high electrochemical activity, and mechanical adaptability. Rational design of their nanostructures and composite configurations is expected to further improve their cycle life and energy density, paving the way for their integration into next-generation wearable electronics and portable energy storage systems.

I.4.4. Transition Metal Oxides and Hydroxides

Transition metal oxides and hydroxides have attracted significant research interest as pseudocapacitive electrode materials for supercapacitors, owing to their unique charge storage mechanisms, high theoretical capacitance, and excellent electrochemical stability [107]. In contrast to conventional carbon-based materials, these compounds not only store charge via electric double-layer formation, but also participate in rapid and reversible Faradaic redox reactions with electrolyte ions, thereby substantially enhancing energy density [108]. Compared with conductive polymers, metal oxides and hydroxides

generally exhibit longer cycling lifespans and superior thermal stability. Typical examples include RuO_2, MnO_2, NiO, and Fe_3O_4 among oxides, and layered double hydroxides (LDHs) as representative hydroxides.

I.4.4.1. Ruthenium Dioxide (RuO_2)

RuO_2 is one of the earliest metal oxides employed in supercapacitors and is characterized by its high conductivity, excellent electrochemical reversibility, and wide voltage window (up to 1.2 V). It demonstrates a high specific capacitance, outstanding energy density, and stable cycling performance [109]. RuO_2 maintains electrochemical stability in gel electrolytes such as PVA/H_2SO_4 and undergoes highly reversible redox transitions between three oxidation states within a 1.2 V window. For instance, Cho et al. fabricated a RuO_2/graphene/PEDOT:PSS hybrid electrode via screen printing. The resulting 5 μm thick electrode exhibited a conductivity of 1570 S cm^{-1} and a specific capacitance of 820 F g^{-1}, retaining 81.5% of its capacitance after 1000 cycles (**Figure I.10**) [110]. However, the commercialization of RuO_2 is hindered by its high cost, limited availability, and unresolved environmental concerns.

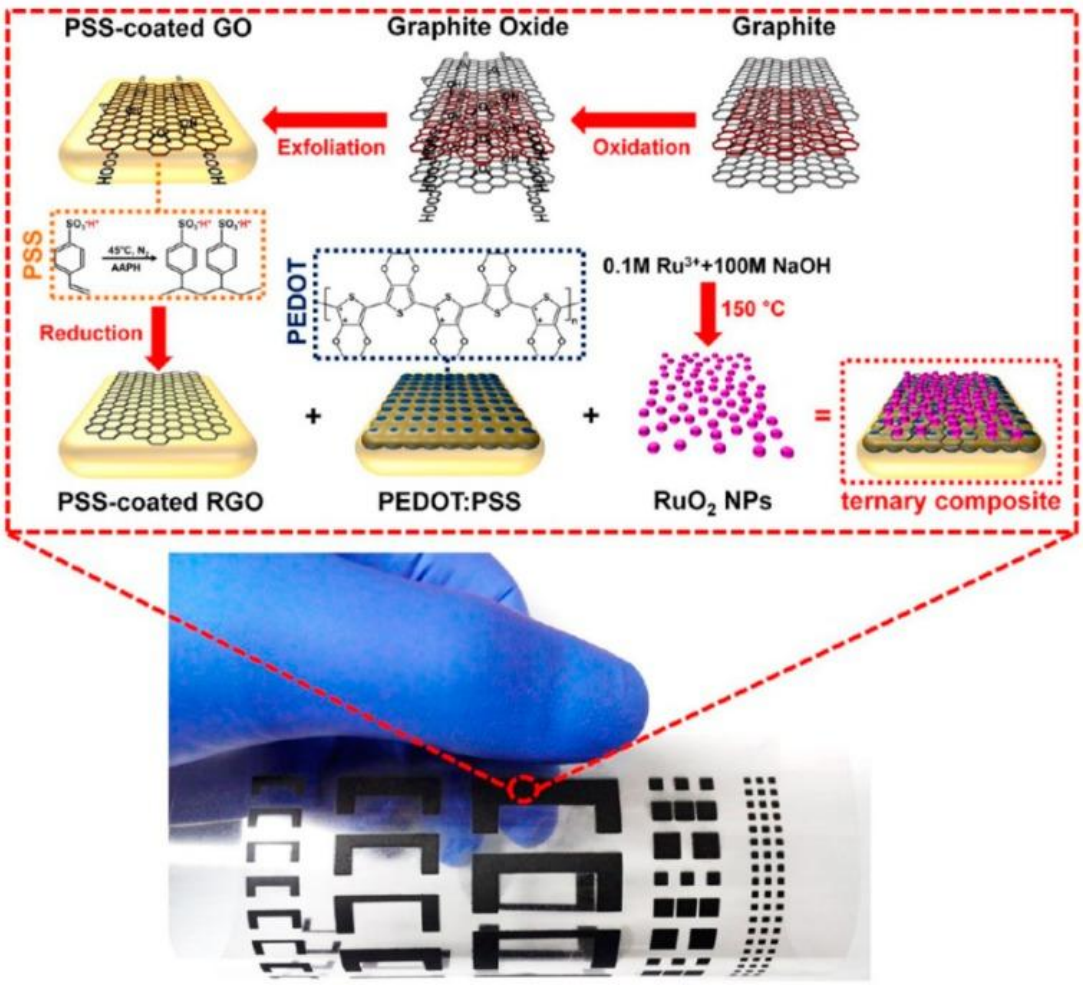

Figure I.10. Illustration of the complete screen-printing process for fabricating RuO_2 composite electrodes, along with an image of the resulting printed supercapacitor electrode [110].

I.4.4.2. Manganese Dioxide (MnO_2)

MnO_2 has emerged as a promising alternative due to its abundance, low cost, environmental benignity, and theoretical capacitance as high as 1370 F g^{-1} [111]. Despite its favorable redox activity, the poor intrinsic conductivity of MnO_2 (~10^{-5}–10^{-6} S/m) limits its rate capability [112]. Strategies such as hybridizing with conductive carbon materials (e.g., graphene, CNTs) or other oxides are widely adopted to enhance its

electrical conductivity and structural stability. For instance, Lu et al. fabricated MnO_2/FeOOH composite electrodes using screen-printing technology. The resulting solid-state supercapacitor delivered a specific capacitance of 350.2 F g^{-1} at 0.5 A g^{-1} and maintained 159.5 F g^{-1} even at 20 A g^{-1}, along with 95.6% capacitance retention after 10,000 cycles (**Figure I.11**) [113].

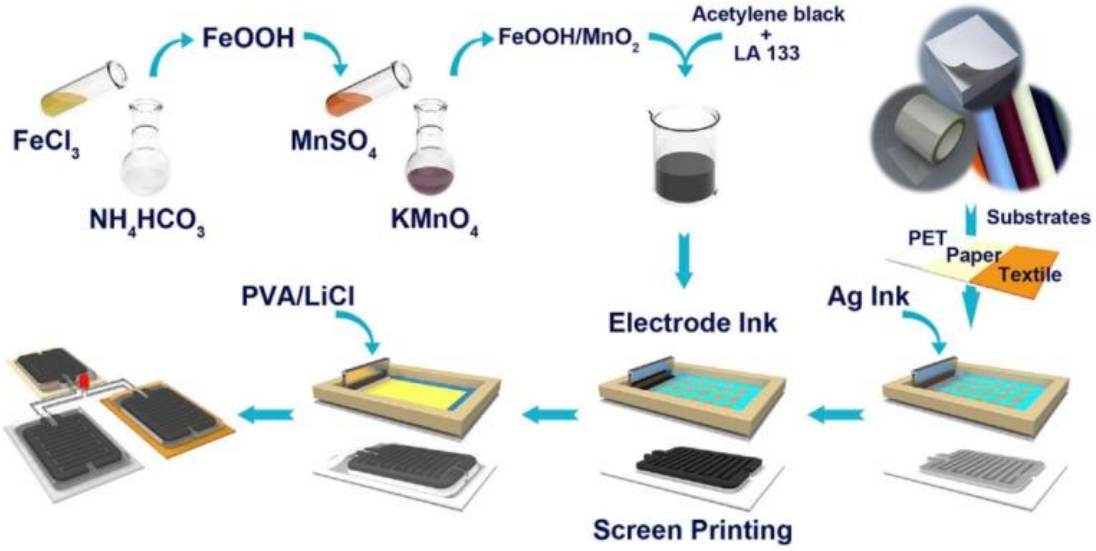

Figure I.11. Schematic illustration of the preparation of MnO_2 composite ink and the screen-printing process used to fabricate MnO_2-based supercapacitor electrodes [113].

I.4.4.3. Layered Double Hydroxides (LDHs)

Layered double hydroxides (LDHs), also referred to as anionic clays, are a class of two-dimensional materials consisting of positively charged metal hydroxide layers and interlayer charge-compensating anions [114]. Their general formula is $[M1-xa+Mx'b+(OH)_2]y+[Ay/cc-]y+\cdot zH_2O$ (where $y=a(1-x)+bx-2$, M^{2+} and M^{3+} are divalent and trivalent metal cations such as Ni^{2+}, Co^{2+}, and Al^{3+}, and A is an interlayer anion) (**Figure I.12**) [115-118].

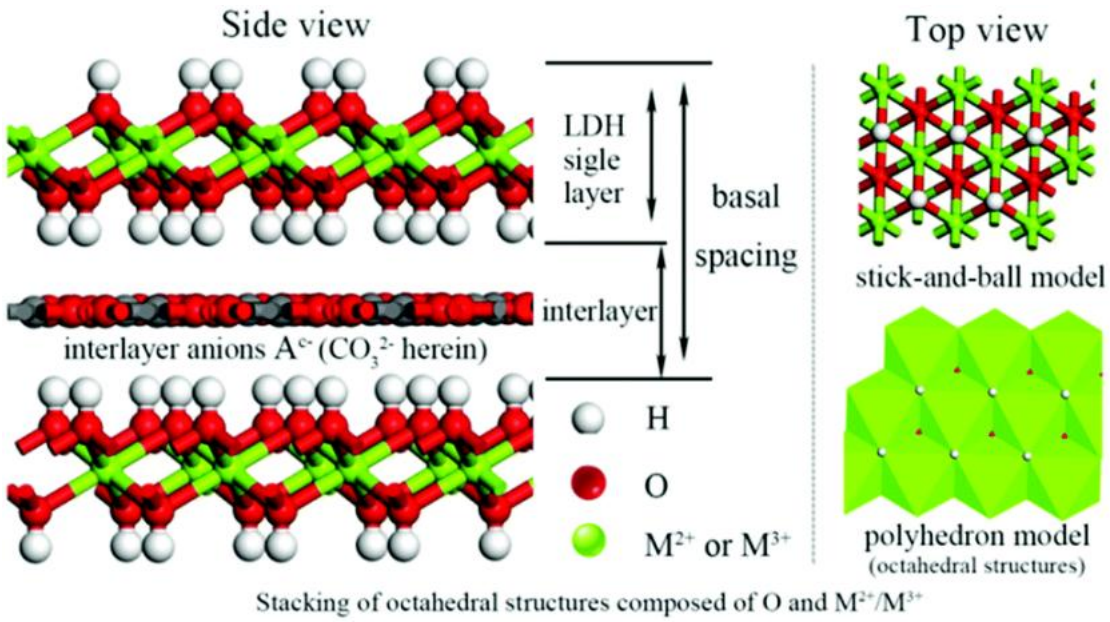

Figure I.12. Representative crystal structure of a layered double hydroxide (LDH), expressed as $[M_{1-x}^{2+}M_x'^{3+}(OH)_2][A_{x/c}^{c-}]$, where M^{2+} and M'^{3+} denote divalent and trivalent metal cations, respectively, and A^{c-} represents the interlayer anion [118].

LDHs offer high surface area, tunable compositions, and abundant ion transport pathways, making them ideal candidates for pseudocapacitive applications. For example, 3D nanostructured NiFe-LDH significantly enhances electron mobility and ion diffusion, proving effective in water splitting and energy storage devices [119]. Composite structures, such as NiCo-LDH on conductive textiles, provide a flexible yet high-capacitance electrode platform [120]. Additionally, MgAl-LDH has been used in environmental remediation for selectively adsorbing radioactive nuclides like uranium [121], and LDH–semiconductor heterojunctions are being developed to improve photocatalytic performance via enhanced charge carrier separation [122,123].

I.5. Opportunities and Challenges

In the context of emerging demands for miniaturized, flexible, and multifunctional energy storage systems—particularly for wearable electronics, portable sensors, and integrated micro-energy networks—supercapacitors have attracted increasing attention due to their high power density, rapid charge–discharge capability, and long cycle life. Nevertheless, their relatively low energy density and narrow working voltage window remain critical limitations that hinder broader practical deployment [124,125]. According to the energy density equation ($E = CV^2/2$, Equation 3), both high specific capacitance and a wide operating voltage are essential to enhance device performance [126,127]. Conventional approaches to address these limitations include incorporating pseudocapacitive materials such as transition metal oxides, hydroxides, and conductive polymers to improve capacitance, or using non-aqueous and asymmetric configurations to expand the voltage window [128,129]. However, these strategies often involve challenges, such as uncontrolled stacking of layered materials, that restrict ion accessibility, low-yield and costly solution processing for nanosheets [130,131], unstable interfaces between electrode and electrolyte, and the reliance on complex device configurations with current collectors, binders, and separators—all of which increase internal resistance and reduce integration flexibility [132,133].

Furthermore, the pursuit of self-sustainable microsystems necessitates the integration of energy storage components with various harvesting technologies [134], including photovoltaic, thermoelectric, or triboelectric generators. However, unified platforms that offer scalability, environmental compatibility, and multifunctionality are still lacking. In

addition, the development of electrolyte systems with broad electrochemical stability, especially those based on neutral or bio-compatible media, presents another important avenue [135,136]. To meet the increasing performance demands of modern microelectronics, future supercapacitor designs must achieve a careful balance among electrochemical efficiency, mechanical adaptability, and manufacturing scalability. Therefore, it is imperative to develop new material systems and fabrication strategies that are capable of producing high-performance, robust, and integrated micro-supercapacitors using low-cost, high-throughput, and environmentally benign processes [137-139].

I.6. Objectives

To address the challenges of low energy density, limited scalability, and poor interfacial compatibility in current flexible supercapacitors, this dissertation proposes an integrated and scalable fabrication strategy for high-performance micro-supercapacitors (MSCs), leveraging laser-assisted patterning techniques combined with functional material assembly. Specifically, a programmable laser-induced graphene (LIG) patterning process was developed to directly construct porous interdigitated electrodes on flexible polyimide (PI) substrates. This laser-based method not only enables high-resolution, mask-free microfabrication, but also provides a three-dimensional conductive scaffold with excellent wettability, which facilitates the uniform and binder-free deposition of few-layer $Ti_3C_2T_x$ MXene nanosheets through mask-assisted spraying. The resulting MXene-based symmetric MSCs exhibit high areal capacitance, strong mechanical flexibility, and stable performance under bending and large-area integration, and have been successfully extended to self-powered systems in combination with solar cells and biodegradable substrates.

Building on this platform, an asymmetric MSC was further developed by combining laser-induced graphene electrodes with electrochemically deposited pseudocapacitive materials. CoNi-layered double hydroxide (CoNi-LDH) with hydrogen vacancy engineering and FeOOH were selectively deposited onto the LIG-patterned positive and negative interdigitated electrodes, respectively, forming a LIG-CoNi-$LDH_{(v)}$//LIG-FeOOH architecture. This device operates efficiently within a wide voltage window of 1.8 V in neutral electrolytes without the need for metallic current collectors, separators, or polymer binders. The AMSC demonstrates significantly improved energy and power densities, enhanced interfacial adhesion, and long-term cycling stability, as well as ion compatibility in multi-cation systems (Li^+, Na^+, K^+, Ca^{2+}), thus offering great potential for integration into next-generation wearable, portable, and self-powered electronic systems.

Overall, this work presents a multifunctional and environmentally friendly manufacturing strategy that unites laser-based microstructuring, solution-processed nanomaterials, and electrochemical activation to construct flexible, scalable, and high-performance MSCs. The outcomes of this research are expected to provide new insights into the rational design of advanced micro-energy storage devices, and to contribute to the realization of sustainable and intelligent energy systems.

References

[1] M. Armand, J. M. Tarascon, Nature. 2008, 451, 652–657.

[2] M. Cui, X. Meng, Nanoscale Adv. 2020, 2, 5516–5528.

[3] Z. S. Iro, C. Subramani, S. S. Dash, Int. J. Electrochem. Sci. 2016, 11, 10628–10643.

[4] X.Huang, Z. Zeng, H. Zhang, Chem. Soc. Rev. 2013, 42, 1934–1946.

[5] J. R. Miller, P. Simon, Science. 2008, 321, 651–652.

[6] W. Zuo, R. Li, C. Zhou, Y. Li, J. Xia, J. Liu, Adv. Sci. 2017, 4, 1600539.

[7] I. Chotia, S. Chowdhury, IEEE Innovative Smart Grid Technologies-Asia. 2015, 1–6.

[8] X. Chen, R. Paul, L. Dai, Natl. Sci. Rev. 2017, 4, 453–489.

[9] C. Zhang, Z. Peng, C. Huang, B. Zhang, C. Xing, H. Chen, H. Cheng, J. Wang, S. Tang, Nano Energy. 2021, 81, 105609.

[10] P. S. NK, S. M. Jeong, C. S. Rout, Energy Adv. 2024, 3, 341–365.

[11] D. G. Wang, Z. Liang, S. Gao, C. Qu, R. Zou, Coord. Chem. Rev. 2020, 404, 213093.

[12] S. Saini, P. Chand, A. Joshi, J. Energy Storage. 2021, 39, 102646.

[13] Z. Y. Li, P. T. M. Bui, D. H. Kwak, M. S. Akhtar, O. B. Yang, Ceram. Int. 2016, 42, 1879–1885.

[14] S. Najib, E. Erdem, Nanoscale Adv. 2019, 1, 2817–2827.

[15] S. B. Aziz, F. Ali, H. Anuar, T. Ahamad, W. O. Kareem, M. A. Brza, M. F. Z. Kadir, Alexandria Eng. J. 2022, 61, 3985–3997.

[16] P. Sharma, T. S. Bhatti, Energy Convers. Manage. 2010, 51, 2901–2912.

[17] Y. J. Kim, Y. Masutzawa, S. Ozaki, M. Endo, M. S. Dresselhaus, J. Electrochem. Soc. 2004, 151, E199.

[18] L. Guo, M. Ding, D. Yan, M. E. Pam, S. Vafakhah, C. Gu, W. Zhang, P. V. Y. Alvarado, Y. Shi, H. Y. Yang, Desalination. 2020, 496, 114750.

[19] M. R. Lukatskaya, B. Dunn, Y. Gogotsi, Nat. Commun. 2016, 7, 12647.

[20] Z. Yu, L. Tetard, L. Zhai, J. Thomas, Energy Environ. Sci. 2015, 8, 702–730.

[21] D. P. Dubal, O. Ayyad, V. Ruiz, P. G. Romero, Chem. Soc. Rev. 2015, 44, 1777–1790.

[22] E. Faggioli, P. Rena, V. Danel, X. Andrieu, R. Mallant, H. Kahlen, J. Power Sources. 1999, 84, 261–269.

[23] A. Eftekhari, J. Mater. Chem. A. 2018, 6, 2866–2876.

[24] K. W. Nam, K. B. Kim, J. Electrochem. Soc. 2002, 149, A346.

[25] N. R. Chodankar, H. D. Pham, A. K. Nanjundan, J. F. S. Fernando, K. Jayaramulu, D. Golberg, Y. K. Han, D. P. Dubal, Small. 2020, 16, 2002806.

[26] A. Velasco, Y. K. Ryu, A. Boscá, A. Ladrón-de-Guevara, E. Hunt, J. Zuo, J. Pedrós, F. Calle, Sustain. Energy Fuels. 2021, 5, 1235–1254.

[27] J. Lin, Z. Peng, Y. Liu, F. Ruiz-Zepeda, R. Ye, E. L. G. Samuel, M. J. Yacaman, B. I. Yakobson, Nat. Commun. 2014, 5, 5714.

[28] M. F. El-Kady, R. B. Kaner, ACS Nano. 2014, 8, 8725–8729.

[29] A. Tiliakos, C. Ceaus, S. M. Iordache, E. Vasile, I. Stamatin, J. Anal. Appl. Pyrolysis. 2016, 121, 275–286.

[30] A. Tiliakos, C. Ceaus, S. M. Iordache, E. Vasile, I. Stamatin, Functionalization and Applications. Mater. Technol. 2018, 33, 340–356.

[31] A. Ladrón-de-Guevara, A. Boscá, J. Pedrós, E. Climent-Pascual, A. De Andrés, F. Calle, Appl. Surf. Sci. 2019, 467, 691–697.

[32] L. Cao, S. Zhu, B. Pan, X. Dai, W. Zhao, Y. Liu, W. Xie, Y. Kuang, X. Liu, Carbon. 2020, 163, 85–94.

[33] R. Ye, D. K. James, J. M. Tour, Adv. Mater. 2019, 31, e1803621.

[34] Z. Zhang, M. Song, J. Hao, K. Wu, C. Li, C. Hu, Carbon. 2018, 127, 287–296.

[35] Y. Chyan, R. Ye, Y. Li, S. P. Singh, C. J. Arnusch, J. M. Tour, ACS Nano. 2018, 12, 2176–2183.

[36] F. M. Vivaldi, A. Dallinger, A. Bonini, N. Poma, L. Sembranti, D. Biagini, P. Salvo, F. Greco, ACS Appl. Mater. Interfaces. 2021, 13, 30245–30260.

[37] Q. Shangguan, Y. Zhao, Z. Song, J. Wang, H. Yang, J. Chen, C. Liu, S. Cheng, W. Yang, Z. Yi, Diamond Relat. Mater. 2022, 128, 109273.

[38] C. F. Du, Q. H. Liang, Y. B. Luo, Y. Zheng, Q. Y. Yan, J. Mater. Chem. A. 2017, 5, 22442–22458.

[39] X. C. Tian, J. Jin, S. Q. Yuan, C. K. Chua, S. B. Tor, K. Zhou, Adv. Energy Mater. 2017, 7, 1700127.

[40] F. Zhang, M. Wei, V. V. Viswanathan, B. Swart, Y. Y. Shao, G. Wu, C. Zhou, Nano Energy. 2017, 40, 418–431.

[41] E. Menard, M. A. Meitl, Y. G. Sun, J. U. Park, D. J. L. Shir, Y. S. Nam, S. Jeon, J. A. Rogers, Chem. Rev. 2007, 107, 1117–1160.

[42] M. Singh, H. M. Haverinen, P. Dhagat, G. E. Jabbour, Adv. Mater. 2010, 22, 673–685.

[43] J. Z. Sun, B. Bao, M. He, H. H. Zhou, Y. L. Song, ACS Appl. Mater. Interfaces. 2015, 7, 28086–28099.

[44] B. Kang, W. H. Lee, K. Cho, ACS Appl. Mater. Interfaces. 2013, 5, 2302–2315.

[45] Z. H. Nie, E. Kumacheva, Nat. Mater. 2008, 7, 277–290.

[46] J. Pu, Z. Shen, C. Zhong, Q. Zhou, J. Liu, J. Zhu, H. Zhang, Adv. Mater. 2020, 32, 1903808.

[47] M. F. Montemor, S. Eugénio, N. Tuyen, R. P. Silva, T.M. Silva, M. J. Carmezim, Energies, 2020, 13, 5228.

[48] S. Dhere, Curr. Sci. 115, 436–449.

[49] S. Mehdigholami, M. Hamadanian, M. R. Memarzadeh, J. Mater. Sci.: Mater. Electron. 2024, 35, 2303.

[50] S. Nayak, A. Soam, J. Nanda, C. Mahender, M. Singh, D. Mohapatra, R. Kumar, J. Mater. Sci.: Mater. Electron. 2018, 29, 9361–9368.

[51] S. J. Uke, S. P. Mardikar, D. R. Bambole, Y. Kumar, G. N. Chaudhari, Mater. Sci. Energy Technol. 2020, 3, 446–455.

[52] H. S. Nam, J. S. Kwon, K. M. Kim, J. M. Ko, J. D. Kim, Electrochim. Acta. 2010, 55, 7443–7446.

[53] R. Yadav, R. Banoth, K. Singh, H. Borkar, K. Kumari, Mater. Chem. Phys. 2024, 328, 130004.

[54] K. Vamsikrishna, P. Usha, D. Venkatesh, T. Ramesh, Ceram. Int. 2024, 50, 30869–30878.

[55] T. N. Myasoedova, R. Kalusulingam, T. S. Mikhailova, Coatings. 2022, 12, 1625.

[56] F. Zhang, H. L. Hu, P. Gao, Battery Bimonthly. 2009, 39, 291–293.

[57] P. Forouzandeh, P. Ganguly, R. Dahiya, S. C. Pillai, J. Power Sources. 2022, 519, 230744.

[58] S. Chen, Y. Chang, A. Liu, Y. Wang, Z. Feng, J. Li, L. Jiao, Surf. Interface Anal. 2025, 56, 105581.

[59] M. Asghar, S. A. Zahra, Z. Khan, M. Ahmed, F. Nasir, M. Iqbal, M. A. Mohammad, A. Mahmood, Front. Mater. 2020, 7, 179.

[60] Y. Zhang, T. Ji, S. Hou, L. Zhang, Y. Shi, J. Zhao, X. Xu, J. Power Sources. 2018, 403, 109–117.

[61] P. Sundriyal, ECS Meeting Abstracts. 2022, 1, 42.

[62] Y. Li, H. Sun, Y. Yang, Y. Cao, W. Zhou, H. Chai, J. Colloid Interface Sci. 2020, 580, 298–307.

[63] L. L. Zhang, X. S. Zhao, Chem. Soc. Rev. 2009, 38, 2520–2531.

[64] Z. Yang, J. Tian, Z. Yin, C. Cui, W. Qian, F. Wei, Carbon. 2019, 141, 467–480.

[65] V. Kuzmenko, O. Naboka, M. Haque, H. Staaf, G. Go¨ransson, P. Gatenholm, P. Enoksson, Energy. 2015, 90, 1490–1496.

[66] Z. Fan, J. Yan, L. Zhi, Q. Zhang, T. Wei, J. Feng, M. Zhang, W. Qian, F. Wei, Adv. Mater. 2010, 22, 3723–3728.

[67] B. A. Ali, A. H. Biby, N. K. Allam, ChemElectroChem. 2020, 7, 1672–1678.

[68] C. Ma, L. Wu, M. Dirican, H. Cheng, J. Li, Y. Song, J. Shi, X. Zhang, Appl. Surf. Sci. 2021, 537, 147914.

[69] Z. Yang, J. Ren, Z. Zhang, X. Chen, G. Guan, L. Qiu, Y. Zhang, H. Peng, Chem Rev. 2015, 115, 5159–223.

[70] J. H. Kim, K. W. Nam, S. B. Ma, K. B. Kim, Carbon. 2006, 44, 1963–1968.

[71] H. J. Kim, J. Y. Yoon, G. B. Lee, S. H. Paik, G. W. Choi, D. Kim, B. M. Kim, G. S. Zi, J. S. Ha, ACS Appl. Mater. Interfaces. 2016, 8, 16016–16025.

[72] M. D. Stoller, S. Park, Y. Zhu, J. An, R. S. Ruoff, Nano Lett. 2008, 8, 3498–502.

[73] H. Jin, X. M. Wang, Z. R. Gu, Q. H. Fan, B. Luo, J. Power Sources. 2015, 273, 1156–1162.

[74] A. M. Abdelkader, N. Karim, C. Vallés, S. Afroj, K. S. Novoselov, S. G. Yeates, 2D Mater. 2017, 4, 035016.

[75] Y. Q. Liu, B. B. Zhang, Q. Xu, Y. Y. Hou, S. Y. Seyedin, S. Qin, G. G. Wallace, S. Beirne, J. M. Razal, J. Chen, Adv. Funct. Mater. 2018, 28, 1706592.

[76] W. B. Li, Y. H. Li, M. Su, B. X. An, J. Liu, D. Su, L. H. Li, F. Y. Li, Y. L. Song, J. Mater. Chem. A. 2017, 5, 16281–16288.

[77] S. G. Dai, H. Y. Guo, M. J. Wang, J. L. Liu, G. Wang, C. G. Hu, Y. Xi, J. Mater. Chem. A. 2014, 2, 19665–19669.

[78] J. Noh, C. M. Yoon, K. K. Yun, J. S. Jang, Carbon. 2017, 116, 470–478.

[79] M. Naguib, M. Kurtoglu, V. Presser, J. Lu, J. J. Niu, M. Heon, L. Hultman, Y. Gogotsi, M. W. Barsoum, Adv. Mater. 2011, 42, 4248–4253.

[80] Y. Xie, P. R. C. Kent, Phys. Rev. B. 2013, 87, 939–949.

[81] M. Naguib, O. Mashtalir, J. Carle, V. Presser, J. Lu, L. Hultman, Y. Gogotsi, M. W. Barsoum, ACS Nano. 2012, 6, 1322–1331.

[82] A. L. Ivanovskii, A. N. Enyashin, Russ. Chem. Rev. 2013, 82, 735–746.

[83] D. B. Xiong, X. F. Li, Z. M. Bai,S. G. Lu, Small. 2018, 14, 1703419.

[84] O. Mashtalir, M. Naguib, V. N. Mochalin, Y. Dall'Agnese, M. Heon, M. W. Barsoum, Y. Gogotsi, Nat. Commun. 2013, 4, 1716.

[85] S. Kajiyama, L. Szabova, K. Sodeyama, H. Iinuma, R. Morita, K. Gotoh, Y. Tateyama, M. Okubo, A. Yamada, ACS Nano. 2016, 10, 3334–3341.

[86] M. R. Lukatskaya, O. Mashtalir, C. E. Ren, Y. Dall'Agnese, P. Rozier, P. L. Taberna, M. Naguib, P. Simon, M. W. Barsoum, Y. Gogotsi, Science. 2013, 341, 1502–1505.

[87] J. Come, M. Naguib, P. Rozier, M. Barsoum, Y. Gogotsi, P. L. Taberna, M. Morcrette, P. Simon, J. Electrochem. Soc. 2012, 159, A1368–A1373.

[88] Q. Tang, Z. Zhou, P. Shen, J. Am. Chem. Soc. 2012, 134, 16909–16916.

[89] S. Murali, N. Quarles, L. L. Zhang, J. R. Potts, Z. Tan, Y. Lu, Y. Zhu, R. S. Ruoff, Nano Energy. 2013, 2, 764–768.

[90] M. Ghidiu, M. R. Lukatskaya, M. Q. Zhao, Y. Gogotsi, M. W. Barsoum, Nature. 2014, 516, 78.

[91] M. M. Hu, Z. J. Li, G. X. Li, T. Hu, C. Zhang, X. H. Wang, Adv. Mater. Technol. 2017, 2, 1700143.

[92] M. R. Lukatskaya, O. Mashtalir, C. E. Ren, Y. D. Agnese, P. Rozier, P. L. Taberna, M. Naguib, P. Simon, M. W. Barsoum, Y. Gogotsi, Science. 2013, 341, 1502–1505.

[93] M. Boota, B. Anasori, C. Voigt, M. Q. Zhao, M. W. Barsoum, Y. Gogotsi, Adv. Mater. 2016, 28, 1517–1522.

[94] H. Shirakawa, E. J. Louis, A. G. MacDiarmid, C. K. Chiang, A. J. Heeger, J. Chem. Soc. 1977, 16, 578–580.

[95] C. K. Chiang, C. R. Fincher, J. Y. W. Park, A. J. Heeger, H. Shirakawa, E. J. Louis, S. C. Gau, A. G. MacDiarmid, Phys. Rev. Lett. 1977, 39, 1098.

[96] X. Y. Cui, J. F. Hetke, J. A.Wiler, D. J. Anderson, D. C. Martin, Sens. Actuators A Phys. 2001, 93, 8–18.

[97] A. G. Macdiarmid, J. C. Chiang, A. F. Richter, A. J. Epstein, Synth. Met. 1987, 18, 285–290.

[98] K. Kaneto, K. Yoshino, Y. Inuishi, J. Jpn, Appl. Phys. 1982, 21, 567–568.

[99] J. Janata, M. Josowicz, Nat. Mater. 2003, 2, 19–24.

[100] K. Jurewicz, K. Lota, F. Béguin, J. Power Sources. 2006, 153, 413–418.

[101] M. Mastragostino, C. Arbizzani, F. Soavi, Solid State Ion. 2002, 148, 493–498.

[102] G. A. Snook, P. Kao, A. S. Best, J. Power Sources. 2011, 196, 1–12.

[103] H. Talbi, P. E. Just, L. H. Dao, J. Appl. Electrochem. 2003, 33, 465–473.

[104] D. D. Potphode, S. P. Mishra, P. Sivaraman, M. Patri, Electrochim. Acta. 2017, 230,

29–38.

[105] Q. F. Meng, K. F. Cai, Y. X. Chen, L. D. Chen, Nano Energy. 2017, 36, 268–285.

[106] K. Chi, Z. Y. Zhang, J. B. Xi, Y. A. Huang, F. Xiao, S. Wang, Y. Q. Liu, ACS Appl. Mater. Interfaces. 2014, 6, 16312–16319.

[107] P. Sharma, T. Bhatti, Energy Conv. Manag. 2010, 51, 2901–2912.

[108] J. Yan, T. Wei, J. Cheng, Z. Fan, M. Zhang, Mater. Res. Bull. 2010, 45, 210–215.

[109] H. Y. Ma, D. B. Kong, Y. Xu, X. Y. Xie, Y. Tao, Z. C. Xiao, W. Lv, H. D. Jang, Small. 2017, 13, 1701026.

[110] S. Cho, M. Kim, J. Jang, ACS Appl. Mater. Interfaces. 2015, 7, 10213–10227.

[111] J. K. Chang, M. T. Lee, W. T. Tsai, J. Power Sources. 2007, 166, 590–594.

[112] Y. M. He, W. J. Chen, X. D. Li, Z. X. Zhang, J. C. Fu, C. H. Zhao, E. Q. Xie, ACS Nano. 2013, 7, 174–182.

[113] Q. Lu, L. Liu, S. L. Yang, J. Liu, Q. Y. Tian, W. J. Yao, Q. W. Xue, M. X. Li, W. Wu, J. Power Sources. 2017, 361, 31–38.

[114] J. Wan, S. D. Lacey, J. Dai, W. Bao, M. S. Fuhrer, L. Hu, Chem. Soc. Rev. 2016, 45, 6742–6765.

[115] Q. Tao, B. J. Reddy, H. He, R. L. Frost, P. Yuan, J. Zhu, Mater. Chem. Phys. 2008, 112, 869–875.

[116] Q. Tao, Y. Zhang, X. Zhang, P. Yuan, J. Solid State Chem. 2006, 179, 708–715.

[117] J. Yu, Q. Wang, D. O'Hare, L. Sun, Chem. Soc. Rev. 2017, 46, 5950–5974.

[118] Q. Tao, H. He, R. L. Frost, P. Yuan, J. Zhu, Appl. Surf. Sci. 2009, 255, 4334–4340.

[119] L. Yu, H. Zhou, J. Sun, F. Qin, F. Yu, J. Bao, Y. Yu, S. Chen, Z. Ren, Energy Environ. Sci. 2017, 10, 1820–1827.

[120] G. Nagaraju, G. S. R. Raju, Y. H. Ko, J. S. Yu, Nanoscale. 2016, 8, 812–825.

[121] S. Ma, L. Huang, L. Ma, Y. Shim, S. M. Islam, P. Wang, L. D. Zhao, S. Wang, G. Sun, X. Yang, J. Am. Chem. Soc. 2015, 137, 3670–3677.

[122] Y. Ao, D. Wang, P. Wang, C. Wang, J. Hou, RSC Adv. 2015, 5, 54613–54621.

[123] S. Mancipe, F. Tzompantzi, R. Gomez, Appl. Clay Sci. 2017, 136, 67–74.

[124] C. Zhang, Z. Peng, C. Huang, B. Zhang, C. Xing, H. Chen, H. Cheng, J. Wang, S. Tang, Nano Energy. 2021, 81, 105609.

[125] C. Lu, X. Chen, Acc. Chem. Res. 2020, 53, 1468–1477.

[126] Z. Pan, J. Yang, Q. Zhang, M. Liu, Y. Hu, Z. Kou, N. Liu, X. Yang, X. Ding, H. Chen, J. Li, K. Zhang, Adv. Energy Mater. 2019, 9, 1802753.

[127] Y. Xie, H. Zhang, X. Jiang, L. Fan, J. Huang, W. Wang, H. Hu, Z. He, J. Colloid Interface Sci. 2025, 677, 12–20.

[128] M. M. Momeni, N. Moosavi, J. Alloys Compd. 2024, 1006, 176257.

[129] X. Xu, Z. Lu, L. Hua, J. Dong, Z. Guo, Y. Kou, J. Wu, H. Yu, Y. Wang, J. Colloid Interface Sci. 2025, 679, 643–655.

[130] R. Wang, S. Luo, C. Xiao, Z. Chen, H. Li, M. Asif, V. Chan, K. Liao, Y. Sun, Electrochim. Acta, 2021, 386, 138420.

[131] J. Yang, Z. Pan, Q. Yu, Q. Zhang, X. Ding, ACS Appl. Mater. Interfaces. 2019, 11, 5938–5946.

[132] X. Lin, X. Li, N. Yang, X. Li, J. Yao, W. Zhang, R. Yan, J. Xu, S. Komarneni, J. Power Sources. 2023, 560, 232712.

[133] H. Huang, X. Chu, H. Su, H. Zhang, Y. Xie, W. Deng, N. Chen, F. Liu, H. Zhang, B. Gu, W. Deng, J. Power Sources. 2019, 415, 1–7.

[134] X. Qu, Y. W. Kwon, S. Jeon, J. Jeong, W. Kang, Z. Jiang, C. Zhang, S. W. Hong, J. Colloid Interface Sci. 2023, 634, 715–729.

[135] A. Akhoondi, M. Y. Nassar, B. Yuliarto, H. Meskher, Synth. Sintering. 2023, 3, 200–212.

[136] Z. Pan, J. Yang, Q. Zhang, M. Liu, Y. Hu, Z. Kou, N. Liu, X. Yang, X. Ding, H. Chen, J. Li, K. Zhang, Adv. Energy Mater. 2019, 9, 1802753.

[137] C. Zhang, Z. Peng, C. Huang, B. Zhang, C. Xing, H. Chen, H. Cheng, J. Wang, S. Tang, Nano Energy. 2021, 81, 105609.

[138] X. Xu, Z. Lu, L. Hua, J. Dong, Z. Guo, Y. Kou, J. Wu, H. Yu, Y. Wang, J. Colloid Interface Sci. 2025, 679, 643–655.

[139] J. Yang, Z. Pan, Q. Yu, Q. Zhang, X. Ding, ACS Appl. Mater. Interfaces. 2019, 11, 5938–5946

Chapter II. Materials and Characterization Techniques

II.1. Reagents and Materials

All chemicals used in this study were commercially available and employed as received without further purification. Lithium fluoride (LiF), hydrochloric acid (HCl), sulfuric acid (H_2SO_4), potassium hydroxide (KOH), nickel nitrate hexahydrate ($Ni(NO_3)_2 \cdot 6H_2O$), cobalt nitrate hexahydrate ($Co(NO_3)_2 \cdot 6H_2O$), ferric nitrate nonahydrate ($Fe(NO_3)_3 \cdot 9H_2O$), polyvinyl alcohol (PVA, No. 1799), lithium chloride (LiCl), sodium chloride (NaCl), potassium chloride (KCl), and calcium chloride ($CaCl_2$) were all purchased from Sinopharm Chemical Reagent Co., Ltd. (China).

The Ti_3AlC_2 MAX phase precursor was obtained from Jilin 11 Technology Co., Ltd. (China). Polyimide (PI) film with a thickness of 0.23 mm was supplied by Shenzhen Beilong Electronic Materials Co., Ltd. (China).

II.2. Instrumentation

II.2.1 CO_2 Laser Processing System

In this study, the fabrication of laser-induced graphene (LIG) formed the core of the device engineering strategy. A high-power CO_2 laser processing system (Universal VLS2.30DT, USA) was employed to directly convert the surface of polyimide (PI) substrates into porous, conductive three-dimensional carbon frameworks under ambient conditions. This laser-assisted manufacturing approach is highly advantageous due to its chemical-free, and scalable nature, allowing for programmable design and rapid

prototyping of energy storage devices. The process leverages the localized photothermal effect of focused infrared laser irradiation, which decomposes the polymer backbone of PI, resulting in graphitic carbon domains with high conductivity and surface area.

The CO_2 laser system is fully integrated with computer-aided design (CAD) software, enabling precise pattern customization in terms of shape, size, and electrode geometry. This degree of flexibility is crucial for tailoring micro-supercapacitors to meet diverse application scenarios, including wearable electronics, microsensors, and integrated energy systems. The programmable nature of the system ensures reproducibility, resolution down to tens of micrometers, and compatibility with various substrates, making it highly suitable for fabricating next-generation flexible energy storage devices.

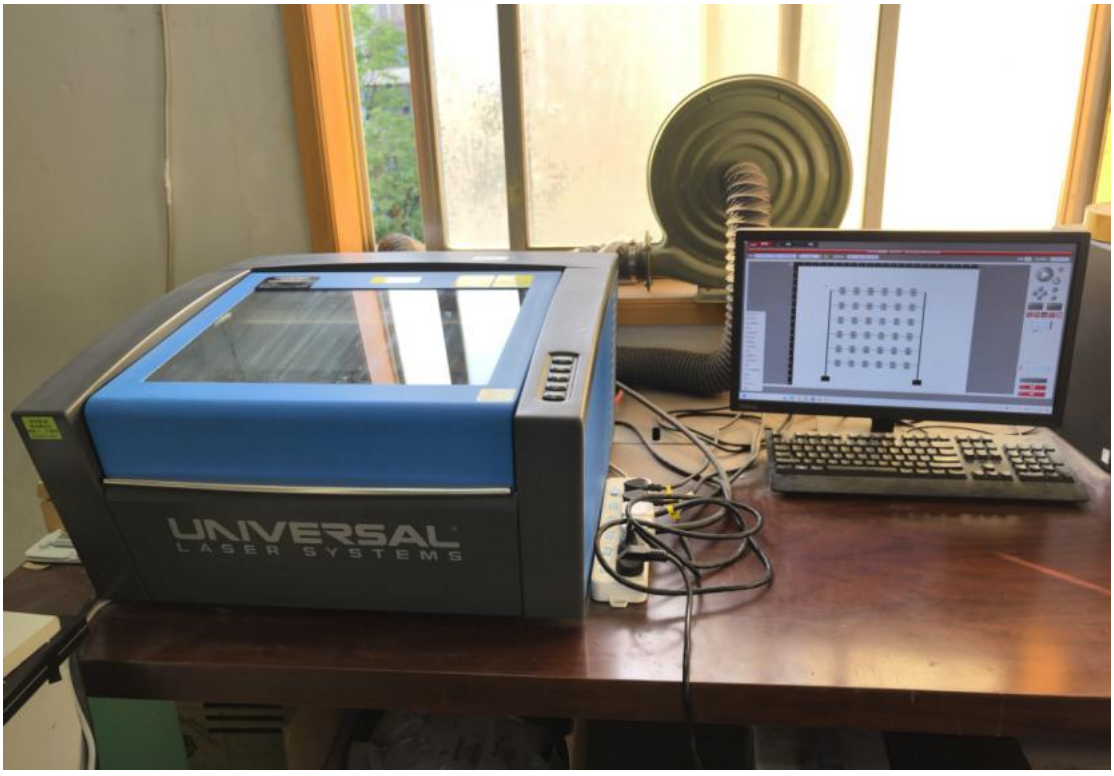

Figure II.1. Universal VLS2.30DT CO_2 laser processing system.

II.2.2 Freeze Dryer

Freeze drying, also known as lyophilization, is a low-temperature dehydration technique widely utilized in material science to preserve structure-sensitive nanomaterials without inducing thermal degradation or oxidation. In this process, the sample is first frozen and then subjected to vacuum conditions that enable direct sublimation of ice from the solid to the gas phase, bypassing the liquid state. This method is especially suitable for the processing of two-dimensional (2D) nanomaterials such as MXene, as it effectively maintains their layered morphology and surface chemistry during solvent removal. The absence of high-temperature drying prevents restacking, oxidation, and collapse of nanosheet structures—issues that often compromise electrochemical performance.

In this study, a commercial freeze dryer (SCIENTZ-18ND/D, China) was employed to process the delaminated MXene dispersion after selective etching of Ti_3AlC_2. The resulting D-MXene hydrogel was rapidly converted into dry, accordion-like D-MXene powder, which preserved the expanded interlayer spacing critical for further exfoliation. Compared to traditional oven-drying or air-drying methods, freeze drying not only significantly shortened processing time, but also ensured the retention of functional surface terminations (–OH, –F, –O), which are essential for stable colloidal dispersion and surface interaction with other active materials. The dry D-MXene powder obtained through this route was subsequently redispersed in deionized water and subjected to ultrasonication and centrifugation to efficiently produce few-layer MXene (FL-MXene) solutions. These FL-MXene dispersions exhibited excellent stability and uniformity, making them ideal for further applications such as spray coating, ink formulation, and integration into flexible micro-supercapacitors.



Figure II.2. SCIENTZ-18ND/D commercial freeze dryer.

II.3. Characterization

II.3.1 Scanning Electron Microscopy (SEM)

Scanning Electron Microscopy (SEM) is extensively used for investigating surface morphology, due to its ability to reveal detailed topographical features. The technique operates by directing a high-energy electron beam onto the specimen surface, which generates various signal outputs—primarily secondary electrons. These electrons are collected to construct high-resolution images that provide insights into the surface architecture of the material. In addition to secondary electron emission, the interaction between the electron beam and the specimen also produces characteristic X-rays. These X-rays can be analyzed using Energy-Dispersive Spectroscopy (EDS) to determine the

elemental composition and distribution, thus enabling comprehensive elemental mapping [1]. In this study, SEM imaging of the prepared samples was conducted using a ZEISS Sigma 360 field emission scanning electron microscope.



Figure II.3. ZEISS Sigma 360 field emission scanning electron microscope.

II.3.2 Transmission Electron Microscopy (TEM)

Transmission Electron Microscopy (TEM) enables high-resolution characterization of the microstructure and morphology of the synthesized materials. Through focused imaging of selected regions, well-defined lattice fringes can be directly visualized, offering insights into the crystallographic structure. Furthermore, elemental mapping of specific areas allows for precise analysis of elemental distribution across the sample surface,

contributing to a comprehensive understanding of the material's composition. In this work, transmission electron microscopy (TEM, JEOL JEM-2100F, Japan) was used at an accelerating voltage of 200 kV to characterize FL-MXene samples, which were prepared by dropping a few droplets of the dispersion onto copper grids and drying overnight in air.



Figure II.4. JEM-2100F transmission electron microscope instrument.

II.3.3 X-ray Diffraction (XRD)

X-ray Diffraction (XRD) is a widely employed technique for determining the phase composition and crystallographic structure of materials. The method operates by irradiating a sample with monochromatic X-rays, which interact with the atomic planes within the material, producing diffracted beams at characteristic angles and intensities. These diffraction patterns, governed by the orientation and spacing of the crystal planes, yield vital information about the material’s crystal structure and phase constitution. When the incident X-ray beam strikes the sample, the electric field component of the wave

interacts with the electrons of the constituent atoms, inducing the emission of secondary waves that retain the same wavelength as the incident radiation. The resulting diffraction intensity is closely related to the atomic number (Z) of the scattering atoms, meaning that heavier elements typically contribute more strongly to the detected signal. Constructive interference of these scattered waves occurs when Bragg's law is satisfied, which is mathematically expressed in Eq. 2.1:

$$n\lambda = 2d\sin\theta \qquad \text{Eq.2.1}$$

where n is the diffraction order, λ is the wavelength of the incident X-ray, d represents the interplanar spacing between atomic layers, and θ is the Bragg angle—the angle between the incident beam and the atomic plane. Variations in the position and intensity of diffraction peaks reflect differences in crystal symmetry and atomic arrangement, enabling phase identification and structural analysis [2].

The crystalline structures of various samples in this study were examined using X-ray diffraction (XRD) techniques. Conventional XRD measurements were performed on a Bruker D8 Advance diffractometer (Germany) equipped with a Cu Kα radiation source (λ = 1.54056 Å). The instrument operated at an accelerating voltage of 45 kV and a tube current of 200 mA. Diffraction patterns were recorded over a 2θ range of 3° to 80° at a scanning rate of 2° min^{-1} to analyze the bulk phase composition of the samples.



Figure II.5. Bruker D8 Advance XRD instrument.

In addition, micro-area X-ray diffraction (micro-XRD) analysis was performed using a Rigaku SmartLab diffractometer (Japan) to obtain localized crystallographic information from specific regions of interest on the electrode surface. This technique was particularly applied to characterize the interdigitated microelectrodes after electrochemical deposition, with the aim of identifying the microscale phase composition of the deposited materials. Compared to conventional XRD, micro-XRD offers higher spatial resolution, making it especially suitable for heterogeneous or patterned surfaces. During the measurement, the scan was conducted at a rate of 2° min^{-1} over a 2θ range of 10° to 90°, which allowed for the detection of distinct diffraction peaks from the electrodeposited nanostructures while minimizing background interference from the underlying substrate. This localized

structural characterization provided critical insights into the crystallinity and phase evolution of the active materials confined to the microscale electrode areas.



Figure II.6. Rigaku Smartlab micro-XRD instrument.

II.3.4 X-ray Photoelectron Spectroscopy (XPS)

X-ray Photoelectron Spectroscopy (XPS) is a surface-sensitive analytical technique based on the photoelectric effect, wherein irradiation of a material by electromagnetic radiation induces the emission of low-energy electrons, known as photoelectrons [3-5]. In XPS, the incident X-rays—typically of known energy—excite core-level electrons within atoms near the material's surface. The kinetic energy of the emitted photoelectrons is measured, and the corresponding binding energy is calculated to identify the elemental composition and chemical states present.

During measurement, non-conductive samples may accumulate positive surface charges, resulting in a shift in the measured kinetic energy and leading to inaccuracies in the binding energy determination. To compensate for this, a flood gun is employed to introduce low-energy electrons and neutralize surface charging. Additionally, internal referencing is commonly used; the C 1s peak from adventitious carbon (assigned at 284.8 eV) serves as a standard in most laboratories. Therefore, the C 1s spectrum is typically recorded both at the beginning and end of each measurement session to ensure energy calibration accuracy [6].

In this study, XPS measurements were conducted using a Thermo Scientific K-Alpha spectrometer (USA) equipped with a monochromatic Al Kα X-ray source (photon energy = 1486.7 eV), operating at 225 W (15 kV). This configuration enabled precise surface elemental and chemical state analysis of the synthesized materials.



Figure II. 7. Thermo Scientific K-Alpha XRS instrument.

II.3.5 Contact Angle Measurements

The wettability of the sample surfaces was evaluated via both static and dynamic water contact angle (CA) measurements. The magnitude of the contact angle provides information on the surface wettability and chemical affinity of the material. Contact angles between 0° and 90° indicate hydrophilic surfaces, while values ranging from 90° to 150° reflect hydrophobic behavior. Superhydrophobicity is characterized by a contact angle exceeding 150°, implying a highly water-repellent surface where water droplets easily roll off.

To analyze the time-dependent wetting behavior, dynamic contact angle measurements were carried out using a dynamic contact angle analyzer (SDC 350KS, China). During testing, the droplet–surface interaction was recorded in real-time using a high-resolution camera. Water droplets were dispensed onto the substrate surface, and the variation in contact angle was tracked as a function of time. Representative snapshots were extracted at specific intervals (e.g., 1, 5, and 60 s) to quantify the temporal evolution of the contact angle. This method provided deeper insight into the dynamic wetting properties of the samples, including absorption rate and liquid spreading behavior.



Figure II.8. SDC 350KS dynamic contact angle analyzer.

II.3.6 Electrical Conductivity Measurements

The sheet resistance of the fabricated samples was measured using a four-point probe resistivity tester (HPS2661, China). The four-point probe method is a widely adopted technique for accurately assessing the surface conductivity of thin films and layered materials. It operates by applying a constant current through the outer two probes, while the inner two probes detect the resulting voltage drop across a defined distance. This configuration effectively eliminates the influence of contact resistance, thereby providing a more precise evaluation of intrinsic sheet resistance.

In this study, for each set of laser processing parameters, three laser-induced graphene (LIG) strips with dimensions of 5 mm in width and 15 mm in length were tested. The

measurements were conducted under ambient conditions, and the average values along with standard deviations were reported to ensure reproducibility and statistical reliability.



Figure II.9. HPS2661 four-point probe resistivity tester.

II.4. Electrochemical Performance Parameters

To comprehensively evaluate the electrochemical performance of the fabricated micro-supercapacitors, several key parameters were systematically analyzed. These included areal capacitance (CA), areal capacity (QA), areal energy density (EA), and areal power density (PA), which collectively reflect the energy storage and power output capabilities of the device per unit area. In addition, electrochemical impedance spectroscopy (EIS) was employed to investigate the charge transfer resistance and ion diffusion behavior

within the electrodes. The cycling stability of the devices was also assessed to determine their long-term reliability under repeated charge–discharge conditions.

II.4.1. Electrode and Electrolyte

All electrochemical measurements were conducted at room temperature using a Squidstat Plus 2444 electrochemical workstation (USA) in either a standard three-electrode or two-electrode configuration, depending on the experimental setup.

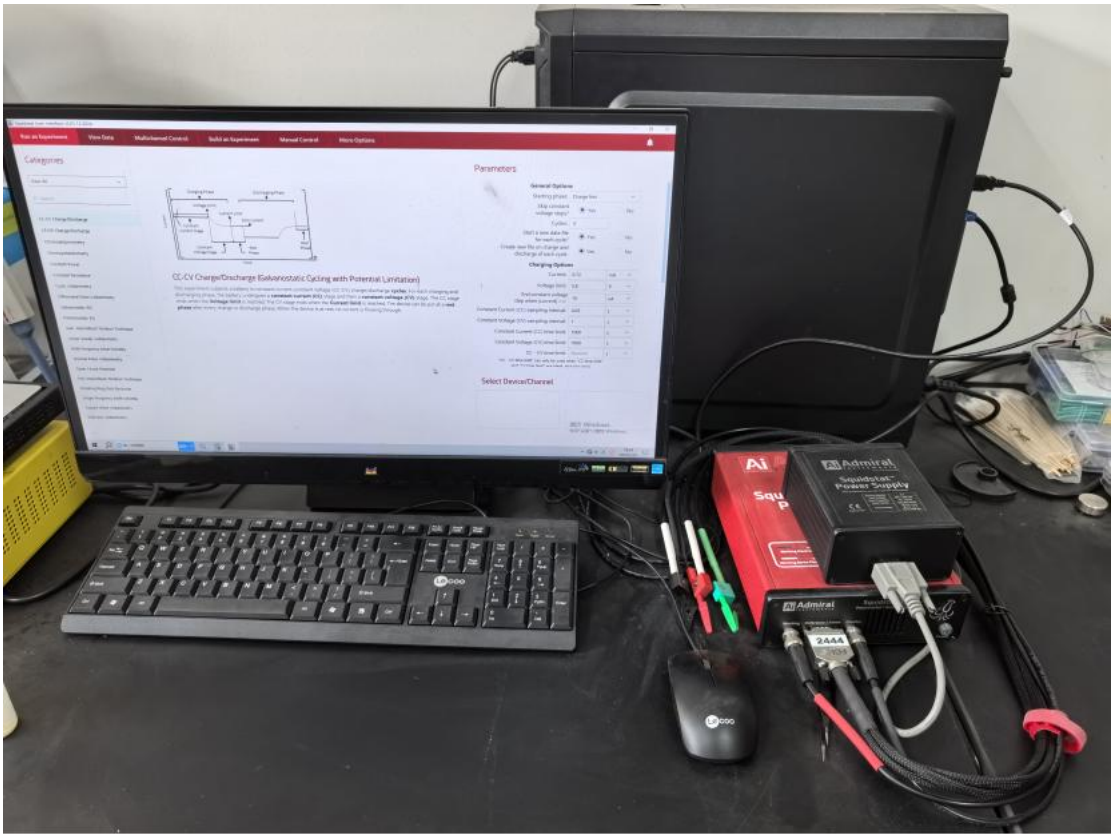

Figure II.10. Squidstat Plus 2444 electrochemical workstation.

In the three-electrode system, the working electrode consisted of the as-prepared supercapacitor electrode, while a platinum sheet and an Ag/AgCl electrode (saturated KCl) served as the counter and reference electrodes, respectively. A 5 M LiCl aqueous

solution was employed as the electrolyte to ensure high ionic conductivity and stability during testing.

For two-electrode measurements, the positive and negative electrodes of the fabricated supercapacitor device were directly connected as the working and counter electrodes. The electrolyte used in this configuration was either a PVA/H_2SO_4 gel or a PVA/LiCl gel, depending on the device type and targeted performance. This setup was utilized to evaluate the integrated performance of the assembled device under practical conditions.

II.4.2. Cyclic Voltammetry (CV)

Cyclic Voltammetry (CV) can not only be employed as a synthetic tool under specific electrochemical conditions, but it is also a classical technique widely used for probing redox activity and charge storage behavior [7]. During CV analysis, the potential is linearly swept within a defined potential window, while the resulting current response is simultaneously recorded. As the applied potential increases during the forward scan, oxidation reactions occur at the electrode surface or within the electrolyte, resulting in an anodic current. Conversely, during the reverse scan, the potential is reduced, leading to the reduction of electroactive species and the generation of a cathodic current.

In the investigation of symmetric MXene-based supercapacitors, CV measurements were performed in a two-electrode configuration across a potential window of 0–0.6 V, using scan rates ranging from 10 to 500 mV s^{-1}. For LIG-CoNi-$LDH_{(v)}$//LIG-FeOOH asymmetric supercapacitors, a more comprehensive CV analysis was carried out in both three-electrode and two-electrode setups. In the three-electrode configuration, the positive electrode was tested over a potential window of 0 to 1.0 V (*vs.* Ag/AgCl), and

the negative electrode over –0.8 to 0 V (*vs.* Ag/AgCl), at scan rates from 10 to 100 mV s^{-1}. Subsequently, full device CV curves were recorded in the two-electrode system within a broader voltage range of 0 to 1.8 V at the same scan rate conditions (10–100 mV s^{-1}), allowing for evaluation of the complete cell behavior.

II.4.3. Galvanostatic Charge–Discharge (GCD)

Galvanostatic Charge–Discharge (GCD) is a fundamental electrochemical technique used to evaluate the capacitive performance of energy storage devices. In this method, a constant current is applied while recording the voltage response as a function of time. The shape and symmetry of the GCD curves provide insight into the charge storage mechanism, internal resistance, and reversibility of the electrode reactions. Additionally, the discharge duration at various current densities allows for the calculation of capacitance, energy density, and power density.

In the study of symmetric MXene-based supercapacitors, GCD measurements were carried out in a two-electrode configuration over a potential window of 0–0.6 V, with applied current densities ranging from 0.2 to 4 mA cm^{-2}. For LIG-CoNi-$LDH_{(v)}$//LIG-FeOOH asymmetric supercapacitor systems, tests were performed in both three-electrode and two-electrode configurations. In the three-electrode setup, the positive electrode was tested within a potential window of 0 to 1.0 V (*vs.* Ag/AgCl), and the negative electrode within –0.8 to 0 V (*vs.* Ag/AgCl), using current densities from 0.5 to 10 mA cm^{-2}. Subsequently, full-device GCD curves were recorded in the two-electrode configuration under a broader potential range of 0 to 1.8 V, at current densities ranging from 0.25 to 8 mA cm^{-2}, to assess the overall charge–discharge behavior of the assembled supercapacitor.

II.4.4. Electrochemical Impedance Spectroscopy (EIS)

Electrochemical Impedance Spectroscopy (EIS) is a powerful diagnostic technique widely used to investigate the interfacial properties and charge transport behavior at the electrode–electrolyte interface [8-11]. It involves applying a small-amplitude sinusoidal voltage (or current) perturbation over a range of frequencies and measuring the resulting current (or voltage) response. The impedance response is typically plotted as a Nyquist plot, which provides valuable insights into both resistive and capacitive elements of the electrochemical system.

The selection of frequency range is critical, as it governs the type of information extracted from the spectrum. In the high-frequency region, where faradaic processes are negligible, the intercept on the real axis corresponds to the solution resistance (R_s)—reflecting the combined resistance of the electrolyte and electrical connections. In contrast, the low-frequency region reveals kinetic parameters related to charge transport and storage. Here, the semicircle diameter in the Nyquist plot corresponds to the charge transfer resistance (R_{ct}), which reflects the ease with which electrons move across the electrode–electrolyte interface. A lower R_{ct} value indicates faster redox kinetics and more efficient electrochemical activity.

In this study, EIS measurements were conducted over a frequency range of 100 mHz to 100 kHz to evaluate the resistive behavior of the electrodes. The results were used to analyze the intrinsic resistance, charge transfer characteristics, and ion diffusion dynamics of the electrode materials, thereby assisting in understanding the overall electrochemical performance of the supercapacitors.

II.4.4. Ragone Plot Analysis

The Ragone plot is a widely adopted and effective graphical tool for evaluating and comparing the electrochemical performance of energy storage devices, including supercapacitors. By plotting energy density against power density, this representation enables a comprehensive visualization of a device's energy–power relationship, thereby providing critical insight into its practical application potential. Unlike single-parameter analyses, the Ragone plot facilitates a rapid horizontal comparison among various systems—such as batteries, supercapacitors, and hybrid devices—highlighting trade-offs between energy delivery capacity and response speed.

To construct a Ragone plot for areal devices, it is necessary to first calculate the areal capacitance (CA) from galvanostatic charge–discharge (GCD) curves. The areal energy density (EA) and areal power density (PA) can then be derived using the following equations (2.2 – 2.4)[12]:

$$C_A = \frac{I \times \Delta t}{A \times \Delta V} \qquad \text{Eq.2.2}$$

$$E_A = \frac{C_A \times V^2}{2 \times 3600} \qquad \text{Eq.2.3}$$

$$P_A = \frac{E_A \times 3600}{t} \qquad \text{Eq.2.4}$$

Where I is the discharge current (A), Δt is the discharge duration obtained from the GCD curve (s), A is the total electrochemically active area of the interdigitated electrodes (cm^2), and ΔV is the operating voltage window obtained from the GCD curve (V), V is the applied voltage, t is the discharge time.

In this work, GCD measurements were used to calculate the areal capacitance of the fabricated micro-supercapacitors under various current densities. These values were then substituted into Equations (2.3) and (2.4) to determine the corresponding areal energy and power densities.

II.4.5. Cycling Stability Evaluation

Supercapacitors have long been recognized for their exceptional cycling stability, which is a crucial parameter for evaluating their suitability in practical energy storage applications. Unlike batteries, which often suffer from capacity fading due to irreversible redox reactions and structural degradation, supercapacitors rely on electrostatic charge accumulation or surface-confined faradaic processes, allowing them to sustain thousands of charge–discharge cycles with minimal performance loss.

A robust electrode structure and stable electrode–electrolyte interface are essential for maintaining long-term operational durability. Assessing the cycling performance typically involves repeated cyclic voltammetry (CV) or galvanostatic charge–discharge (GCD) cycling. In CV-based assessments, the device is subjected to hundreds or even thousands of continuous voltage sweeps, and the gradual change in current response or integrated area under the curve is used to evaluate capacity retention. However, due to its closer resemblance to real-world usage scenarios, GCD-based cycling tests are considered more representative and reliable for practical durability evaluations. They simulate continuous charging and discharging under constant current conditions, reflecting the mechanical and electrochemical resilience of the electrode materials.

References

[1] R. Sharma, W. C. D. Yang, Microscopy. 2024, 73, 79–100.

[2] H. Stanjek, W. Häusler, Hyperfine Interact. 2004, 154, 107–119.

[3] J. Timoshenko, B. R. Cuenya, Chem. Rev. 2021, 121, 882–961.

[4] R. Mom, L. Frevel, J. J. Velasco-Velez, M. Plodinec, A. Knop-Gericke, R. Schlogl, J. Am. Chem. Soc. 2019, 141, 6537–6544.

[5] M. Favaro, W. S. Drisdell, M. A. Marcus, J. M. Gregoire, E. J. Crumlin, J. A. Haber, J. Yano, ACS Catal. 2017, 7, 1248–1258.

[6] G. Greczynski, L. Hultman, J. Appl. Phys. 2022, 132, 1–54.

[7] N. Elgrishi, K. J. Rountree, B. D. McCarthy, E. S. Rountree, T. T. Eisenhart, J. L. Dempsey, J. Chem. Educ. 2017, 95, 197–206.

[8] W. Chen, B. Wu, Y. Wang, W. Zhou, Y. Li, T. Liu, C. Xie, L. Xu, S. Du, M. Song, D. Wang, Y. liu, Y. Li, J. Liu, Y. Zou, R. Chen, C. Chen, J. Zheng, Y. Li, J. Chen, S. Wang, Energy Environ. Sci. 2021, 14, 6428–6440.

[9] K. Gu, D. Wang, C. Xie, T. Wang, G. Huang, Y. Liu, Y. Zou, L. Tao, S. Wang, Angew. Chem., Int. Ed. Engl. 2021, 60, 20253–20258.

[10] C. Xie, W. Chen, S. Du, D. Yan, Y. Zhang, J. Chen, B. Liu, S. Wang, Nano Energy. 2020, 71, 104653.

[11] P. Zhai, C. Wang, Y. Zhao, Y. Zhang, J. Gao, L. Sun, J. Hou, Nat. Commun. 2023, 14, 1873.

[12] L. Li, J. Zhang, Z. Peng, Y. L, C. Gao, Y. Ji, R. Ye, N. D. Kim, Q. Zhong, Y. Yang, H. Fei, G. Ruan, J. M. Tour, Adv. Mater. 2016, 28, 838–845.

Chapter III: Mask-Assisted Spray Deposition of Additive-Free MXene on Laser-Induced Graphene for Flexible Symmetric Micro-Supercapacitors

III.1. Abstract

Flexible and scalable fabrication strategies for high-performance micro-supercapacitors (MSCs) are critical for next-generation wearable electronics. In this study, we propose a facile and programmable method that integrates laser-induced graphene (LIG) patterning with mask-assisted spray coating of additive-free MXene ink to fabricate flexible symmetric MSCs. The process involves direct laser irradiating of polyimide (PI) substrates covered with adhesive masks to create interdigitated LIG electrodes, followed by uniform deposition of few-layer $Ti_3C_2T_x$ (FL-MXene) nanosheets. Electrochemical tests demonstrate that increasing the MXene ink concentration improves areal capacitance. Under a current density of 0.2 mA cm^{-2}, the optimized LIG-MXene-5 MSC delivers a high areal capacitance of 43.80 mF cm^{-2} and achieves an energy density of 2.103 μWh cm^{-2} at a power density of 58.80 μW cm^{-2}. Moreover, the integration of MSC units in various series-parallel configurations (4S, 4P, 2P2S) allows for tunable voltage and current outputs, demonstrating excellent flexibility and scalability. The approach is further extended to fabricate large-area 6S×6P MSC arrays and self-powered systems integrating solar cells and LEDs. Additionally, the method is validated on biodegradable paper substrates, indicating its compatibility with green and low-cost energy solutions. This work provides a robust, patternable, and scalable fabrication strategy for high-

performance MXene-based MSCs, offering great potential for flexible and sustainable on-chip energy storage platforms.

Keywords: MXene; laser-induced graphene (LIG); micro-supercapacitors; flexible electronics; spray coating; areal capacitance; scalable fabrication; self-powered system.

III.2. Introduction

With the rapid advancement of flexible electronics, the Internet of Things (IoT), and micro-sensor technologies, there is an increasing demand for high-performance micro-scale energy storage devices [1,2]. Especially in wearable electronics, self-powered systems, and on-chip integration platforms, energy storage units must not only be lightweight and miniaturized, but also exhibit high energy density, excellent mechanical flexibility, and fast charge–discharge capabilities [3-5]. Among various storage technologies, micro-supercapacitors (MSCs) have emerged as a promising alternative to conventional microbatteries, owing to their high power density, long cycle life, and fast electrochemical response [6-8]. Achieving scalable and integrated MSCs with fine electrode structures is thus critical for enabling advanced flexible energy systems [9].

In recent years, printed electronics have gained significant traction as a fabrication strategy for patterned microelectrodes, offering advantages such as digital programmability, high material utilization, and low-temperature processing [10]. Compared to traditional microfabrication methods like photolithography and sputtering [11,12], printing techniques, such as inkjet printing [13], screen printing [14,15] and direct ink writing (DIW) [16,17], enable more flexible and cost-effective manufacturing across diverse substrates. However, the print quality heavily depends on the formulation

and rheological behavior of functional inks [18,19]. To improve film uniformity and resolution, additives, such as surfactants or low-boiling-point solvents, are commonly incorporated to adjust viscosity and surface tension. Unfortunately, these additives often require complex post-treatments (e.g., thermal annealing or chemical washing), which are incompatible with many substrates and may deteriorate the performance of the active materials [20,21]. Consequently, the development of additive-free inks is crucial for scalable, low-cost, and efficient printing of MSC electrodes [22].

MXenes, a family of two-dimensional (2D) transition metal carbides and nitrides (e.g., $Ti_3C_2T_x$), have attracted considerable attention due to their outstanding electrical conductivity, high volumetric capacitance, and rich surface functionalization [23-25]. These characteristics make them ideal candidates for flexible energy storage applications. MXenes can form stable aqueous dispersions, enabling the fabrication of freestanding films and composite electrodes [26-31]. Despite these advantages, MXene nanosheets tend to restack during film formation, which limits electrolyte accessibility and reduces charge transport, thus impairing device performance [32]. Previous studies have explored MXene integration via photolithography and printing methods [33,34]. However, achieving printable rheology often requires high ink concentrations, increasing cost and exacerbating aggregation and sedimentation issues, ultimately compromising device efficiency.

To address these challenges, this study proposes a scalable and programmable fabrication strategy that integrates laser-induced graphene (LIG) patterning with mask-assisted spray deposition of additive-free MXene inks for constructing high-performance, flexible symmetric MSCs [35,36]. Laser processing offers high patterning resolution,

mask-free operation, and excellent substrate adaptability, making it particularly suitable for building interdigitated electrode architectures. In this work, LIG structures were precisely formed on polyimide substrates using CO_2 laser irradiation through adhesive masking. These LIG frameworks provided a 3D porous scaffold that enabled the uniform deposition of few-layer $Ti_3C_2T_x$ nanosheets, enhancing interfacial adhesion and charge transport. The resulting MSCs exhibited tunable electrical output through various series–parallel configurations and demonstrated reliable operation under mechanical deformation. Furthermore, this method was successfully extended to fabricate large-area integrated MSC arrays and self-powered systems using solar cells, and was validated on biodegradable paper substrates, underscoring its versatility and sustainability. Overall, this work offers a robust, scalable platform for fabricating high-performance MXene-based MSCs with broad applicability in flexible, self-powered, and environmentally friendly electronic systems.

III.3. Experimental Section

III.3.1. Experimental Materials

All chemicals used in this study were commercially available and used without further purification. Lithium fluoride (LiF), hydrochloric acid (HCl), sulfuric acid (H_2SO_4), and polyvinyl alcohol (PVA, MACKLIN No.1799) were purchased from Sinopharm Chemical Reagent Co., Ltd. (China). Polyimide (PI) film with a thickness of 0.23 mm was obtained from Shenzhen Beilong Electronic Materials Co., Ltd. (China). The Ti_3AlC_2 MAX phase precursor was purchased from Jilin 11 Technology Co., Ltd. (China).

III.3.2. Preparation of Delaminated Multilayer $Ti_3C_2T_x$ (D-MXene)

Delaminated multilayer $Ti_3C_2T_x$ (D-MXene) was synthesized by selectively etching aluminum from the Ti_3AlC_2 MAX phase precursor. Specifically, 1 g of LiF was dissolved in 20 mL of 6 M HCl under magnetic stirring for 5 min. Subsequently, 1 g of Ti_3AlC_2 powder was slowly added, and the mixture was stirred continuously at 35 °C for 48 h. The resulting acidic suspension was repeatedly washed with deionized (DI) water and centrifuged at 3500 rpm for 5 min to remove residual impurities until the supernatant pH reached approximately 6, producing a black sediment settled at the bottom of the centrifuge tube. Finally, D-MXene powder was obtained by freeze-drying the collected sediment.

III.3.3. Preparation of Few-Layer $Ti_3C_2T_x$ Nanosheets (FL-MXene)

To prepare few-layer $Ti_3C_2T_x$ nanosheets (FL-MXene), 0.1 g of D-MXene powder was dispersed in 50 mL DI water and sonicated in an ice bath for 30 min, followed by centrifugation at 3500 rpm for 30 min to remove incompletely delaminated multilayer MXene. The ink-like supernatant with a concentration of approximately 5 mg mL^{-1} was collected as FL-MXene ink, which was further sonicated for 5 min prior to spraying.

III.3.4. Fabrication of Flexible Symmetric MXene Micro-Supercapacitors

III.3.4.1. Preparation and Patterning of Laser-Induced Graphene (LIG)

Laser-induced graphene (LIG) was fabricated at room temperature under ambient conditions by irradiating a polyimide (PI) substrate covered with a mask using a high-power CO_2 laser system (Universal VLS2.30DT). A thin acrylic adhesive layer was applied to ensure good adhesion between the mask and the PI substrate. Laser power and

scanning speed were optimized to achieve a structurally intact and conductive three-dimensional carbon network. The interdigitated electrode pattern, designed using AutoCAD software, consisted of 12 microelectrodes, each measuring 6 mm in length and 0.6 mm in width, with electrode gaps of approximately 0.3 mm.

III.3.4.2. Preparation of Gel Electrolyte

The polymer gel electrolyte (PVA/H_2SO_4) was prepared by dissolving 1 g of polyvinyl alcohol (PVA, MACKLIN No.1799) in 10 mL DI water, heating and stirring at 90 °C for 3 h until a clear solution was obtained, and then cooling to room temperature. Next, 1 g of concentrated sulfuric acid (H_2SO_4) was added, and the mixture was stirred for an additional 2 h. The prepared gel was degassed in a vacuum drying oven at room temperature for 2 h to eliminate bubbles.

III.3.4.3. Assembly of MXene-Based Symmetric Micro-Supercapacitors

Using a low-cost spray gun, 1 mL of FL-MXene ink (5 mg mL^{-1}) was directly sprayed onto the LIG interdigitated electrode substrate, with a hot air gun employed to rapidly dry the MXene layer. The sprayed electrodes were dried overnight in a vacuum oven at 60 °C to remove residual moisture. After removing the mask, silver paste (Pellco) was applied to the common electrode area to enhance electrical contact, and copper tape was used to extend connections to an electrochemical workstation. The common electrode area was sealed with Kapton tape to prevent the silver paste from reacting with the electrolyte and oxidation. Approximately 0.25 mL of the prepared PVA/H_2SO_4 gel electrolyte was then dropped onto the active areas of both electrodes, and the assembled device was dried overnight in a vacuum desiccator (≈120 mm Hg) to ensure good electrolyte-electrode

contact and complete curing, resulting in flexible, quasi-solid-state symmetric MXene-based micro-supercapacitors.

III.3.5. Material Characterization

The sheet resistance of the samples was measured using a four-probe resistivity tester (HPS2661, China). For each laser condition utilized in this study, three LIG stripes measuring 5 mm in width and 15 mm in length were tested to obtain the average resistance and corresponding standard deviation are summarized in **Table III.1**. For LIG-MXene-X samples (X indicating concentrations) prepared by spraying FL-MXene inks of various concentrations, resistance measurements were conducted multiple times at different locations on stripes measuring 7 mm in width and 10 mm in length, and the average values and standard deviations are reported in **Table III.2**. Additionally, a series of 9.6 mm long LIG-MXene-X stripes (X indicating concentration) was prepared by spraying FL-MXene ink of different concentrations or volumes. The stripes denoted as LIG-MXene-1, LIG-MXene-3, and LIG-MXene-5 were fabricated using ink concentrations of 1, 3, and 5 mg mL^{-1}, respectively. To evaluate the effect of ink volume at a fixed concentration of 5 mg mL^{-1}, stripes were further prepared by spraying 0.5, 1.0, and 1.5 mL of ink, and were denoted as LIG-MXene-5-0.5, LIG-MXene-5-1.0, and LIG-MXene-5-1.5, respectively. These stripes were evenly divided into five segments, coated with silver paint, and connected to four silver wires for electrical measurements.

Current-voltage (I-V) curves were recorded using an electrochemical workstation (Squidstat Plus 2444, USA) at a scan rate of 20 V s^{-1}. A multimeter was employed to measure the relationship between resistance and electrode spacing.

X-ray diffraction (XRD, Bruker D8 Advance, Germany) was used to characterize the crystalline phases.

The morphology and structure of samples were observed using scanning electron microscopy (SEM, ZEISS Sigma 360, Germany), and transmission electron microscopy (TEM, JEOL JEM-2100F, Japan) was used at an accelerating voltage of 200 kV to characterize FL-MXene samples, which were prepared by dropping a few droplets of the dispersion onto copper grids and drying overnight in air.

Dynamic contact angles of different substrates were measured using a dynamic contact angle analyzer (SDC 350KS, China).

III.3.6. Electrochemical Characterization

Electrochemical measurements, including cyclic voltammetry (CV), galvanostatic charge-discharge (GCD), and electrochemical impedance spectroscopy (EIS), were conducted on symmetric MXene micro-supercapacitors using an electrochemical workstation (Squidstat Plus 2444, USA). CV tests were performed at scan rates ranging from 10 to 500 mV s^{-1}. GCD measurements were conducted at current densities from 0.25 to 10.0 mA cm^{-2}, and EIS was measured within a frequency range from 100 mHz to 100 kHz.

The areal capacitance ($C_{Device,A}$) of symmetric MXene micro-supercapacitors was calculated from GCD curves using Eq. 3.1 (units: mF cm^{-2}) [37]:

$$C_{Device,A} = \frac{I \times \Delta t}{A_{Device} \times \Delta V_{Device}} \qquad \text{Eq.3.1}$$

Where Δt is the discharge duration (s), A_{Device} is the total electrochemically active area of the interdigitated electrodes (cm^2), and ΔV_{Device} is the operating voltage window (V).

The areal energy density (EA) of symmetric MXene micro-supercapacitors was calculated using Eq. 3.2 (units: μWh cm^{-2}) [37]:

$$E_A = \frac{C_A \times V^2}{2 \times 3600} \qquad \text{Eq.3.2}$$

where V is the applied voltage.

The areal power density (PA) of symmetric MXene micro-supercapacitors was calculated using Eq.3.3 (units: μW cm^{-2}) [37]:

$$P_A = \frac{E_A \times 3600}{t} \qquad \text{Eq.3.3}$$

where t is the discharge time.

III.4. Results and Discussion

III.4.1. Fabrication of Flexible Symmetric MXene-Based Micro-Supercapacitors

Figure III.1 illustrates the fabrication process of the flexible symmetric MXene-based micro-supercapacitor (MSC). Initially, an interdigitated laser-induced graphene (LIG) electrode was patterned on a polyimide (PI) substrate using CO_2 laser irradiation with a mask. Subsequently, highly conductive few-layer $Ti_3C_2T_x$ nanosheets (FL-MXene) were uniformly deposited onto the LIG surface via mask-assisted spray coating. The MXene loading on the hybrid electrodes was precisely controlled by adjusting the concentration of the FL-MXene ink. Finally, a quasi-solid-state symmetric MSC was assembled using a

polyvinyl alcohol (PVA)-based gel electrolyte, and the resulting devices were denoted as LIG-MXene-X MSCs, where X indicates the ink concentration in mg mL^{-1}.

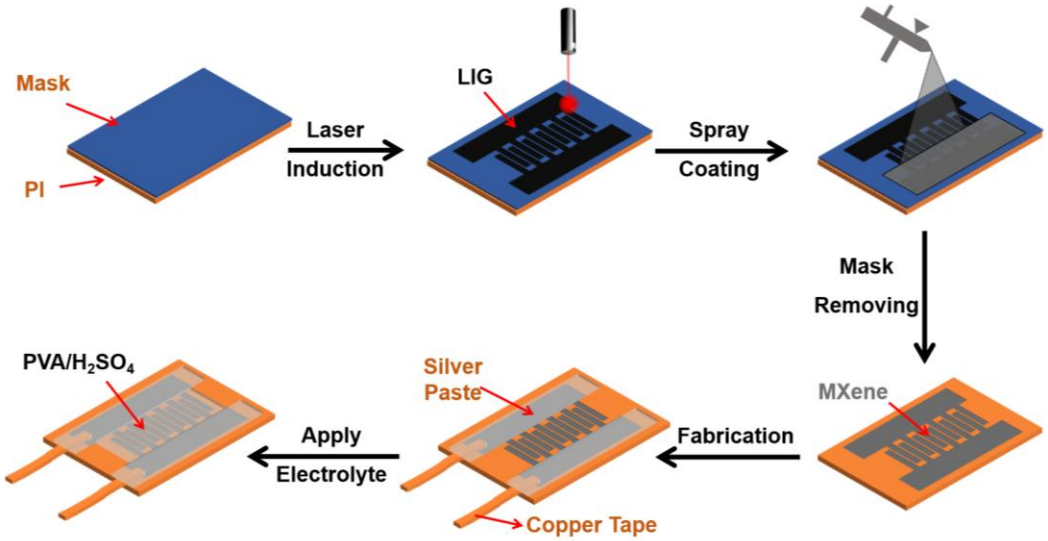

Figure III.1. Schematic illustration of the fabrication process of the flexible symmetric MXene-based micro-supercapacitor (MSC), including laser patterning of interdigitated LIG electrodes and subsequent spray deposition of FL-MXene nanosheets.

The detailed synthesis procedure of FL-MXene and the device assembly steps are described in the Experimental Section. Notably, compared to previously reported methods using direct laser cutting of MXene films to fabricate MSCs [38], the process adopted in this study—laser patterning, followed by spray deposition—effectively prevents edge oxidation of MXene nanosheets under high laser-induced temperatures, thereby enhancing the electrochemical stability of the device.

To determine the optimal laser conditions, five groups of LIG samples were fabricated and their sheet resistances were measured (**Table III.1**). For each group, three LIG strips with dimensions of 5 mm × 15 mm were tested, and the average value with standard deviation was reported. As shown in **Figure III.2a**, the L-2.1-8% sample exhibited a

relatively high resistance (11.99 Ω sq^{-1}) with large deviation, indicating insufficient graphitization. In contrast, the L-3.0-8% sample showed the lowest average sheet resistance (~5.12 Ω sq^{-1}) and better uniformity, suggesting superior conductivity and reproducibility. However, the L-3.3-8% sample featured structural damage, due to excessive laser power. Thus, a laser power of 3.0 W and a scan speed of 8% were identified as the optimal parameters, and the L-3.0-8% sample was selected for subsequent experiments.

Figure III.2b displays the X-ray diffraction (XRD) pattern of the L-3.0-8% sample (10°–80°). A prominent peak near 26.2° corresponds to the (002) plane of graphitic carbon (JCPDS No. 26-1079), indicating a well-graphitized structure. A broad peak between 12° and 22° reflects the presence of amorphous carbon domains. Additionally, a weaker diffraction peak at approximately 44.5° can be attributed to the (100) plane of graphite, suggesting an in-plane ordering of sp^2-hybridized carbon atoms [39].

Table III.1. Summary of the laser parameters used for the five fabricated samples, including the sample name, laser power, and scan speed.

Sample Name	Power (W)	Scan Speed (%)
L-2.1-8%	2.1	8
L-2.4-8%	2.4	8
L-2.7-8%	2.7	8
L-3.0-8%	3.0	8
L-3.3-8%	3.3	8

Note: The scan speed (%) refers to the percentage of the rated scan speed of the instrument. A scan speed of 8% corresponds to approximately 107.3 mm s^{-1}.

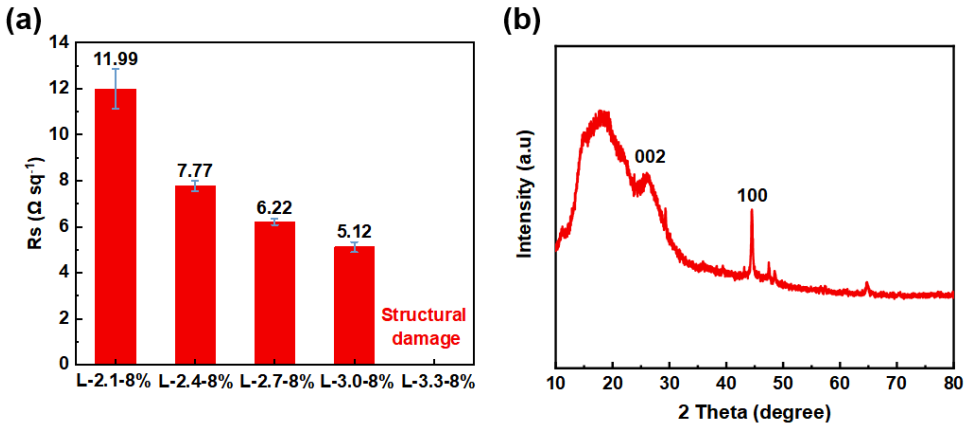

Figure III.2. (**a**) Average sheet resistance (R_s) of LIG samples fabricated under various laser conditions. Each bar represents the mean value of three independent measurements (strip size: 5 mm × 15 mm), with error bars indicating standard deviations. (**b**) X-ray diffraction (XRD) pattern of the optimized L-3.0-8% sample, showing characteristic peaks corresponding to graphitic carbon.

III.4.2. Morphological and Structural Characterization

Figure III.3 presents the surface morphology of Ti_3AlC_2 MAX phase precursor and the delaminated $Ti_3C_2T_x$ multilayer (D-MXene), captured by scanning electron microscopy (SEM). Notably, the layered morphology observed in **Figure III.3b** confirms the successful removal of Al atoms from the MAX phase and the formation of stacked D-MXene structures.

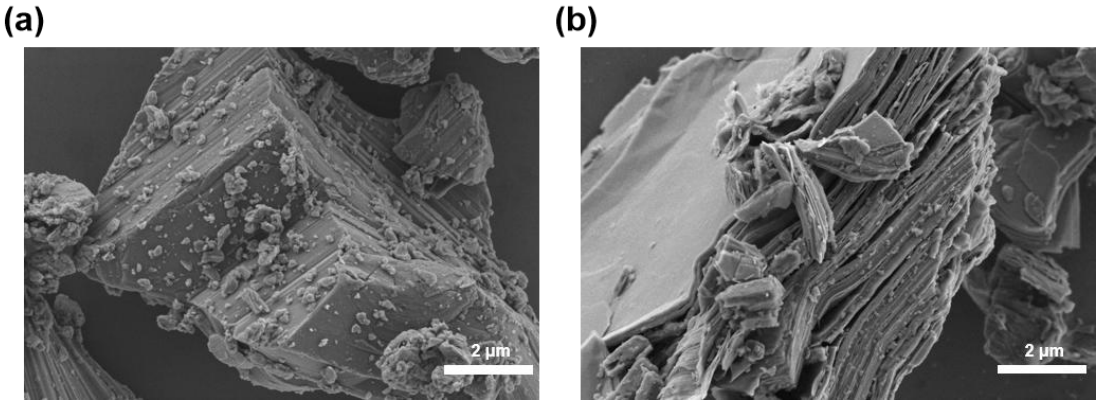

Figure III.3. SEM images of (**a**) Ti_3AlC_2 MAX phase precursor and (**b**) delaminated multilayer $Ti_3C_2T_x$ (D-MXene).

Subsequent ultrasonic treatment further exfoliated D-MXene into few-layer $Ti_3C_2T_x$ nanosheets (FL-MXene). When dispersed in deionized water, FL-MXene forms a stable colloidal solution, referred to as FL-MXene ink. As shown in **Figure III.4a**, the ink exhibits a pronounced Tyndall effect, indicative of well-dispersed nanoscale particles. **Figure III.4b** displays a transmission electron microscopy (TEM) image of the FL-MXene nanosheets, confirming their ultrathin and few-layer structure. **Figure III.4c** presents a high-resolution transmission electron microscopy (HRTEM) image of the FL-MXene nanosheets, showing distinct lattice fringes with an interplanar spacing of approximately 0.25 nm. The inset selected area electron diffraction (SAED) pattern reveals multiple concentric bright rings, confirming the polycrystalline nature of the nanosheets. This contrasts with the typical hexagonal spot pattern seen in single-layer MXene, and is likely due to the restacking or partial overlap of nanosheets during processing [40]. **Figure III.4d** compares the X-ray diffraction (XRD) patterns of Ti_3AlC_2, D-MXene, and FL-MXene powders. After etching, the (002) peak of D-MXene shifts from 9.5° to 6.8° and broadens significantly, while other peaks disappear, indicating the successful synthesis of $Ti_3C_2T_x$. Notably, the (002) peak of FL-MXene further shifts to ~6.5°, suggesting increased interlayer spacing due to effective exfoliation [41][43].

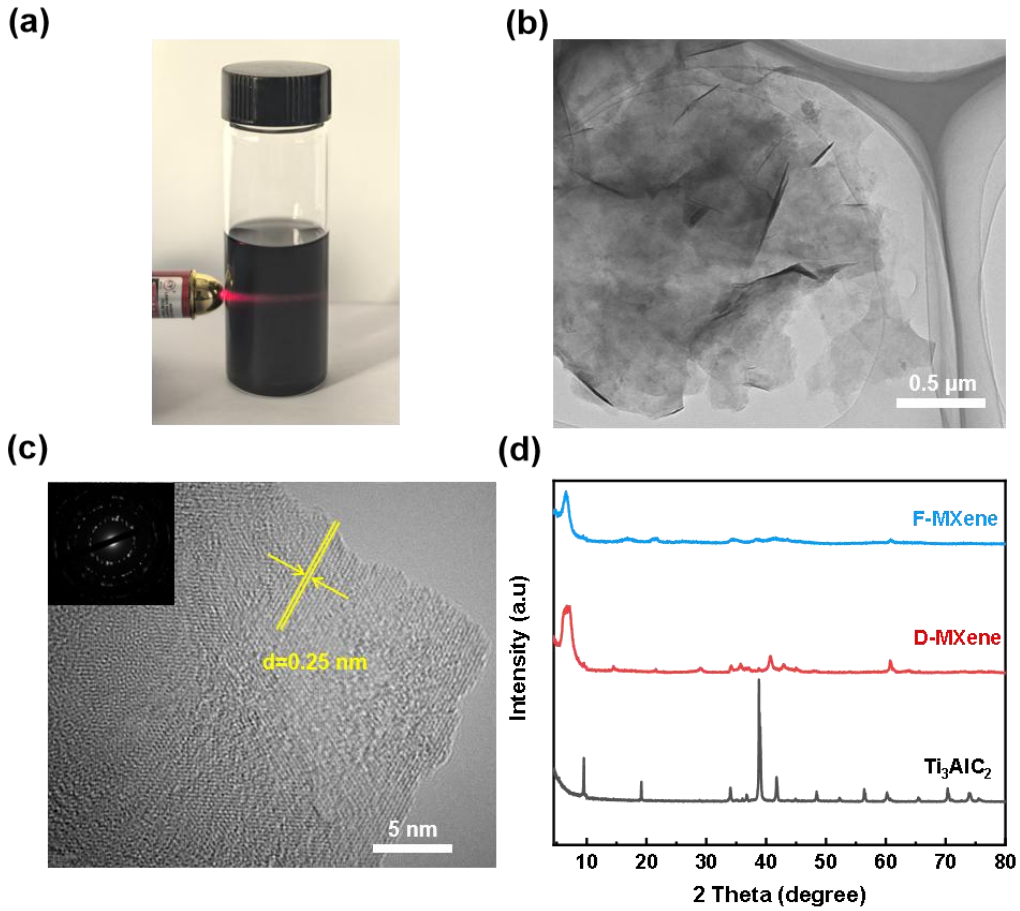

Figure III.4. (**a**) Optical image of FL-MXene ink showing a clear Tyndall effect, indicating good dispersion stability. (**b**) TEM image of few-layer FL-MXene nanosheets, confirming their ultrathin structure. (**c**) High-resolution TEM (HRTEM) image of FL-MXene displaying lattice fringes with an interplanar spacing of ~0.25 nm, the inset shows the selected area electron diffraction (SAED) pattern with multiple concentric rings, indicating a polycrystalline structure. (**d**) XRD patterns of Ti_3AlC_2, D-MXene, and FL-MXene powders. Notably, the (002) peak shift and broadening indicate successful etching and further exfoliation after ultrasonic treatment.

III.4.3. Patterning and Electrode Configuration

Laser-induced patterning controlled via computer assistance enables precise processing of polyimide (PI) substrates under ambient conditions. When combined with mask-assisted spray coating, this technique provides a high degree of flexibility in designing microsupercapacitor (MSC) arrays of various sizes and shapes, such as the letters "MXene," a paperclip shape, concentric circles, and other complex geometries (**Figure III.5a**). As shown in **Figure III.5b**, an interdigitated MSC pattern was designed and etched onto the PI substrate via laser ablation, generating laser-induced graphene (LIG) that functions as both the active electrode and current collector. The interdigitated structure minimizes short-circuit risk and facilitates miniaturization and integration, addressing energy storage needs in portable electronics. **Figure III.5c** depicts an optical image of a single interdigitated electrode (comprising 12 microelectrodes) fabricated according to the design, followed by mask-assisted deposition of MXene nanosheets. The magnified view on the right clearly depicts microelectrode structures with a finger width of ~0.6 mm, length of ~6 mm, and spacing of ~0.3 mm. The SEM cross-section of the LIG-MXene-5 electrode (**Figure III.5d**) reveals a thickness of approximately 41.3 μm.

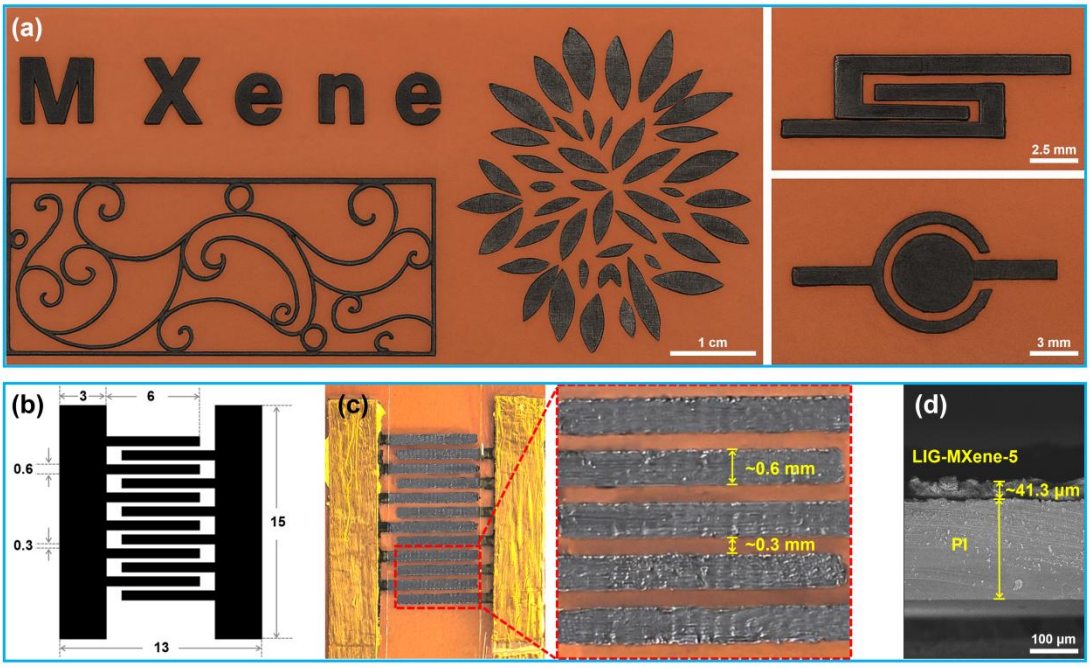

Figure III.5. (**a**) Optical images of various finely patterned designs achieved by depositing MXene nanosheets. (**b**) Top-view schematic of an interdigitated MSC layout designed using computer-aided software (dimensions in mm). (**c**) Optical image of an LIG-MXene electrode with deposited MXene nanosheets; the right panel shows a magnified view. (**d**) Cross-sectional SEM image of an LIG-MXene-5 electrode adhered to the PI substrate.

In the field of printed electronics, the uniformity and smoothness of the printed patterns are critically important [44]. The mask-assisted spray-coating technique employed in this study offers high reproducibility and patterning precision, enabling the formation of well-defined, smooth, and uniformly distributed MXene patterns on the substrate surface, which is beneficial for the investigation of their electrical properties. Substrate selection also plays a vital role—its wettability and ink drying behavior directly influence deposition quality [22]. To evaluate the advantages of the LIG substrate, FL-MXene ink was sprayed on both LIG and PI substrates, yielding LIG-MXene and PI-MXene electrodes, respectively. Optical images in **Figures III.6a** and **III.6b** show that

LIG-MXene electrodes exhibit clearer, more defined microelectrode structures than those on PI, without flaking. Due to hydrogen bonding, MXene nanosheets exhibit compact stacking and adhere firmly to the 3D porous LIG structure without polymer binders. In contrast, the inert, smooth PI surface interacts weakly with MXene, leading to delamination under mechanical stress. Contact angle measurements (**Figures III.6c** and **III.6d**) confirmed that water droplets rapidly infiltrated the LIG surface within 5 seconds, while maintaining a 77° contact angle on PI even after 60 seconds, indicating superior wettability of LIG. The excellent wettability of the LIG substrate facilitates the rapid deposition of MXene during the spray-coating process using a heat gun, leading to the formation of a uniform and conductive network, which in turn enhances the electrochemical performance of the MSCs.

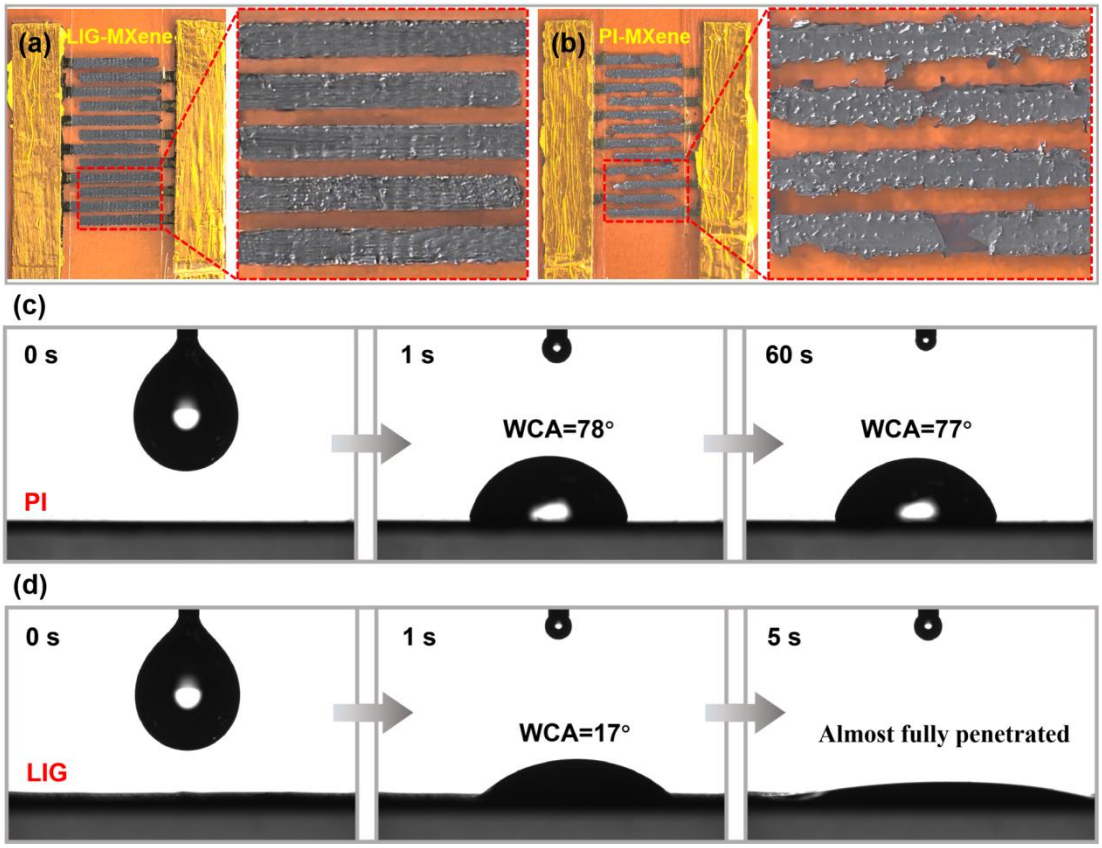

Figure III.6. (**a**) Optical image of an LIG-MXene electrode coated with MXene nanosheets; the right panel is a magnified view. (**b**) Optical image of a PI-MXene electrode; right panel shows a magnified view. (**c**) and (**d**) Comparison of surface wettability on PI and LIG substrates.

To optimize the performance of MXene-based MSCs, we evaluated various FL-MXene ink formulations. The sheet resistance (R_s) of LIG substrates sprayed with different MXene concentrations was measured and summarized in **Table III.2**. Each sample strip (7 mm wide, 10 mm long) was tested, and the average R_s values with standard deviations are presented in **Figure III.7a**. With increasing MXene ink concentration, R_s decreased significantly—from 5.12 Ω sq^{-1} for pure LIG to 1.90 Ω sq^{-1} for LIG-MXene-5, demonstrating excellent conductivity of the synthesized MXene nanosheets.

Table III.2 Summary of FL-MXene ink concentrations and corresponding sheet resistance (Rs) on LIG substrates.

Sample Name	**MXene Ink Concentration (mg mL^{-1})**	**Rs (Ω sq^{-1})**
LIG	0	5.12
LIG-MXene-1	1	5.05
LIG-MXene-3	3	3.53
LIG-MXene-5	5	1.90

Figure III.7b displays I-V curves of LIG-MXene-X strips (1, 3, and 5 mg mL^{-1}), showing clear ohmic behavior. Moreover, the resistance-length relationship was linear for all samples (**Figure III.7c**), with observed y-intercepts likely attributed to contact resistance. The unit-length resistances were 26.50, 17.57, and 8.68 Ω mm^{-1} for

concentrations of 1, 3, and 5 mg mL^{-1}, respectively. To examine the effect of spraying volume, LIG-MXene-5 strips were fabricated using 0.5, 1.0, and 1.5 mL ink volumes and labeled LIG-MXene-5-0.5, LIG-MXene-5-1.0, and LIG-MXene-5-1.5 strips, respectively. Resistance-length curves (**Figure III.7d**) revealed that higher spray volumes yielded lower unit-length resistances, decreasing from 13.94 Ω mm^{-1} (0.5 mL) to 5.28 Ω mm^{-1} (1.5 mL). These results demonstrate that the combination of laser patterning and mask-assisted MXene deposition enables controlled fabrication of electrodes with tunable electrical properties on flexible substrates, offering an efficient and scalable approach for MSC design.

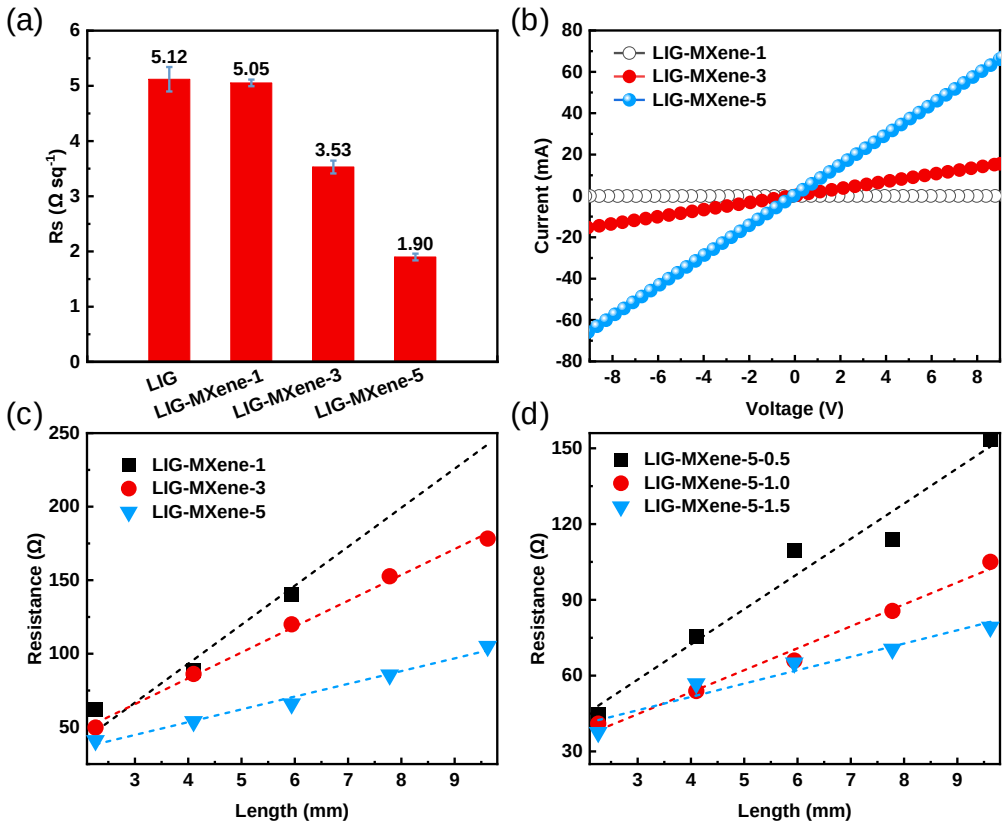

Figure III.7. (**a**) Sheet resistance (R_S) of LIG substrates sprayed with MXene inks of varying concentrations. Each bar represents the average of multiple samples under identical conditions; error bars show standard deviations. (**b**) I-V curves of LIG-MXene-

X strips sprayed using different ink concentrations. (**c**) Relationship between resistance and strip length; linearity observed in all samples. (**d**) Resistance *vs.* length curves for LIG-MXene-5-0.5, LIG-MXene-5-1.0, and LIG-MXene-5-1.5 strips.

III.4.4. Electrochemical Performance

To verify the feasibility of integrating laser processing with mask-assisted spray-coating for microscale energy storage devices, a two-electrode configuration was employed using PVA/H_2SO_4 gel electrolyte to investigate the electrochemical behavior of MXene-based micro-supercapacitors (MSCs). Devices fabricated using varying concentrations of FL-MXene ink were studied, including LIG MSC, LIG-MXene-1 MSC, LIG-MXene-3 MSC, and LIG-MXene-5 MSC. As illustrated in **Figure III.8a**, the cyclic voltammetry (CV) curves at 100 mV s^{-1} show that LIG-MXene-5 MSC exhibits the largest integrated CV area, indicating superior areal capacitance compared to other MSCs prepared using lower ink concentrations. Furthermore, the nearly rectangular shape of the CV curve suggests the formation of electrochemical double layers between MXene sheets, enabling rapid ion intercalation/deintercalation.

The scan rate-dependent CV curves of these devices are presented in **Figure III.9**, recorded over a range of 10–500 mV s^{-1}. As expected, the current response increases with scan rate. Notably, the CV response of the bare LIG substrate is negligible, indicating its minimal contribution to the overall capacitance of LIG-MXene-X MSCs. Even at a high scan rate of 500 mV s^{-1}, the devices maintain capacitive behavior, attributed to the interdigitated electrode design, which facilitates rapid ion transport in the gel electrolyte. Unlike traditional sandwich configurations, where ionic mobility is hindered by

directional limitations of 2D nanosheets and separators, this architecture promotes efficient charge transport and enhanced power density [38].

Figure III.8b displays the galvanostatic charge–discharge (GCD) profiles of LIG-MXene-X MSCs and LIG MSC recorded within a voltage window of 0–0.6 V at a current density of 0.2 mA cm^{-2}. The discharge duration increases with higher FL-MXene ink concentrations, with LIG-MXene-5 MSC featuring the longest discharge time. The minimal IR drop observed at the beginning of discharge further highlights the excellent capacitive behavior and high conductivity of the electrodes. To further explore rate-dependent behavior, GCD curves at various current densities (0.2–4.0 mA cm^{-2}) are displayed in **Figure III.10**. The negligible electrochemical response of the LIG MSC confirms its minimal electrochemical contribution, consistent with CV observations (**Figure III.9**). As microscale energy storage devices rely more on areal metrics than volumetric or gravimetric ones, as reported previously [45], areal capacitance remains the key performance parameter in this context. Based on these GCD curves, the areal capacitance values of all devices were calculated using Equation (3.1) and summarized in **Figure III.8c**. The results clearly indicate that the capacitance performance of LIG-MXene-X MSCs improves with increasing FL-MXene concentration. Specifically, LIG-MXene-5 MSC delivered the highest areal capacitance of 43.80 mF cm^{-2} at 0.2 mA cm^{-2}, while LIG MSC recorded a negligible capacitance of only 0.67 mF cm^{-2} under the same conditions (see **Table III.3** for details).

Electrochemical impedance spectroscopy (EIS) was used to further probe the charge transfer and ion transport behavior, as shown in **Figure III.8d**. The Nyquist plots feature semicircles in the high-frequency region and linear tails at low frequencies,

corresponding to charge transfer resistance (R_{ct}) and Warburg-type ion diffusion, respectively. The solution resistance (R_s) values for LIG-MXene-1 MSC, LIG-MXene-3 MSC, and LIG-MXene-5 MSC were 19.7, 20.0, and 18.2 Ω, respectively. Notably, R_{ct} decreased significantly from 37.2 Ω in LIG-MXene-3 to 15.8 Ω in LIG-MXene-5, indicating that increased MXene loading facilitates interfacial charge transfer and enhances overall electrochemical performance. These findings suggest that the electrochemical behavior of MXene-based MSCs is primarily diffusion-controlled and can be tuned through electrode composition optimization. Thus, a concentration of 5 mg mL^{-1} was identified as optimal and used for further studies and benchmarking against other reported MSCs.

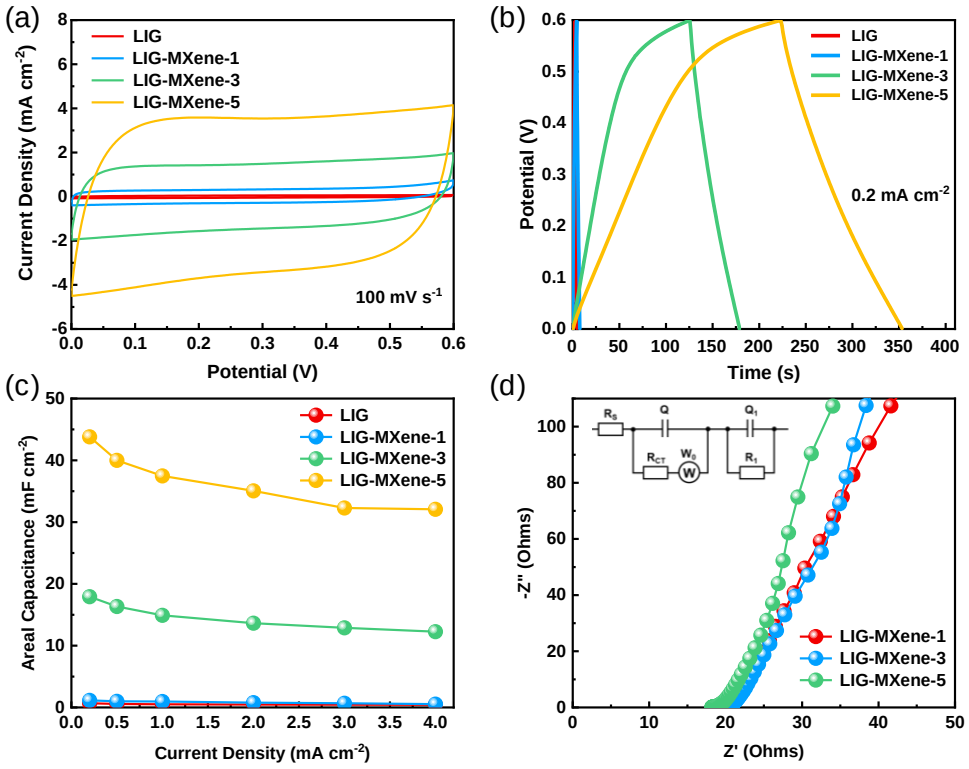

Figure III.8. Electrochemical performance of LIG-MXene-X MSCs and LIG MSC. (**a**) CV curves of LIG-MXene-X MSCs and LIG MSC at a scan rate of 100 mV s^{-1}. (**b**) GCD curves at a current density of 0.2 mA cm^{-2}. (**c**) Areal capacitance values as a function of

current density ranging from 0.2 to 4.0 mA cm^{-2}. (**d**) Electrochemical impedance spectra (EIS) of LIG-MXene-X MSCs measured from 100 mHz to 100 kHz.

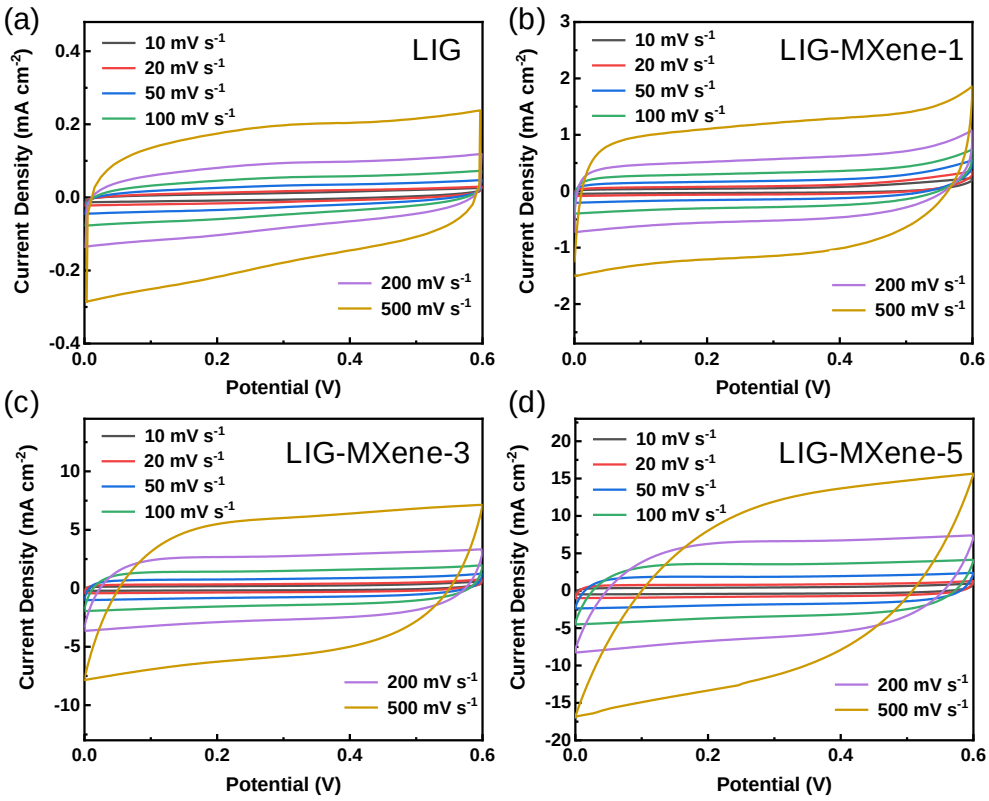

Figure III.9. CV curves of (**a**) LIG MSC, (**b**) LIG-MXene-1 MSC, (**c**) LIG-MXene-3 MSC, and (**d**) LIG-MXene-5 MSC measured at scan rates ranging from 10 to 500 mV s^{-1} within a voltage window of 0–0.6 V.

The areal energy density and power density of LIG-MXene-X MSCs and LIG MSC were calculated using Equations (3.2) and (3.3) and the results are summarized in **Table III.3**. As shown in **Figure III.11**, the Ragone plot highlights the performance of LIG-MXene-5 MSC, which delivers a maximum areal energy density of 2.103 µWh cm^{-2} at a power density of 58.80 µW cm^{-2}. Even at a high power density of 1037.86 µW cm^{-2}, it maintains an energy density of 1.200 µWh cm^{-2}. Compared with other printed MSCs based on graphene or sprayed graphene/MXene hybrids, LIG-MXene-5 MSC exhibits an

order of magnitude improvement in energy density. Detailed performance comparisons are tabulated in **Table III.4**.

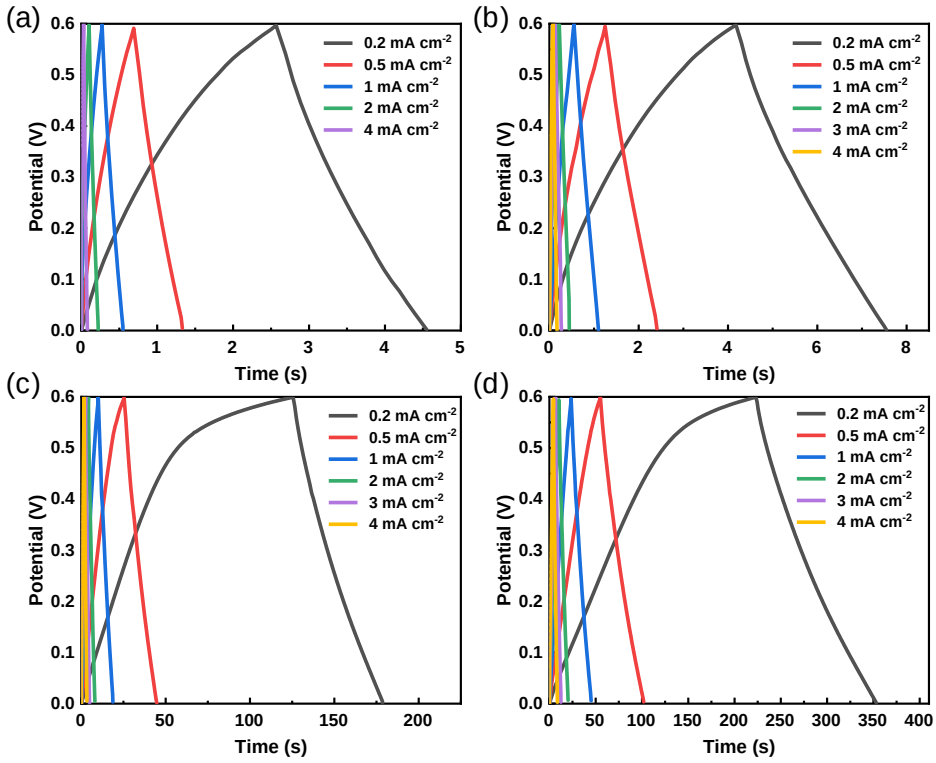

Figure III.10. GCD curves of (**a**) LIG MSC, (**b**) LIG-MXene-1 MSC, (**c**) LIG-MXene-3 MSC, and (**d**) LIG-MXene-5 MSC recorded at current densities from 0.2 to 4.0 mA cm^{-2} within 0–0.6 V.

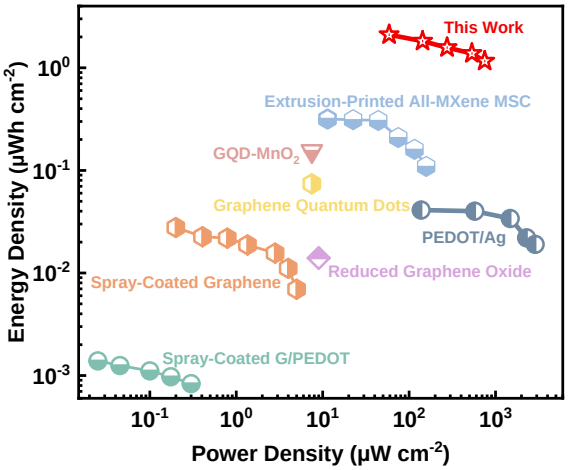

Figure III.11. Ragone plot comparing the areal energy and power densities of LIG-MXene-5 MSC with those of previously reported MSC systems. Detailed reference data are provided in **Tables III.3** and **III.4**.

Table III.3. Summary of Areala capacitance, energy density, and power density of LIG-MXene-X MSCs and LIG MSC under various current densities.

Sample	Electrolyte	Test Condition	Areal Capacitance (mF cm^{-2})	Energy Density (μWh cm^{-2})	Power Density (μW cm^{-2})
LIG MSC	PVA/H_2SO_4	0.2 mA cm^{-2}	0.67	0.027	60.0
		0.5 mA cm^{-2}	0.56	0.020	125.35
		1 mA cm^{-2}	0.51	0.016	236.05
		2 mA cm^{-2}	0.46	0.010	389.87
		4 mA cm^{-2}	0.42	0.003	471.56
LIG-MXene-1 MSC	PVA/H_2SO_4	0.2 mA cm^{-2}	1.14	0.050	56.22
		0.5 mA cm^{-2}	0.99	0.037	129.14
		1 mA cm^{-2}	0.96	0.023	206.55
		2 mA cm^{-2}	0.78	0.017	396.34
		3 mA cm^{-2}	0.68	0.008	437.01
		4 mA cm^{-2}	0.53	0.002	360.28
LIG-MXene-3 MSC	PVA/H_2SO_4	0.2 mA cm^{-2}	17.92	0.840	58.08
		0.5 mA cm^{-2}	16.34	0.682	136.98
		1 mA cm^{-2}	14.91	0.616	272.77
		2 mA cm^{-2}	13.64	0.554	541.09
		3 mA cm^{-2}	12.89	0.469	767.64
		4 mA cm^{-2}	12.27	0.430	1004.58
LIG-MXene-5 MSC	PVA/H_2SO_4	0.2 mA cm^{-2}	43.80	2.103	58.80
		0.5 mA cm^{-2}	40.00	1.820	143.11
		1 mA cm^{-2}	37.47	1.576	275.18
		2 mA cm^{-2}	35.06	1.382	532.72
		3 mA cm^{-2}	32.29	1.163	749.95
		4 mA cm^{-2}	32.07	1.200	1037.86

Note: The capacitance reported for the MXene-based MSC refers to the total device capacitance, rather than the capacitance of individual electrodes.

Table III.4. Comparative analysis of areal energy and power densities among reported printed MSCs.

Electrode Material	Energy Density ($\mu Wh\ cm^{-2}$)	Power Density ($\mu W\ cm^{-2}$)	Reference
Reduced Graphene Oxide	9.0	0.014	[46]
Graphene Quantum Dots	7.5	0.074	[47]
Graphene Quantum Dots/MnO_2	7.5	0.154	[47]
PEDOT/Ag	138	0.041	[48]
	575	0.04	
	1480	0.034	
	2290	0.022	
	2880	0.019	
Inkjet-Printed Graphene	0.025	0.00139	[49]
	0.045	0.00125	
	0.1	0.00111	
	0.175	0.000972	
	0.3	0.000833	
Spray-Coated Graphene	0.2	0.02778	[50]
	0.40625	0.02257	
	0.7875	0.02187	
	1.35	0.01875	
	2.8125	0.01563	
	4.0	0.01111	
	5.0	0.00694	
Extrusion-Printed All-MXene MSC	11.4	0.3166	[22]
	22.5	0.312	
	44.1	0.3065	
	75.1	0.2086	
	115.4	0.1603	
	157.7	0.1094	

III.4.5. Application Demonstration of MXene-Based MSCs

To meet practical application requirements, micro-supercapacitors (MSCs) are often configured in series or parallel to achieve desired voltage outputs. Benefiting from the programmable laser processing on PI substrates, arbitrary electrode patterns can be realized, significantly simplifying device integration. In this study, three tandem configurations were constructed: A 4S configuration, consisting of four MSCs connected in series, capable of storing charge reversibly within a voltage window of 2.4 V; A 2P2S configuration, which includes two MSCs in series connected in parallel with another identical 2S unit, operating at 1.2 V with doubled current output; A 4P configuration, with four MSCs connected in parallel, providing 0.6 V and tripled current output. **Figure III.12a** presents an optical image of the spray-coated 2P2S device fabricated on a PI substrate. **Figures III.12b and c** further demonstrate the excellent mechanical flexibility of the tandem structures, highlighting their suitability for flexible and wearable applications. **Figure III.12d** shows schematic illustrations of the 4S, 4P, and 2P2S configurations generated using computer-aided design, underscoring the versatility of this method to construct customized MSC networks tailored for varying energy and power demands.

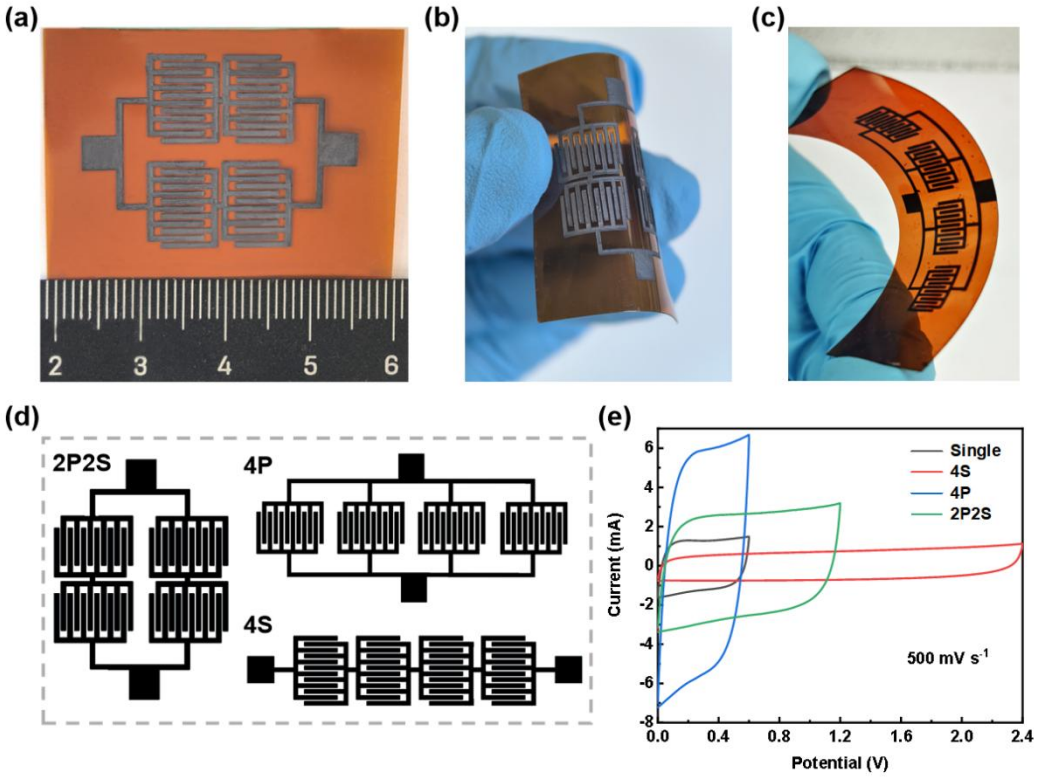

Figure III.12. Optical and schematic illustrations of MXene-based tandem MSCs. (**a**) Optical image of a 2P2S tandem device (two MSCs in parallel and two in series) fabricated on a PI substrate, the bottom ruler is marked in millimeters (mm) to indicate the overall size. (**b–c**) Demonstration of device flexibility. (**d**) Schematic diagrams of three interconnection configurations: 2P2S, 4P, and 4S. (**e**) Representative CV curves of the as-assembled tandem devices, indicating adjustable voltage and capacitance through series and parallel combinations.

To further explore the electrochemical performance of these interconnected devices, CV and GCD characterizations were conducted using a two-electrode setup with PVA/H_2SO_4 gel electrolyte. **Figures III.13a–c** display the CV curves of the 2P2S, 4S, and 4P devices over a scan rate range of 10 to 500 mV s^{-1}. In addition, **Figure III.12e** compares the CV responses of all configurations at 500 mV s^{-1}. The 4P configuration exhibited a significantly enhanced areal capacitance within the same 0–0.6 V window

due to increased active electrode area. The 4S configuration, while showing a lower current response, extended the voltage window up to 2.4 V. Meanwhile, the 2P2S device balanced increased voltage and higher capacitance, operating within a 1.2 V window. These results confirm that series connections increase the operational voltage, whereas parallel configurations enhance the total capacitance—both critical factors for practical applications. **Figure III.13d–f** further presents GCD curves of the three configurations under various current densities (0.2–4.0 mA cm^{-2}). The 4S, 2P2S, and 4P devices exhibited increasing voltage windows of 0.6 V, 1.2 V, and 2.4 V, respectively, while discharge durations were notably longer for the parallel-connected devices, verifying the capacitance enhancement. All devices displayed nearly rectangular CV profiles and symmetrical linear GCD curves with negligible IR drops, indicating excellent capacitive performance and effective charge transport. These findings demonstrate the feasibility of combining laser processing with mask-assisted spray-coating to fabricate flexible, high-performance MXene-based MSC arrays.

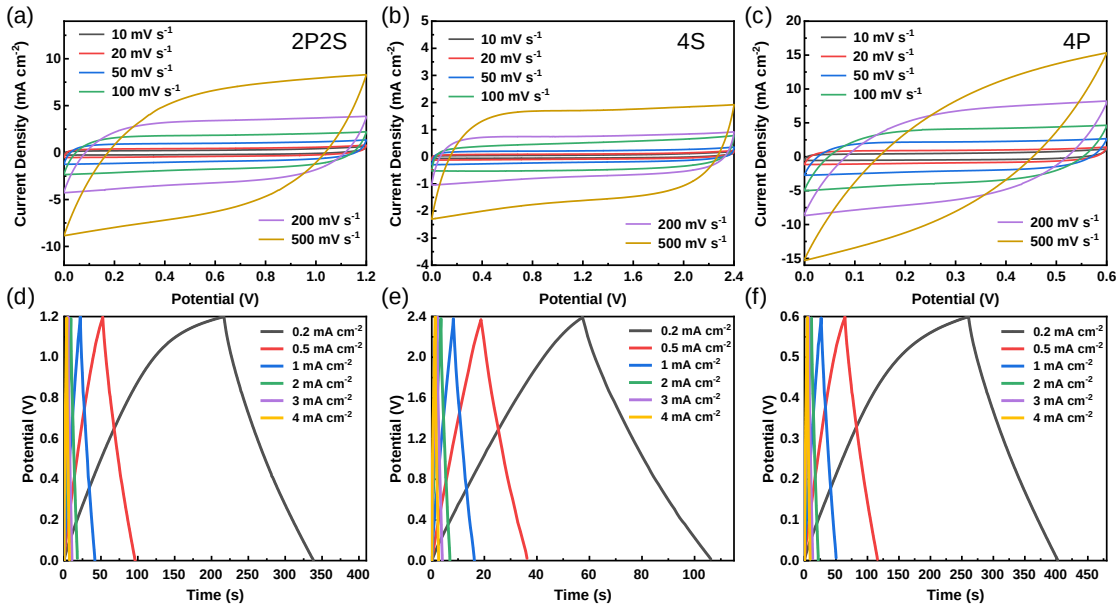

Figure III.13. Electrochemical characterization of MXene-based tandem MSCs. (**a–c**) CV curves of 2P2S, 4S, and 4P tandem configurations at various scan rates. (**d–f**) Corresponding GCD curves of each configuration measured at different current densities.

The proposed strategy was further extended to large-scale energy storage systems. As shown in **Figure III.14a**, a flexible MSC array composed of 6 cells in series and 6 in parallel (6S×6P) was fabricated, achieving a total footprint of over 133 cm^2. **Figures III.14b–d** reveal that the array can be bent, twisted, and rolled into a cylindrical shape, confirming its outstanding mechanical flexibility. To verify real-world functionality, this integrated MSC array was combined with a commercial polycrystalline silicon solar panel (energy harvester) and a red LED bulb (energy consumer) to form a self-powered energy conversion–storage–utilization system. **Figure III.14e** illustrates the system schematic, where a single-pole double-throw (SPDT) switch toggles between charging and discharging modes. Upon charging under simulated sunlight, the MSC array successfully powered the LED bulb for over 4 minutes (**Figure III.14f**), demonstrating its potential for on-demand energy storage in portable electronics.

Additionally, to demonstrate compatibility with biodegradable substrates, MXene-based MSCs were fabricated on both flat paper and corrugated paperboard, as shown in **Figure III.15a, b**. Previous studies have reported that laser-induced graphene (LIG) can be formed not only on PI films, but also on naturally degradable substrates such as paper, textiles, and cork [51]. Here, our hybrid fabrication strategy enables direct patterning of MXene-coated interdigital electrodes on paper-based substrates, where the nanoflakes permeate the porous LIG matrix to form conductive networks. This approach paves the

way for developing low-cost, flexible, and environmentally friendly energy storage devices adaptable to various substrates and application scenarios.

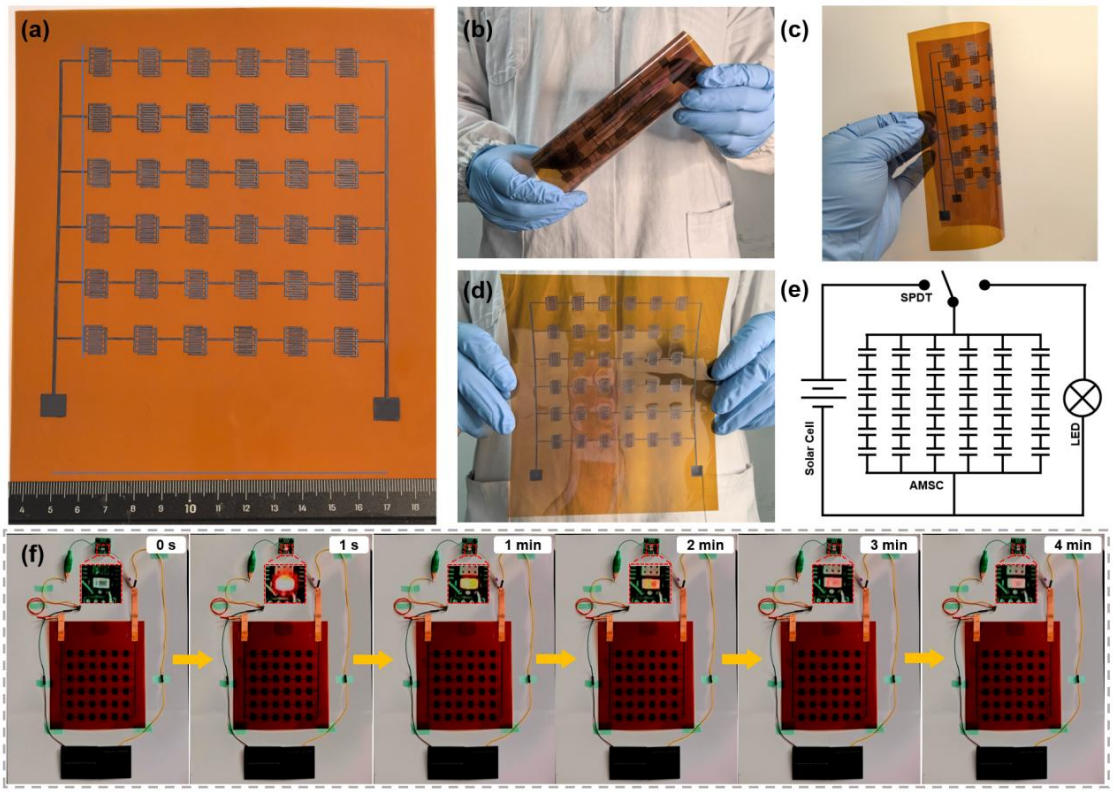

Figure III.14. Large-scale integration and practical application of MXene-based MSC arrays. (**a**–**d**) Photographs of a 6S×6P integrated MSC array on a flexible PI substrate under flat and bent states. (**e**) Schematic diagram of a self-powered system integrating solar cells, MSCs, and an LED. (**f**) Optical image of the system powering a commercial red LED after solar charging under simulated sunlight.

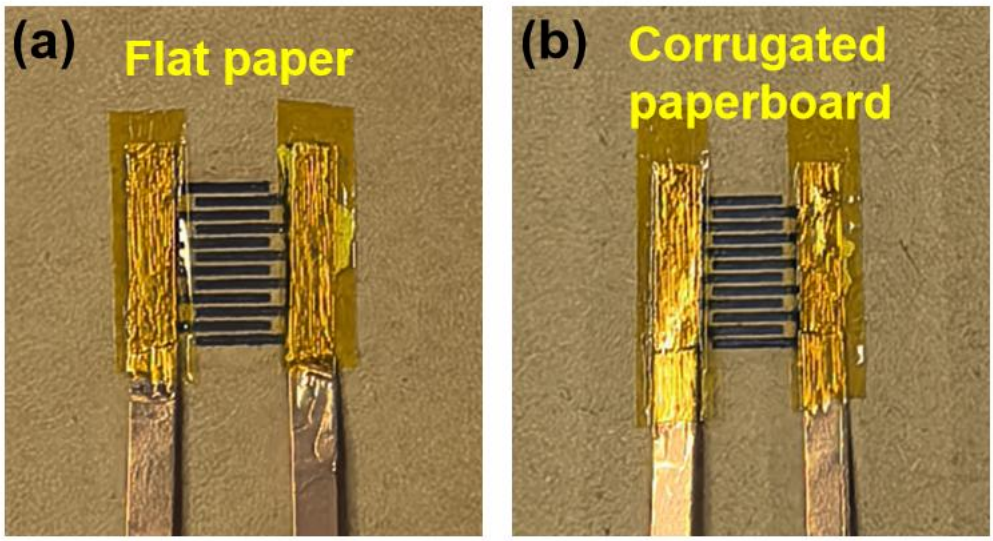

Figure III.15. Demonstration of MXene-based MSCs fabricated on biodegradable paper substrates. (**a**) Interdigitated MXene MSC on flat paper. (**b**) Interdigitated MXene MSC on corrugated paperboard.

III.5. Conclusion

In this work, a scalable, low-cost, and programmable strategy was developed for the fabrication of high-performance, flexible MXene-based micro-supercapacitors (MSCs) through the integration of laser-induced graphene (LIG) patterning and mask-assisted spray deposition of additive-free $Ti_3C_2T_x$ inks. The interdigitated LIG electrodes, formed on polyimide substrates via optimized CO_2 laser irradiation, exhibited excellent wettability, which facilitated the uniform deposition of few-layer MXene nanosheets onto the 3D porous LIG framework. This hierarchical structure significantly enhanced interfacial adhesion and charge transport, leading to hybrid electrodes with excellent conductivity and superior electrochemical performance. Notably, the MXene flakes tightly adhered to the LIG scaffold without the need for polymeric binders, benefiting from strong hydrogen bonding and the high surface area of the porous carbon network.

Systematic studies demonstrated that increasing the MXene ink concentration reduced sheet resistance and improved the areal capacitance. At a current density of 0.2 mA cm^{-2}, the optimized LIG-MXene-5 MSC exhibits a maximum areal capacitance of 43.80 mF cm^{-2} and an energy density of 2.103 μWh cm^{-2} at a corresponding power density of 58.80 μW cm^{-2}. The fabricated MSCs exhibited fast charge–discharge behavior, low internal resistance, and excellent rate capability. Importantly, modular integration in 4S, 4P, and 2P2S configurations enabled tunable voltage and current outputs, while large-area 6S×6P MSC arrays and a self-powered system with solar energy harvesting were also demonstrated. The versatility of the method was further validated by its application to biodegradable substrates, confirming its compatibility with sustainable electronics.

Overall, this study presents a robust and scalable platform for manufacturing flexible MSCs with tunable performance, offering broad potential for integration into wearable, self-powered, and environmentally benign electronic systems.

References

[1] H. Tang, W. Li, L. Pan, C. P. Cullen, Y. Liu, A. Pakdel, D. Long, J. Yang, N. McEvoy, G. S. Duesberg, V. Nicolosi, C. Zhang, Adv. Sci. 2018, 5, 1800502.

[2] C. J. Zhang, V. Nicolosi, Energy Storage Mater. 2019, 16, 102–125.

[3] T. Cheng, Y. Z. Zhang, J. P. Yi, L. Yang, J. D. Zhang, W. Y. Lai, W. Huang, J. Mater. Chem. A. 2016, 4, 13754–13763.

[4] T. Cheng, Y. Z. Zhang, J. D. Zhang, W. Y. Lai, W. Huang, J. Mater. Chem. A. 2016, 4, 10493–10499.

[5] T. Cheng, Y. Z. Zhang, W. Y. Lai, W. Huang, Adv. Mater. 2015, 27, 3349–3376.

[6] P. Zhang, F. Wang, M. Yu, X. Zhuang, X. Feng, Chem. Soc. Rev. 2018, 47, 7426–7451.

[7] N. C. Miller, H. M. Grimm, W. S. Horne, G. R. Hutchison, Nanoscale Adv. 2019, 1, 4834–4843.

[8] P. P. Zhang, F. X. Wang, S. Yang, G. Wang, M. Yu, X. L. Feng, Energy Storage Mater. 2020, 28, 160–187.

[9] C. Zhang, S. Park, S. E. O'Brien, A. S. Ascaso, M. Liang, D. Hanlon, D. Krishnan, A. Crossley, N. McEvoy, J. N. Coleman, V. Nicolosi, Nano Energy. 2017, 39, 151–161.

[10] E. B.Secor, B. Y. Ahn, T. Z. Gao, J. A. Lewis, M. C. Hersam, Adv. Mater. 2015, 27, 6683–6688.

[11] Z. S. Wu, K. Parvez, X. Feng, K. Müllen, Nat. Commun. 2013, 4, 2487.

[12] M. Beidaghi, C. L. Wang, Adv. Funct. Mater. 2012, 22, 4501–4510.

[13] S. Uzun, M. Schelling, K. Hantanasirisakul, T. S. Mathis, R. Askeland, G. Dion, Y. Gogotsi, Small. 2021, 17, 2006376.

[14] S. K. Xu, Y. Dall'Agnese, G. D. Wei, C. Zhang, Y. Gogotsi, W. Han, Nano Energy. 2018, 50, 479–488.

[15] H. B. Hu, T. Hua, J. Mater. Chem. A. 2017, 5, 19639–19648.

[16] W. J. Yang, J. Yang, J. J. Byun, F. P. Moissinac, J. Q. Xu, S. J. Haigh, M. Domingos, M. A. Bissett, R. A. W. Dryfe, S. Barg, Adv. Mater. 2019, 31, 1902725.

[17] J. Orangi, F. Hamade, V. A. Davis, M. Beidaghi, ACS Nano. 2020, 14, 640–650.

[18] M. C. Li, Q. L. Wu, R. J. Moon, M. A. Hubbe, M. J. Bortner, Adv. Mater. 2021, 33, 2006052.

[19] Y. Z. Zhang, Y. Wang, Q. Jiang, J. K. El-Demellawi, H. Kim, H. N. Alshareef, Adv. Mater. 2020, 32, 1908486.

[20] G. Hu, J. Kang, L. W. T. Ng, X. Zhu, R. C. T. Howe, C. G. Jones, M. C. Hersam, T. Hasan, Chem. Soc. Rev. 2018, 47, 3265–3300.

[21] D. Song, A. Mahajan, E. B. Secor, M. C. Hersam, L. F. Francis, C. D. Frisbie, ACS Nano. 2017, 11, 7431–7439.

[22] C. F. Zhang, L. McKeon, M. P. Kremer, S. H. Park, O. Ronan, A. Seral-Ascaso, S. Barwich, C. O. Coileain, N. McEvoy, H. C. Nerl, B. Anasori, J. N. Coleman, Y. Gogotsi, V. Nicolosi, Nat. Commun. 2019, 10, 1795–1804.

[23] M. Naguib, V. N. Mochalin, M. W. Barsoum, Y. Gogotsi, Adv. Mater. 2014, 26, 992–1005.

[24] Y. Xie, M. Naguib, V. N. Mochalin, M. W. Barsoum, Y. Gogotsi, X. Yu, K. W. Nam, X. Q. Yang, A. I. Kolesnikov, P. R. C. Kent, J. Am. Chem. Soc. 2014, 136, 6385–6394.

[25] S. Zhao, X. Meng, K. Zhu, F. Du, G. Chen, Y. Wei, Y. Gogotsi, Y. Gao, Energy Storage Mater. 2017, 8,42–48.

[26] I. J. Echols, J. Yun, H. Cao, R. M. Thakur, A. Sarmah, Z. Tan, R. Littleton, M. Radovic, M. J. Green, J. L. Lutkenhaus, Chem. Mater. 2022, 34,4884–4895.

[27] M. Vural, A. P. Francesch, J. B. Pomes, H. Jung, H. Gudapati, C. B. Hatter, B. D. Allen, B. Anasori, I. T. Ozbolat, Y. Gogotsi, M. C. Demirel, Adv. Funct. Mater. 2018, 28, 1801972.

[28] Y. Liu, E. Li , Y. Yan, Z. Lin, Q. Chen, X. Wang, L. Shan, H. Chen, T. Guo, Nano Energy. 2021, 86, 106118.

[29] C. J. Zhang, B. Anasori, A. S. Ascaso, S. H. Park, N. McEvoy, A. Shmeliov, G. S. Duesberg, J. N. Coleman, Y. Gogotsi, V. Nicolosi, Adv. Mater. 2017, 29, 1702678.

[30] X. Li, Z. Huang, C. E. Shuck, G. Liang, Y. Gogotsi, C. Zhi, Nat. Rev. Chem. 2022, 6, 389–404.

[31] M. Boota, B. Anasori, C. Voigt, M. Q. Zhao, M. W. Barsoum, Y. Gogotsi, Adv. Mater. 2016, 28, 1517–1522.

[32] D. B. Xiong, X. F. Li, Z. M. Bai, S. G. Lu, Small. 2018, 14, 1703419.

[33] E. Quain, T. S. Mathis, N. Kurra, K. Maleski, K. L. V. Aken, M. Alhabeb, H. N. Alshareef, Y. Gogotsi, Adv. Mater. Technol. 2019, 4, 1800256.

[34] J. Zheng, J. Diao, Y. Jin, A. Ding, B. Wang, L. Wu, B. Weng, J. Chen, J. Electrochem. Soc. 2018, 165, B227–B231.

[35] Y. Y. Peng, B. Akuzum, N. Kurra, M. Q. Zhao, M. Alhabeb, B. Anasori, E. C. Kumbur, H. N. Alshareef, M. D. Gerc, Y. Gogotsi, Energy Environ. Sci. 2016, 9, 2847–2854.

[36] H. Hu, T. Hua, J. Mater. Chem. A. 2017, 5, 19639–19648.

[37] L. Li, J. Zhang, Z. Peng, Y. L, C. Gao, Y. Ji, R. Ye, N. D. Kim, Q. Zhong, Y. Yang, H. Fei, G. Ruan, J. M. Tour, Adv. Mater. 2016, 28, 838–845.

[38] N. Kurra, B. Ahmed, Y. Gogotsi, H. N. Alshareef, Adv. Energy Mater. 2016, 6, 1601372.

[39] X. Shi, F. Zhou, J. Peng, R. Wu, Z. S. Wu, X. Bao, Adv. Funct. Mater. 2019, 29, 1902860.

[40] G. Zhou, M. C. Li, C. Liu, Q. Wu, C. Mei, Adv. Funct. Mater. 2022, 32, 2109593.

[41] M. Naguib, O. Mashtalir, J. Carle, V. Presser, J. Lu, L. Hultman, Y. Gogotsi, M. W. Barsoum, ACS Nano. 2012, 6, 1322–1331.

[42] Y. Dall'Agnese, P. Rozier, P. L. Taberna, Y. Gogotsi, P. Simon, J. Power Sources. 2016, 306, 510–515.

[43] Y. Y. Peng, B. Akuzum, N. Kurra, M. Q. Zhao, M. Alhabeb, B. Anasori, E. C. Kumbur, H. N. Alshareef, M. D. Gerc, Y. Gogotsi, Energy Environ. Sci. 2016, 9, 2847–2854.

[44] J. Li, F. Ye, S. Vaziri, M. Muhammed, M. C. Lemme, M. Östling, Adv. Mater. 2013, 25, 3985.

[45] M. Beidaghi, Y. Gogotsi, Energy Environ. Sci. 2014, 7, 867.

[46] J. J. Yoo, K. Balakrishnan, J. Huang, V. Meunier, B. G. Sumpter, A. Srivastava, M. Conway, A. L. M. Reddy, J. Yu, R. Vajtai, P. M. Ajayan, Nano Lett. 2011, 11, 1423–1427.

[47] W. W. Liu, Y. Q. Feng, X. B.Yan, J. T. Chen, Q. J. Xue, Adv. Funct. Mater. 2013, 23, 4111–4122.

[48] Z. Wang, J. Fang, H. Tang, Z. Pan, J. Zou, G. Wang, W. D. Wagner, X. Liu, Y. Wu, Y. Zhang, J. Power Sources. 2025, 632, 236383.

[49] S. S. Delekta, A. D. Smith, J. Li, M. Östling, Nanoscale. 2017, 9, 6998–7005.

[50] H. Li, Y. Hou, F. Wang, M. R. Lohe, X. Zhuang, L. Niu, X. Feng, Adv. Energy Mater. 2017, 7, 1601847.

[51] Y. Chyan, R. Ye, Y. Li, S. P. Singh, C. J. Arnusch, J. M. Tour, ACS Nano. 2018, 12, 2176−2183.

Chapter IV: High-Performance Flexible Micro-Supercapacitors Based on Laser-Induced Graphene Integrated with Hydrogen Vacancy-Rich CoNi Layer Double Hydroxide

IV.1. Abstract

Advancements in compact, flexible, and high-efficiency energy storage systems are vital to meet the escalating energy demands of wearable electronics, electric mobility solutions, and smart integrated platforms. Herein, we report an innovative design of an asymmetric micro-supercapacitor (AMSC), employing laser-induced graphene (LIG) electrodes loaded with CoNi layered double hydroxides enriched in hydrogen vacancies (CoNi-$LDH_{(v)}$). Utilizing a cost-effective and scalable laser-processing method alongside electrodeposition, we constructed porous, interdigitated LIG structures on polyimide substrates, subsequently functionalized with CoNi-$LDH_{(v)}$ and FeOOH to serve as the cathode and anode, respectively. The fabricated LIG-CoNi-$LDH_{(v)}$//LIG-FeOOH AMSC displayed enhanced electrochemical characteristics, including a broad voltage range (0–1.8 V) in a PVA/LiCl gel electrolyte, elevated areal capacitance (38.28 mF cm^{-2}) and enhanced volumetric capacitance (5.60 F cm^{-3}) at a current density of 0.25 mA cm^{-2}, good mechanical robustness, and long-term cycling stability with 92% retention over 10,000 cycles. Moreover, the device exhibited great compatibility with multiple cationic species (Li^+, Na^+, K^+, Ca^{2+}) in neutral electrolytes. Furthermore, the integration of the AMSC with a solar cell and commercial LED device underscores its feasibility for practical applications in flexible and self-powered electronics. This work provides a

promising avenue to improve MSC performance via defect engineering and hybrid material integration, while also contributing to the advancement of scalable and economically viable energy storage devices for widespread application.

Keywords: Flexible micro-supercapacitor; Laser-induced graphene; CoNi LDH; Hydrogen vacancies; Defect engineering; Electrodeposition; Pseudocapacitive materials.

IV.2. Introduction

In recent years, renewable energy sources, such as solar, wind and tidal energies, have attracted considerable attention due to their significant potential in mitigating energy crises, reducing environmental pollution, and combating global warming [1-4]. However, the intermittent and unstable characteristics of these energy sources limit their direct utilization, thus urgently necessitating the development of efficient energy conversion and storage technologies. Micro-batteries and supercapacitors, as essential components of electrochemical energy storage, have been extensively employed in portable electronic devices, electric vehicles, and smart grid systems [5]. Moreover, the rapid advancement of microelectronics technology has increased the demand for miniaturized energy storage devices featuring flexibility, enhanced safety, and easy integration capabilities [6-8]. Compared with micro-batteries that typically suffer from high costs, relatively slow charging/discharging rates and limited cycling lifetimes, micro-supercapacitors (MSCs) have attracted widespread attention, owing to their high power density, rapid charge-discharge capability, excellent cycling stability, and improved safety [9-11]. However, the relatively low energy density of MSCs restricts their practical application in high-energy-demand scenarios. Hence, increasing energy density, reducing device dimensions, and achieving multifunctional integration have become critical research objectives [12].

Traditional MSCs fabrication methods, including photolithography [13], inkjet printing [14-16], micro-origami techniques [17,18], and focused ion beam processing [19], allow precise control over electrode dimensions and improve electrochemical performance, but are typically hindered by their complexity and high production costs, limiting large-scale production.

Since laser-induced graphene (LIG) first introduction in 2014, it has garnered significant attention [20]. This method offers distinct advantages, including rapid processing, single-step material conversion and device patterning, low cost, and no requirement for cleanroom environments. During this process, a laser beam scans across the surface of a solid precursor, locally altering its properties to form carbon-based graphene-like materials with three-dimensional porous structures [21,22]. Additionally, the microstructure and electrochemical properties of LIG can be precisely tuned by adjusting laser parameters and precursor materials, thereby meeting diverse application requirements [23-27]. Moreover, LIG and its composite materials, such as boron-doped LIG [28] and metal oxide/LIG hybrid structures [29], have shown substantial potential in sensors, electronic devices, and energy storage applications [30]. Enhancing the energy density of MSCs primarily depends on increasing electrode capacitance or broadening the operational voltage window ($E=CV^2/2$) [31]. To overcome the limitations of conventional fabrication methods, laser processing offers an efficient and scalable route by combining laser patterning with electrodeposition techniques [32,33]. Specifically, pseudocapacitive materials, such as transition metal oxides [34], hydroxides [35], sulfides [36], and conducting polymers [37], can be electrodeposited onto LIG substrates, thereby

significantly enhancing charge storage capabilities and forming high-performance nanocomposite electrodes to address the low energy density limitation of MSCs [38].

Layered double hydroxides (LDHs) are a class of two-dimensional layered materials that have received significant attention in energy storage applications, due to their unique structure, tunable chemical composition, and excellent electrochemical properties [39]. LDHs consist of positively charged metal hydroxide layers intercalated with anionic species, exhibiting excellent redox activity. However, the practical application of LDHs in alkaline supercapacitors is limited by their intrinsically narrow potential window (<0.5 V vs. SCE), as determined by the redox behavior of the host layers, and by the onset of oxygen evolution reaction (OER) under high-pH conditions, which may lead to performance degradation [40]. Furthermore, highly alkaline electrolytes such as KOH can pose environmental and corrosion concerns in practical device configurations [41]. To enhance the electrochemical performance of LDHs, various strategies have been explored, including intercalation modification [42], surface engineering [43], hybrid assembly [44], compositional tuning [45], and defect engineering [46,47]. Notably, defect engineering—particularly through the introduction of oxygen vacancies—has been demonstrated to effectively improve electronic conductivity, reduce reaction barriers, and increase active sites [48-50]. More importantly, recent studies have highlighted the significant role of hydrogen vacancies in LDH structures. For instance, hydrogen vacancy-rich CoFe-LDH has been reported to activate oxygen species, serving as active adsorption sites for cation storage and significantly improving the charge storage capacity of supercapacitors [51,52]. Furthermore, Li et al.[53] demonstrated that deprotonated LDHs can serve as promising cathode materials in aqueous batteries, exhibiting negative adsorption energies

towards various cations and thereby demonstrating exceptional potential for multi-cation intercalation. Inspired by these findings, the current study aims to develop a high-performance asymmetric MSCs based on hydrogen vacancy-rich LDHs, exploring their enhanced capability for energy storage applications.

In this study, a high-performance asymmetric micro-supercapacitor (AMSC) based on laser-induced graphene (LIG) and hydrogen vacancy-rich layered double hydroxides (CoNi-$LDH_{(v)}$) is proposed. By integrating laser induction with the electrodeposition of pseudocapacitive materials, a flexible, ASMC was successfully fabricated. Porous interdigitated LIG electrodes were directly patterned on a polyimide (PI) substrate using CO_2 laser irradiation, enhancing conductivity and serving as a flexible scaffold for subsequent material deposition. CoNi-$LDH_{(v)}$ and FeOOH were electrodeposited onto the positive and negative interdigitated electrodes, respectively, forming the LIG-CoNi-$LDH_{(v)}$//LIG-FeOOH AMSC. This AMSC device operates over a wide voltage window (0–1.8 V) and eliminates the need for additional current collectors, binders, or separators. It exhibits enhanced energy density, power density, cycling stability, and mechanical flexibility. Notably, electrochemical evaluation revealed that the LIG-CoNi-$LDH_{(v)}$//LIG-FeOOH AMSC demonstrated excellent performance in neutral electrolytes containing various cations (Li^+, Na^+, K^+, and Ca^{2+}). In addition, the successful demonstration of powering a commercial LED using the integrated AMSC and solar cell highlights its potential for real-world application in flexible and portable energy systems. This work proposes a new strategy for developing high-performance, environmentally-friendly, and scalable micro-supercapacitors, while expanding the application potential of defect engineering in advanced energy storage materials.

IV.3. Experimental Section

IV.3.1. Fabrication of LIG-CoNi-LDH$_{(v)}$//LIG-FeOOH AMSC

IV.3.1.1. Synthesis and fabrication of laser-induced graphene (LIG)

Laser-induced graphene (LIG) was fabricated on polyimide (PI) films at room temperature and ambient air using a high-power CO_2 laser beam (Universal VLS2.30DT laser cutting platform). Laser power and scan speed were carefully selected to maintain structural integrity, while ensuring sufficient pyrolysis to convert PI substrates into conductive 3D carbon networks. After optimizing laser conditions (as detailed in Chapter III, **Table III.2**), LIG was patterned into interdigitated electrodes comprising 20 microelectrodes, each with a length of 10 mm, width of 0.6 mm, and inter-electrode gap of approximately 0.45 mm (**Figure IV.1a, b**). Colloidal silver paste (Pellco) was first applied to the common electrode areas to enhance electrical contact, followed by extension with adhesive copper tape to connect the electrodes to an electrochemical workstation. The common areas of the electrodes were covered with adhesive Kapton film to protect them from the gel electrolyte.

IV.3.1.2. Preparation of LIG-CoNi-LDH

The LIG-CoNi-LDH electrodes were prepared *via* a one-step electrochemical deposition method. The LIG on PI served as the working electrode, with Ag/AgCl as the reference electrode and platinum foil as the counter electrode. Electrodeposition was conducted in 50 mL aqueous solution containing $Ni(NO_3)_2 \cdot 6H_2O$ (58.2 mg) and $Co(NO_3)_2 \cdot 6H_2O$ (58.1 mg) between -1.1 and -0.5 V (*vs.* Ag/AgCl) at a scan rate of 20 mV s^{-1} for various cycles

(30, 40, 50, and 60 cycles). These electrodes were designated as LIG-CoNi-30, LIG-CoNi-40, LIG-CoNi-50, and LIG-CoNi-60, respectively.

IV.3.1.3. Electrochemical activation of LIG-CoNi-LDH (LIG-CoNi-$LDH_{(v)}$)

The LIG-CoNi-LDH electrodes were electrochemically activated by cyclic voltammetry (CV) scanning between 0 and 0.8 V (*vs.* Ag/AgCl) at 100 mV s^{-1} for 10 cycles in 1 M KOH solution, designated as LIG-CoNi-$LDH_{(v)}$ [53][55].

IV.3.1.4. Fabrication of LIG-FeOOH

The electrodeposition of FeOOH was performed in a three-electrode configuration with LIG as the working electrode (WE), Ag/AgCl as the reference electrode (RE), and platinum foil as the counter electrode (CE). Electrodeposition was carried out at a constant potential of -1.0 V (*vs.* Ag/AgCl) in a 50 mL aqueous solution containing $Fe(NO_3)_3 \cdot 9H_2O$ (2.02 g) for durations of 30, 60, and 90 min. According to the deposition time, the samples were designated as LIG-FeOOH-30, LIG-FeOOH-60, and LIG-FeOOH-90, respectively.

IV.3.1.5. Fabrication of flexible asymmetric micro-supercapacitor (AMSC)

A polymer gel electrolyte composed of polyvinyl alcohol (PVA) and lithium chloride (LiCl) was prepared following a previously reported method [56] and utilized for the assembly of an asymmetric micro-supercapacitor (AMSC) using LIG-CoNi-$LDH_{(v)}$ as the positive electrode and LIG-FeOOH as the negative electrode. Briefly, a mixture containing 10 mL deionized water, 2.0 g LiCl (MACKLIN), and 1.0 g PVA (MACKLIN No.1799) was stirred overnight at 80 °C until a transparent gel was obtained. To fabricate the AMSC, approximately 0.25 mL of the prepared gel electrolyte was drop-cast onto the

active area of both electrodes. The assembled device was subsequently dried overnight in a vacuum desiccator (≈120 mm Hg) to ensure intimate contact and complete solidification of the electrolyte, resulting in a flexible, integrated quasi-solid-state AMSC.

IV.3.2. Electrochemical Characterization

Electrochemical measurements—including cyclic voltammetry (CV), galvanostatic charge–discharge (GCD), and electrochemical impedance spectroscopy (EIS)—were carried out using a Squidstat Plus 2444 electrochemical workstation (USA). CV tests were conducted at scan rates ranging from 10 to 100 mV s^{-1}, while GCD profiles were obtained under current densities between 0.25 and 10.0 mA cm^{-2}. EIS analyses were performed within the frequency domain of 100 mHz to 100 kHz.

The areal ($C_{+,A}$; $C_{-,A}$) and volumetric ($C_{+,V}$; $C_{-,V}$) capacitances (mF cm^{-2} and F cm^{-3}) of the positive and negative electrodes were calculated from the GCD curves using Eqs.(4.1-4.4) [56]:

$$C_{+,A} = \frac{I \times \Delta t}{A_+ \times \Delta V_+} \qquad \text{Eq.4.1}$$

$$C_{-,A} = \frac{I \times \Delta t}{A_- \times \Delta V_-} \qquad \text{Eq.4.2}$$

$$C_{+,V} = \frac{C_{+,A}}{T_+} \qquad \text{Eq.4.3}$$

$$C_{-,V} = \frac{C_{-,A}}{T_-} \qquad \text{Eq.4.4}$$

where I is the discharge current (A), Δt is the discharge duration (s), A_+ and A_- represent the effective electrode areas (cm^2), ΔV_+ and ΔV_- denote the potential ranges (V), and T_+ and T_- are the electrode thicknesses (cm), as obtained from cross-sectional SEM images.

The areal capacitance ($C_{Device,A}$) and volumetric capacitance ($C_{Device,V}$) of the complete device were evaluated using Eqs. (4.5, 4.6) [56]:

$$C_{Device,A} = \frac{I \times \Delta t}{A_{Device} \times \Delta V_{Device}} \quad \text{Eq.4.5}$$

$$C_{Device,V} = \frac{C_{Device,A}}{T_{Total}} \quad \text{Eq.4.6}$$

where A_{Device} denotes the total electrochemically active surface area of the interdigitated electrodes (cm^2), calculated as the sum of the projected areas of all electrode fingers. and ΔV_{Device} the working voltage window (V). The total device thickness T_{Total} was also determined from SEM cross-sections (cm).

Equations (4.7) and (4.8) were employed to calculate the areal energy density (E_A) (µWh cm^{-2}) and volumetric energy density (E_V) (mWh cm^{-3}) for both individual electrodes and the MSC [56]:

$$E_A = \frac{C_A \times V^2}{2 \times 3600} \quad \text{Eq.4.7}$$

$$E_V = \frac{C_V \times V^2}{2 \times 3600} \quad \text{Eq.4.8}$$

In these equations, V is the applied potential (V).

Equations (4.9) and (4.10) were used to calculate the areal power density (P_A) (μW cm^{-2}) and volumetric power density (P_V) (mW cm^{-3}) for the electrodes and the MSC [56]:

$$P_A = \frac{E_A \times 3600}{t} \quad \text{Eq.4.9}$$

$$P_V = \frac{E_V \times 3600}{t} \quad \text{Eq.4.10}$$

Here, t represents the discharge time (s).

The areal ($Q_{+,A}$; $C_{-,A}$) and volumetric ($Q_{+,V}$; $Q_{-,V}$) capacities (mC cm^{-2} and C cm^{-3}) of the positive and negative electrodes were calculated from the GCD curves using Eqs.(4.11-4.14) [57]:

$$Q_{+,A} = \frac{I \times \Delta t}{A_+} \quad \text{Eq.4.11}$$

$$Q_{-,A} = \frac{I \times \Delta t}{A_-} \quad \text{Eq.4.12}$$

$$Q_{+,V} = \frac{Q_{+,A}}{T_+} \quad \text{Eq.4.13}$$

$$Q_{-,V} = \frac{Q_{-,A}}{T_-} \quad \text{Eq.4.14}$$

where A_+ and A_- represent the effective electrode areas (cm^2) and T_+ and T_- are the electrode thicknesses (cm), as obtained from cross-sectional SEM images.

Equations (4.15) and (4.16) were used to calculate the areal capacity ($Q_{Device,A}$) (mC cm^{-2}) and volumetric capacity ($Q_{Device,V}$) (C cm^{-3}) for the electrodes and the MSC [57]:

$$Q_{Device,A} = \frac{I \times \Delta t}{A_{Device}} \qquad \text{Eq.4.15}$$

$$Q_{Device,V} = \frac{Q_{Device,A}}{T_{Total}} \qquad \text{Eq.4.16}$$

where A_{Device} denotes the total electrochemically active surface area of the interdigitated electrodes (cm^2), The total device thickness T_{Total} was also determined from SEM cross-sections (cm).

IV.4. Results and Discussion

Figure IV.2a illustrates the synthesis of hybrid materials (LIG–CoNi-LDH$_{(v)}$, LIG–FeOOH) and their assembly into AMSC devices. Firstly, CO_2 laser induction was performed on a PI substrate to pattern LIG into interdigitated electrodes. Subsequently, pseudocapacitive materials (CoNi-LDH and FeOOH) were electrodeposited onto the LIG to form LIG–CoNi-LDH and LIG–FeOOH composites. The amount of CoNi-LDH and FeOOH in the composites can be easily controlled by adjusting deposition time or cycle numbers, denoted as LIG–CoNi-X (X indicating deposition cycles) and LIG–FeOOH-Y (Y indicating deposition time). Further electrochemical activation was conducted on electrodeposited LIG–CoNi-LDH to obtain LIG–CoNi-LDH$_{(v)}$. Detailed procedures for the synthesis of LIG and electrodeposition of CoNi-LDH and FeOOH are described in the experimental section. A gel polymer electrolyte containing polyvinyl alcohol (PVA) was applied to finalize the fabrication of AMSC devices. The laser induction process, controlled by a computer, allows patterning at room temperature in ambient air, facilitating the on-demand fabrication of AMSC with varying sizes (**Figure IV.1c**).

Figure IV.2b depicts a digital image of the finalized device after all processing steps. **Figure IV.2c** displays a cross-sectional scanning electron microscopy (SEM) image of LIG–CoNi-50$_{(v)}$ electrode, revealing CoNi-LDH$_{(v)}$ deposition onto the porous LIG framework. The average thickness of the composite increased from approximately 23.7 µm for untreated LIG to 36.1 µm for LIG–CoNi-60$_{(v)}$ (**Figure IV.3**). **Figure IV.2d–g** shows top-view SEM images of LIG and LIG–CoNi-50$_{(v)}$ electrodes. LIG formed a highly porous and conductive network structure, serving as a conductive substrate for

subsequent electrodeposition and facilitating charge transfer within the electrode (**Figure IV.2d, e**). The deposited CoNi-LDH exhibited flower-like morphology (**Figure IV.2f, g**).

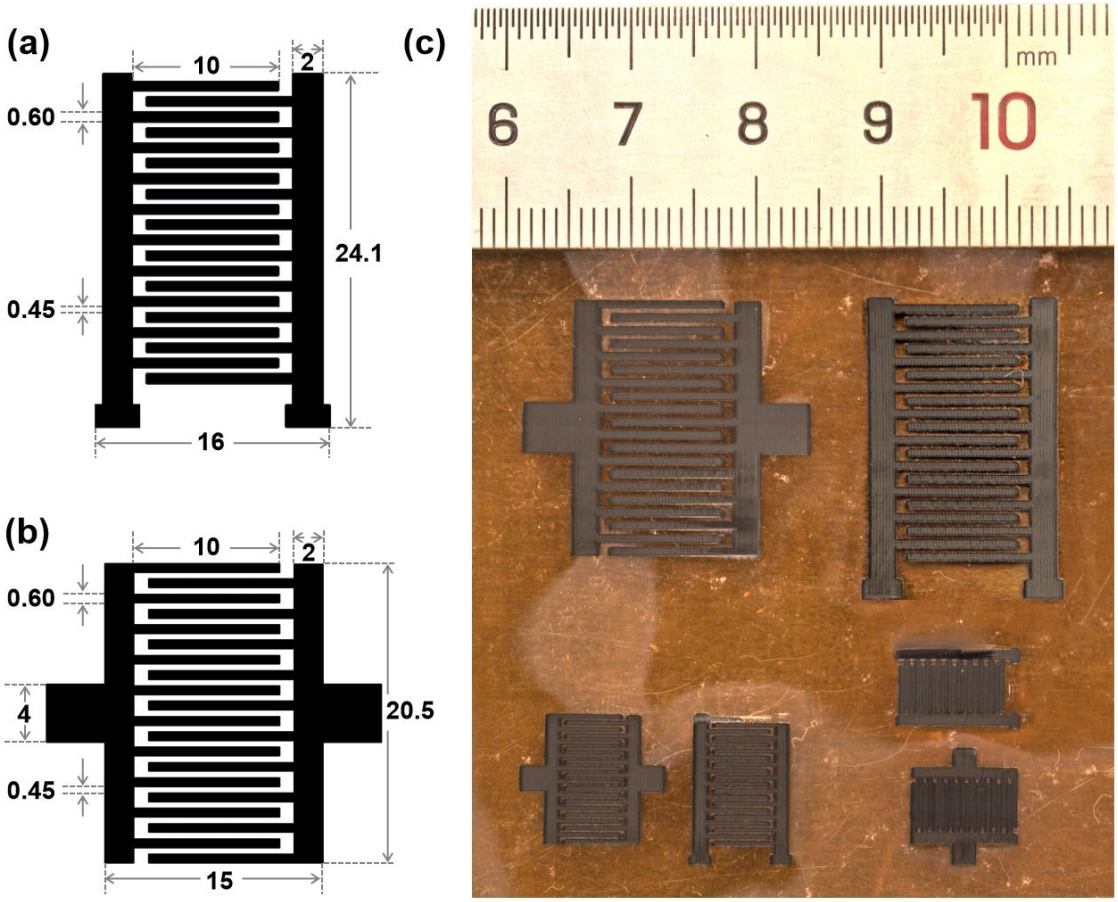

Figure IV.1. (**a**, **b**) Computer-Designed top views (dimensions in mm) of the fabricated devices, showing various configurations of metallic contacts tailored for different application scenarios. (**c**) Digital images of LIG patterned on PI substrates of different sizes.

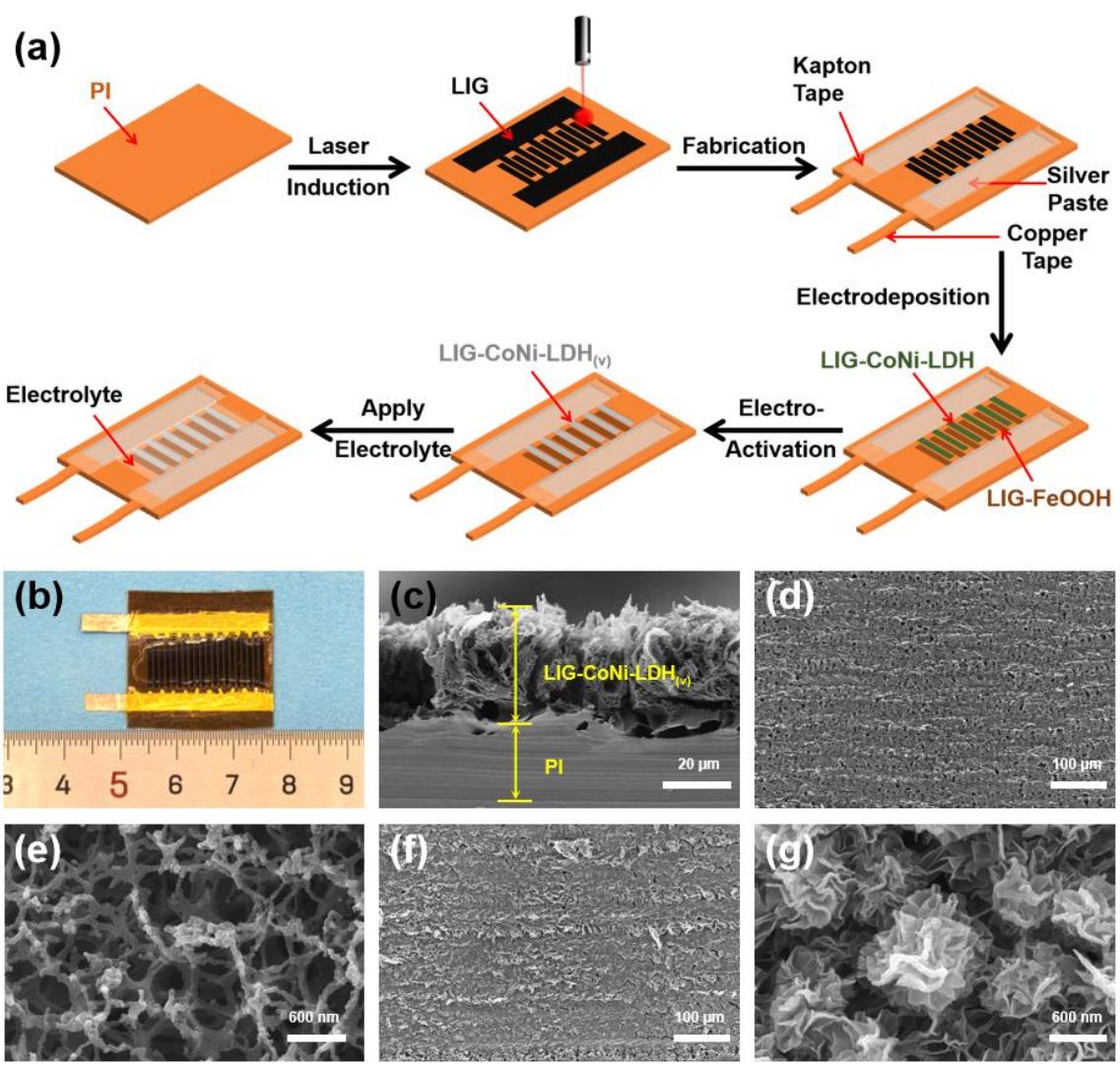

Figure IV.2. (**a**) Schematic illustration of the fabrication process of LIG-CoNi-$LDH_{(v)}$//LIG-FeOOH AMSC. (**b**) Digital photograph of a fabricated AMSC device. (**c**) Cross-sectional SEM image of LIG–CoNi-$50_{(v)}$. Top-view SEM images of (**d,e**) LIG and (**f,g**) CoNi-$50_{(v)}$ within LIG-CoNi-$50_{(v)}$. The line patterns observed in (**d**) and (**f**) result from laser raster scanning.

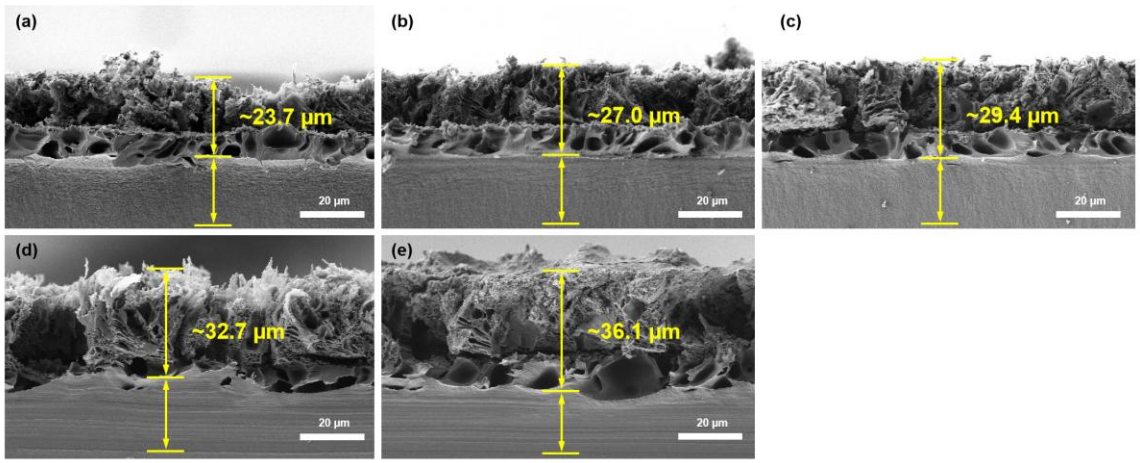

Figure IV.3. Cross-sectional SEM images of (**a**) LIG, (**b**) LIG-CoNi-30$_{(v)}$, (**c**) LIG-CoNi-40$_{(v)}$, (**d**) LIG-CoNi-50$_{(v)}$, and (**e**) LIG-CoNi-60$_{(v)}$ electrodes, showing their respective thicknesses of approximately 23.7, 27.0, 29.4, 32.7, and 36.1 µm.

CoNi-LDH nanosheets were electrodeposited onto the laser-induced graphene (LIG) substrate using cyclic voltammetry (CV). During electrodeposition, OH^- generated from electrochemical reduction of H_2O and NO_3^- reacted with Ni^{2+} and Co^{2+} to form double hydroxides deposited onto the porous conductive network of LIG, as shown in **Figure IV.4a**. The prepared LIG-CoNi-LDH electrode underwent further electrochemical activation via CV in 1 M KOH electrolyte. The activation process was performed within a potential window of 0 to +0.8 V (*vs.* Ag/AgCl) at a scan rate of 100 mV s^{-1} (**Figure IV.4b**). During the initial cycles, the CV curve area progressively increased, reaching a maximum after approximately 10 cycles, after which it became stable. Throughout this process, LDHs were gradually oxidized, resulting in the cleavage of structural O–H bonds. Consequently, hydrogen atoms were released from hydroxyl groups, generating hydrogen vacancies and exposing terminal oxygen sites. Such structural evolution provided abundant active sites, substantially enhancing the storage capacity for cations [54,58]. To further confirm structural changes during electrochemical activation, a series

of spectroscopic measurements were performed. **Figure IV.4c** shows the X-ray diffraction (XRD) patterns of LIG, LIG-CoNi-50, and LIG-CoNi-$50_{(v)}$ electrodes within a range of 10°–44°. The diffraction peak at approximately 26.2° in LIG corresponds to the (002) plane (JCPDS No. 26-1079), indicative of a graphitized structure [56,59]. The broad peak from 12°–22° suggests the presence of amorphous carbon. For the LIG-CoNi-50 electrode, typical peaks observed at 11.3° and 35.5° correspond to the (003) and (012) planes of CoNi-LDH (JCPDS No. 33–0429) [60], while the peak located at around 31.7° corresponds to the (100) plane of $Co(OH)_2/Ni(OH)_2$ (JCPDS No. 30-0443/JCPDS No. 14-0117) [61-63]. However, after electrochemical activation, the XRD pattern of the LIG-CoNi-$50_{(v)}$ electrode exhibited only the graphite substrate peak at 26.2°, whereas the diffraction peaks at 11.3°, 31.7°, and 35.5° became significantly weakened and broadened. This indicates that the LDH structure underwent significant structural transformation, characterized by a reduction of $Co(OH)_2/Ni(OH)_2$ crystalline phases and a transition toward a disordered structure [54,64].

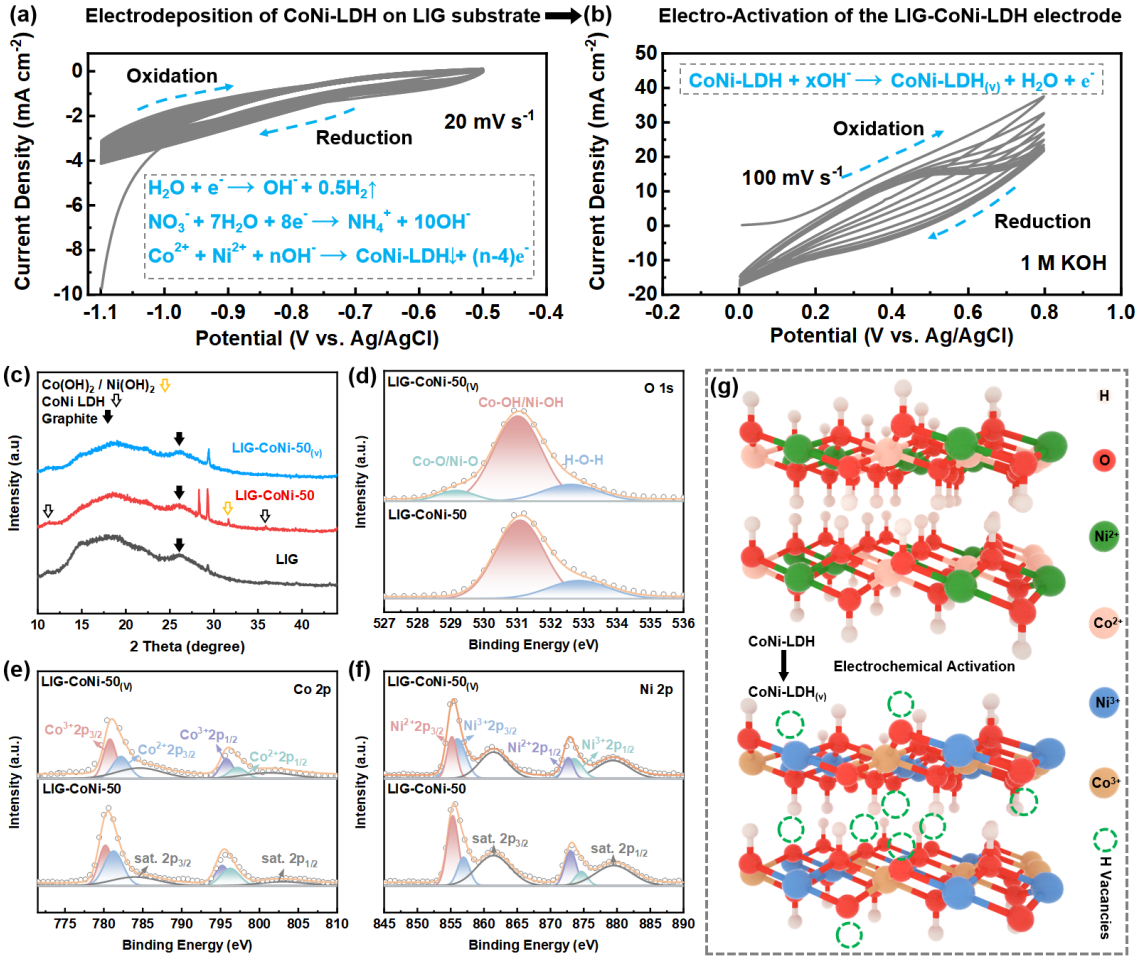

Figure IV.4. (**a**) Cyclic voltammetry (CV) curves recorded during the electrodeposition of CoNi-LDH. (**b**) Electrochemical activation profile of the LIG-CoNi-LDH electrode. (**c**) X-ray diffraction (XRD) patterns of LIG, LIG-CoNi-50, and LIG-CoNi-50$_{(v)}$ electrodes. (**d–f**) X-ray photoelectron spectroscopy (XPS) spectra of (**d**) O 1s, (**e**) Co 2p, and (**f**) Ni 2p. (**g**) Schematic illustration depicting the structural transformation following electrochemical activation.

X-ray photoelectron spectroscopy (XPS) was further employed to characterize changes in the surface electronic structure of CoNi-LDH before and after electrochemical activation. **Figure IV.4d** displays the O 1s spectra of both samples. For the LIG-CoNi-50 electrode, two fitted peaks at 531.1 and 532.8 eV correspond to metal (M)–OH and H–O–

H bonds, respectively. After activation, the O 1s spectrum of the LIG-CoNi-50$_{(v)}$ electrode exhibited a new peak at 529.2 eV, attributed to metal (M)–O bonds. The formation of M–O bonds indicates an irreversible deprotonation of hydroxyl groups in the layered structure, converting M–OH into M–O and generating hydrogen vacancies throughout the LDH structure [64-66]. The Co 2p XPS spectrum of the LIG-CoNi-50 electrode exhibits distinct peaks corresponding to Co^{2+} at binding energies of 781.3 and 796.3 eV, and Co^{3+} at 780.2 and 795.2 eV [67], along with two shake-up satellite peaks located at approximately 783.9 and 802.9 eV [68]. Notably, following activation, a marked decrease in the intensity of the Co^{2+} peak accompanied by an enhancement of the Co^{3+} peak indicates that Co^{2+} undergoes oxidation to Co^{3+} during the activation process (**Figure IV.4e**). Furthermore, the Ni 2p spectra presented in **Figure IV.4f** for both LIG-CoNi-50 and activated LIG-CoNi-50$_{(v)}$ electrodes can be deconvoluted into peaks at 855.3 and 873.2 eV attributed to Ni^{2+}, and at 856.9 and 874.7 eV associated with Ni^{3+}, together with satellite peaks at approximately 861.4 and 879.5 eV [69-71]. The pronounced increase in the Ni^{3+} peak intensity after activation clearly demonstrates the partial oxidation of Ni^{2+} to Ni^{3+} during electrochemical activation. In summary, based on the XPS analysis, the surface electronic structure of CoNi-LDH significantly evolves upon activation, characterized by the deprotonation of M–OH groups to form M–O bonds. This structural change results in partial electron loss from the metal cations, consequently increasing their oxidation states and simultaneously generating hydrogen vacancies within the LDH structure [56]. As illustrated in the FTIR spectra (**Figure IV.5**), a broad absorption band centered at approximately 3450 cm^{-1} corresponds to the O–H stretching vibration. Compared with the LIG-CoNi-50 sample, the LIG-CoNi-50$_{(v)}$ sample exhibits

a noticeable decrease in the intensity of the broad absorption band at around 3450 cm^{-1} in the FTIR spectrum, which is typically associated with O–H stretching vibrations. This attenuation may be attributed to a reduced amount of surface hydroxyl groups or adsorbed water, as a result of electrochemical activation. This interpretation is further supported by the O 1s XPS spectra (**Figure IV.4d**), where the relative proportion of the Co–OH/Ni–OH component (~531.1 eV) decreases significantly after activation [54,64]. This observation supports the formation of hydrogen vacancies during the activation process. The deprotonation of M–OH groups results in the generation of M–O bonds, which aligns well with the XPS analysis. Based on the above findings, it can be concluded that the electrochemical activation process results in the deprotonation of M–OH groups, the oxidation of Co^{2+} and Ni^{2+} ions, and the introduction of hydrogen vacancies within the LDH structure (**Figure IV.4g**). More importantly, the presence of hydrogen vacancies in the LIG-CoNi-$50_{(v)}$ electrode effectively reduces the electrostatic repulsion between cations and metal hydroxide layers, thereby lowering the diffusion barriers for cation transport and significantly enhancing the electrochemical performance of the electrode [56]. Additionally, the activated electrode serves as an active material capable of reversibly storing and releasing cations, making it a promising candidate for electrode applications in cation-based batteries.

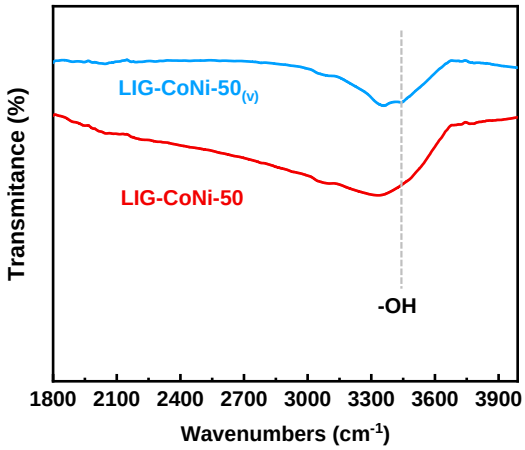

Figure IV.5. FT-IR spectra of LIG-CoNi-50 and LIG-CoNi-50$_{(v)}$ samples.

To investigate the effect of defect engineering, specifically the introduction of hydrogen vacancies, on the electrochemical performance of layered double hydroxides (CoNi-LDH), the electrochemical behaviors of the LIG-CoNi-50 and LIG-CoNi-50$_{(v)}$ electrodes were systematically evaluated in a three-electrode configuration. As illustrated in **Figure IV.6a**, the LIG-CoNi-50$_{(v)}$ electrode was employed as the working electrode, with a Pt foil counter electrode and an Ag/AgCl reference electrode in a 5 M LiCl electrolyte. Additionally, electrochemical activation of the LIG substrate alone was performed under identical experimental conditions (10 cycles of CV in 1 M KOH at a scan rate of 100 mV s^{-1} within a potential window of 0–0.8 V *vs.* Ag/AgCl) to elucidate its contribution to the overall electrochemical performance. **Figure IV.6b** presents cyclic voltammetry (CV) curves recorded for both LIG substrate and LIG-CoNi-50 electrodes, before and after activation, at a scan rate of 50 mV s^{-1} within a potential window of 0–1.0 V (*vs.* Ag/AgCl) in 5 M LiCl electrolyte. Corresponding galvanostatic charge-discharge (GCD) curves and the calculated areal capacitances at a current density of 0.5 mA cm^{-2} are provided in **Figure IV.6c** and **d**, respectively. The results demonstrate that although

the LIG substrate contributes marginally to the total capacitance *via* electric double-layer capacitance (EDLC), its capacitance values remain relatively low (6.55 and 9.09 mF cm^{-2}, before and after activation, respectively), indicating that the predominant capacitive behavior originates from the pseudocapacitance of the activated CoNi LDH. Notably, the pristine LIG-CoNi-50 electrode exhibited limited electrochemical activity in the neutral LiCl electrolyte. In stark contrast, the activated LIG-CoNi-$50_{(v)}$ electrode displayed significantly enhanced electrochemical performance, achieving an areal capacitance as high as 89.61 mF cm^{-2} calculated from the GCD curves—approximately six times greater than that of the pristine electrode (14.10 mF cm^{-2}). These experimental findings clearly illustrate that the introduction of hydrogen vacancies into the CoNi-LDH effectively enhances its charge-storage capability.

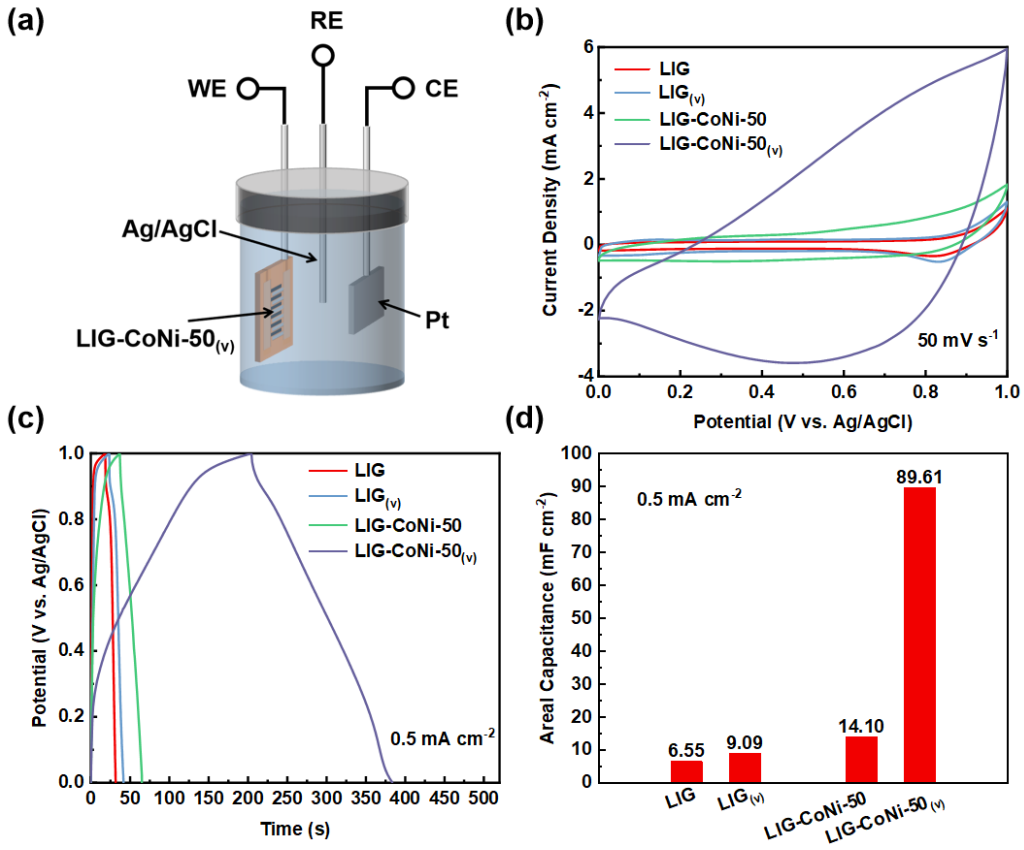

Figure IV.6. (**a**) Schematic diagram of the three-electrode system. (**b**) CV, (**c**) GCD curves, and (**d**) Areal capacitance values of the LIG substrate and LIG-CoNi-50 before and after electrochemical activation.

The electrochemical performance of LIG-CoNi-$X_{(v)}$ electrodes prepared using different deposition cycles was studied in the same three-electrode system. **Figure IV.7** shows the CV curves of $LIG_{(v)}$ and LIG-CoNi-$X_{(v)}$ recorded at various scan rates from 10 to 100 mV s^{-1}, demonstrating increased current density with the scan rate. The CV curve of $LIG_{(v)}$ is negligible, confirming its minimal contribution to the overall capacitance of the LIG-CoNi-$LDH_{(v)}$ composite. **Figure IV.8a** depicts the CV curves acquired at 50 mV s^{-1} of LIG-CoNi-$X_{(v)}$. Among them, the LIG-CoNi-$50_{(v)}$ electrode exhibits the largest integrated CV area, indicating its superior areal capacitance compared to other electrodes with different electrodeposition cycles. Furthermore, the deviation from rectangular shape of the CV curves for LIG-CoNi-$X_{(v)}$ suggests that the capacitive behavior is dominated by pseudocapacitance with good electrochemical reversibility. **Figure IV.8b** displays the GCD curves of $LIG_{(v)}$ and LIG-CoNi-$X_{(v)}$ electrodes recorded at a current density of 0.5 mA cm^{-2} within a voltage window of 0 to 1.0 V (*vs*. Ag/AgCl). The GCD curves of LIG-CoNi-$X_{(v)}$ electrodes exhibit a clear deviation from the ideal triangular shape, typically associated with electric double-layer capacitors, instead showing nonlinear profiles that are characteristic of pseudocapacitive charge storage. Furthermore, the negligible IR drop at the beginning of the discharge process indicates good capacitive behavior and high electrical conductivity. **Figure IV.9** further presents the GCD curves of $LIG_{(v)}$ and LIG-CoNi-$X_{(v)}$ electrodes at various current densities ranging from 0.5 to 10.0 mA cm^{-2}. The GCD response of $LIG_{(v)}$ is minimal and aligns well with its CV behavior in **Figure IV.7a**, confirming its limited electrochemical contribution. Based on

these GCD curves, the areal capacitance of LIG-CoNi-$X_{(v)}$ electrodes was calculated using Eq. Eq.4.1, and the results as a function of current density are plotted in **Figure IV.8c**. As clearly shown, the capacitive performance of LIG–CoNi-$LDH_{(v)}$ electrodes improved progressively with increasing electrodeposition cycles. Notably, LIG-CoNi-$50_{(v)}$ exhibited the highest areal capacitance of 89.61 mF cm^{-2} at a current density of 0.5 mA cm^{-2}. In contrast, LIG-CoNi-$60_{(v)}$ displayed a slightly lower capacitance of 80.28 mF cm^{-2} at the same current density (**Table IV.1**). This observed decline in performance is likely attributed to instability caused by excessive deposition thickness, which may lead to poor adhesion and partial delamination of active material from the substrate, adversely affecting charge storage. Therefore, considering both electrochemical performance and electrode structural integrity, LIG-CoNi-$50_{(v)}$ was selected as the optimal electrode for further investigation.

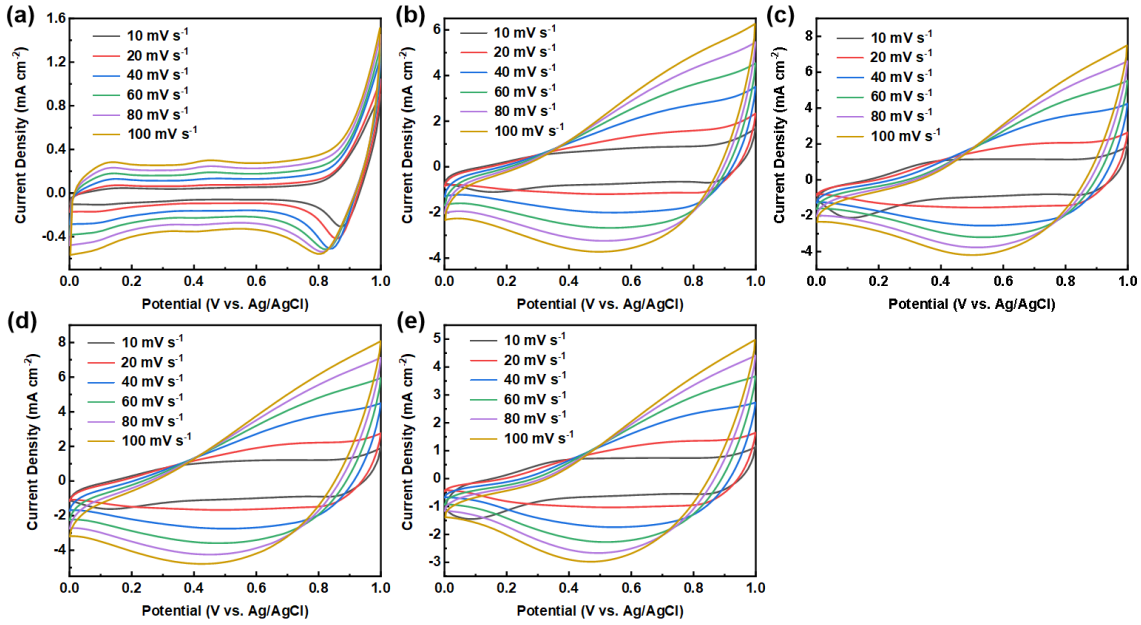

Figure IV.7. Cyclic voltammetry (CV) curves of (**a**) $LIG_{(v)}$, (**b**) LIG-CoNi-$30_{(v)}$, (**c**) LIG-CoNi-$40_{(v)}$, (**d**) LIG-CoNi-$50_{(v)}$, and (**e**) LIG-CoNi-$60_{(v)}$ collected at scan rates ranging from 10 to 100 mV s^{-1} in the potential window of 0–1.0 V (*vs.* Ag/AgCl).

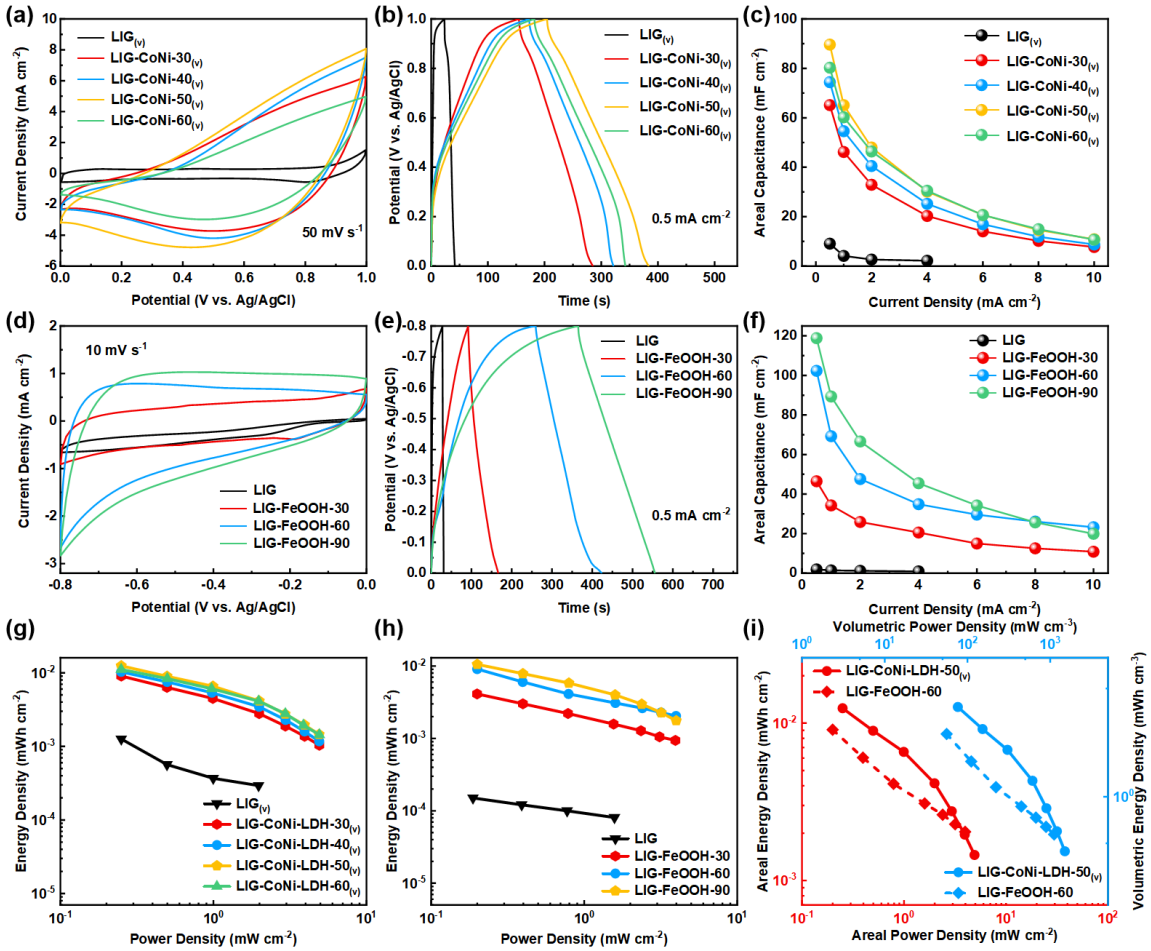

Figure IV.8. Electrochemical performance of LIG–CoNi-LDH$_{(v)}$ and LIG–FeOOH electrodes. (**a**) CV curves of LIG–CoNi-X$_{(v)}$ and LIG at a scan rate of 50 mV s^{-1}. (**b**) GCD curves of LIG–CoNi-X$_{(v)}$ and LIG at a current density of 0.5 mA cm^{-2}. (**c**) Areal capacitance values of LIG–CoNi-X$_{(v)}$ and LIG at current densities from 0.5 to 10.0 mA cm^{-2}. (**d**) CV curves of LIG–FeOOH-Y and LIG at a scan rate of 10 mV s^{-1}. (**e**) GCD curves of LIG–FeOOH-Y and LIG at a current density of 0.5 mA cm^{-2}. (**f**) Areal capacitances of LIG–FeOOH-Y and LIG at current densities ranging from 0.5 to 10.0 mA cm^{-2}. Areal energy and power density of (**g**) LIG–CoNi-X$_{(v)}$, (**h**) LIG–FeOOH-Y. (**i**) Areal and volumetric energy and power densities of LIG-CoNi-50$_{(v)}$ and LIG-FeOOH-60.

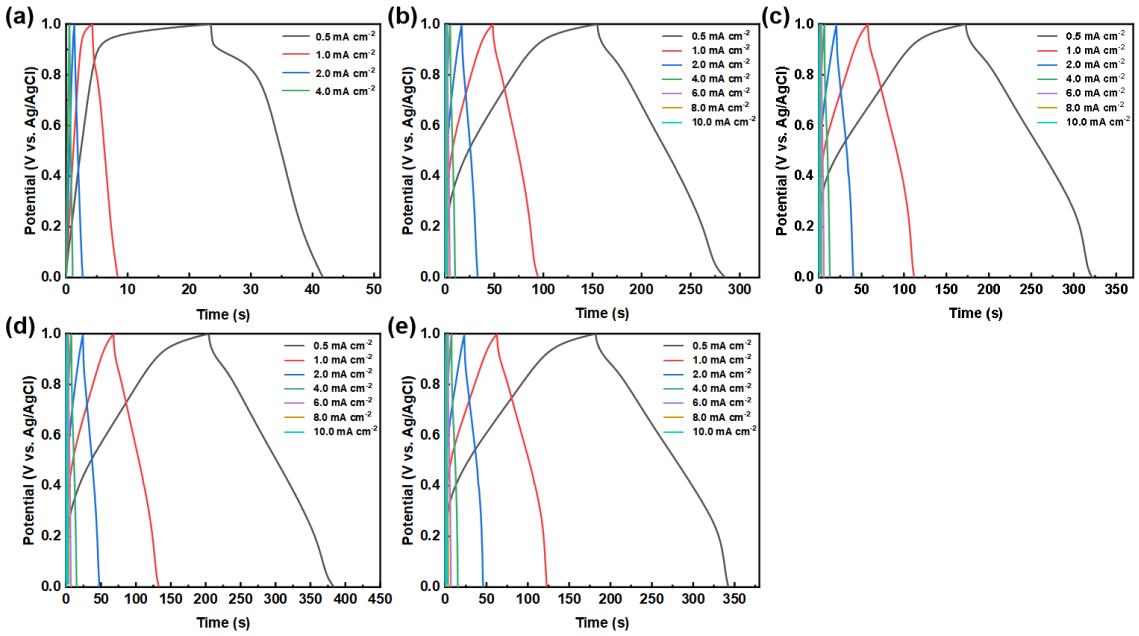

Figure IV.9. Galvanostatic charge–discharge (GCD) curves of (**a**) $LIG_{(v)}$, (**b**) LIG-CoNi-$30_{(v)}$, (**c**) LIG-CoNi-$40_{(v)}$, (**d**) LIG-CoNi-$50_{(v)}$, and (**e**) LIG-CoNi-$60_{(v)}$ measured at current densities ranging from 0.5 to 10.0 mA cm^{-2} in the potential window of 0–1.0 V (*vs.* Ag/AgCl).

Among various pseudocapacitive materials, Fe-based compounds (such as Fe_2O_3, Fe_3O_4, and FeOOH) have attracted significant attention as promising electrode candidates for supercapacitors, owing to their high specific capacitance, low operating potential, cost-effectiveness, and environmental friendliness [72]. In this study, FeOOH was selected as the negative electrode material for assembling an AMSC. A simple electrodeposition technique was employed to grow FeOOH onto the LIG substrate. Taking the LIG-FeOOH-60 electrode (deposited for 60 min) as a representative example, the surface morphology is shown in **Figure IV.10a,b**. The corresponding cross-sectional SEM image (**Figure IV.10c**) reveals a uniform active layer with an average thickness of approximately 35.7 µm. To investigate the elemental composition and oxidation states of

the LIG-FeOOH electrode, X-ray photoelectron spectroscopy (XPS) was conducted, as presented in **Figure IV.11**. In the Fe 2p spectrum **Figure IV.11a**, two main peaks at 710.5 and 724.2 eV, along with satellite peaks at 719.1 and 732.4 eV, are observed—these features are characteristic of Fe^{3+} in FeOOH [73]. The O 1s spectrum (**Figure IV.11b**) depicts two distinct peaks: the lower binding energy peak at 529.5 eV corresponds to Fe–O–Fe bonds, while the higher binding energy peak at 531.0 eV is attributed to Fe–O–H bonds. These results are in good agreement with previously reported FeOOH spectra [74], confirming the successful deposition of FeOOH onto the LIG substrate. To optimize the deposition parameters, a series of LIG-FeOOH-Y electrodes (where Y represents the deposition time) were prepared and systematically evaluated using a three-electrode configuration using CV tests performed in 5 M LiCl electrolyte within a potential window of –0.8 to 0 V (*vs*. Ag/AgCl), using LIG-FeOOH-Y as the working electrode, Pt foil as the counter electrode, and Ag/AgCl as the reference electrode. **Figure IV.12** presents the CV curves of LIG and LIG-FeOOH-Y electrodes at scan rates ranging from 10 to 100 mV s^{-1}. The representative CV profiles at 50 mV s^{-1} are shown in **Figure IV.8d**, where the LIG-FeOOH-90 electrode exhibits the largest integrated CV area, indicating its superior electrochemical activity. GCD measurements were carried out at current densities ranging from 0.5 to 10 mA cm^{-2} (**Figure IV.13**). As evidenced in **Figure IV.13a**, the LIG electrode displays negligible capacitance, consistent with the CV results in **Figure IV.12a**. In contrast, the GCD curves of LIG-FeOOH-Y electrodes (**Figure IV.13b–d**) feature progressively enhanced charge-discharge behavior with increasing deposition time. **Figure IV.8e** displays the GCD profiles of LIG and LIG-FeOOH-Y electrodes at a current density of 0.5 mA cm^{-2}. The

nearly symmetrical charge-discharge curves of the LIG-FeOOH-Y electrodes further confirm their excellent capacitive behavior. The corresponding areal capacitances, calculated based on Eq. (4.**Erreur ! Source du renvoi introuvable.**), are summarized in **Figure IV.8f**. Notably, the LIG-FeOOH-90 electrode delivers the highest areal capacitance of 118.83 mF cm^{-2} at 0.5 mA cm^{-2}, which is significantly larger than that of the bare LIG electrode (1.93 mF cm^{-2} under the same conditions) (**Table IV.1**).

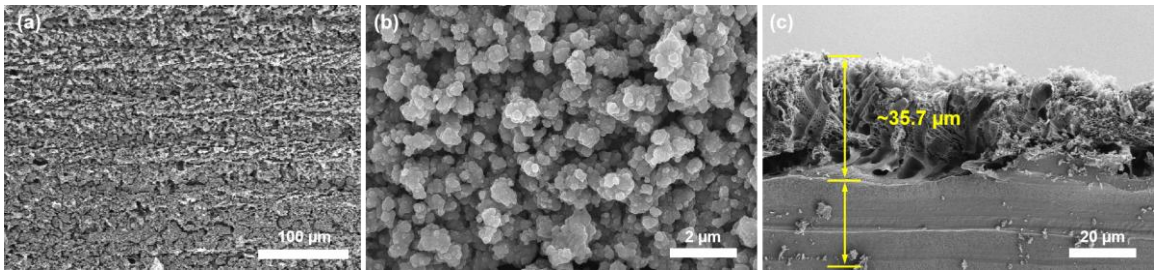

Figure IV.10. (**a, b**) Top-View SEM images of LIG-FeOOH-60 electrode at different magnifications. (**c**) Cross-Sectional SEM image of LIG-FeOOH-60, showing a thickness of approximately 35.7 µm.

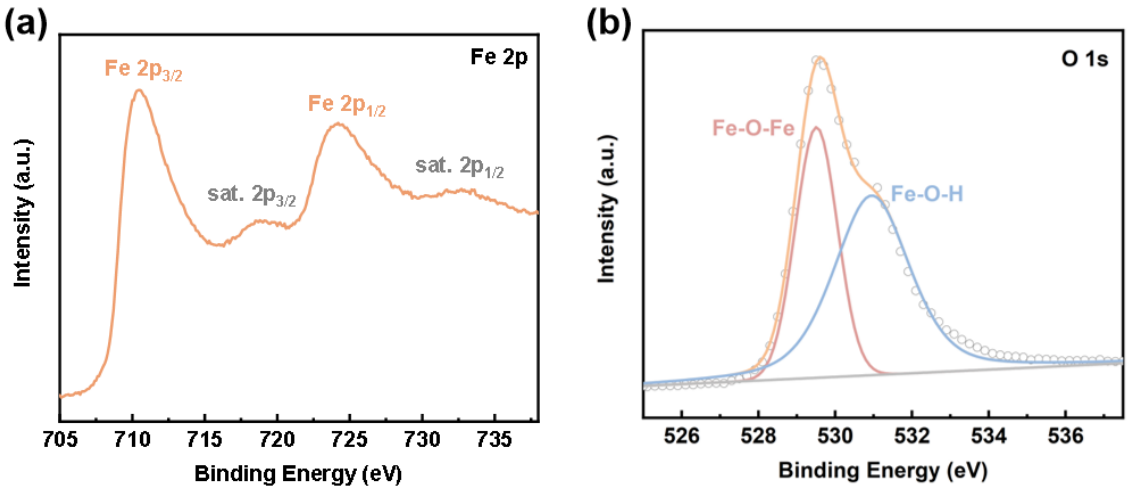

Figure IV.11. (**a**) Fe 2p and (**b**) O 1s XPS spectra of LIG-FeOOH.

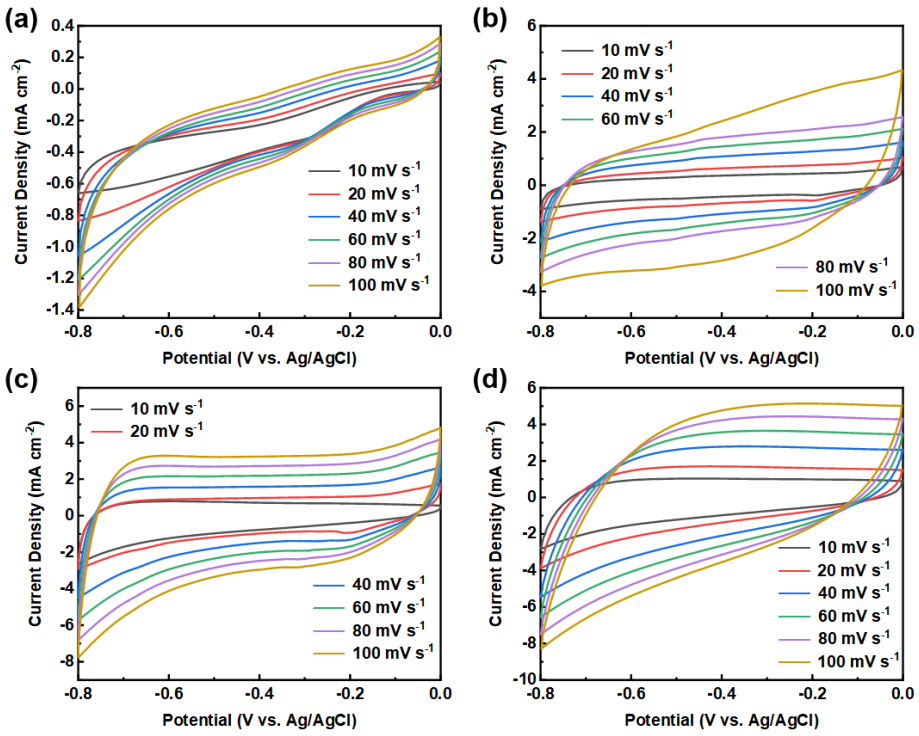

Figure IV.12. CV curves of (**a**) LIG, (**b**) LIG-FeOOH-30, (**c**) LIG-FeOOH-60, and (**d**) LIG-FeOOH-90 collected at scan rates ranging from 10 to 100 mV s^{-1} in the potential window of –0.8 to 0 V (*vs.* Ag/AgCl).

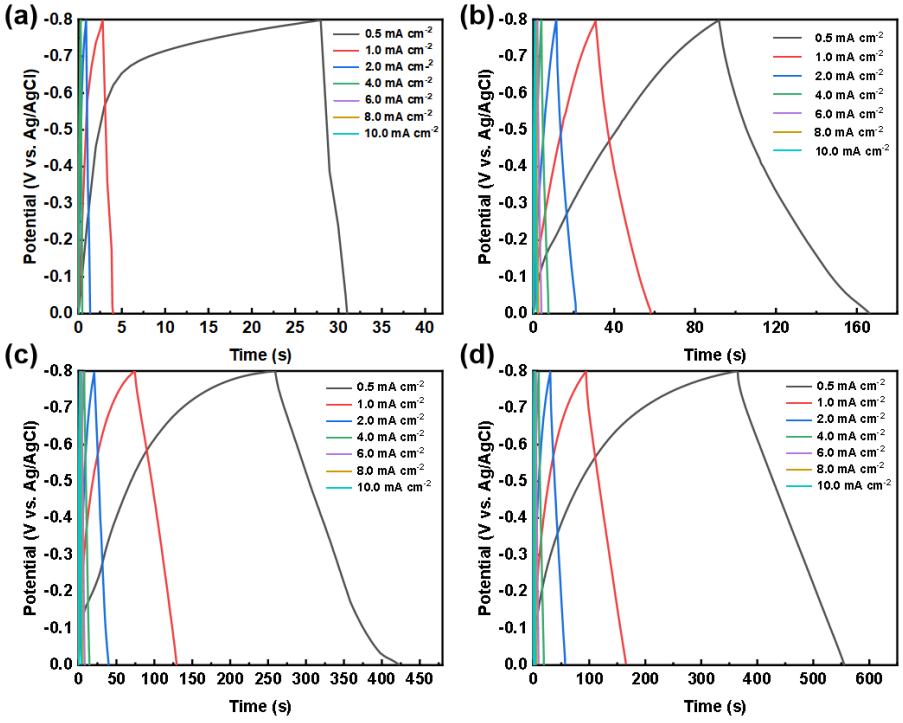

Figure IV.13. Galvanostatic charge–discharge (GCD) curves of (**a**) LIG, (**b**) LIG-FeOOH-30, (**c**) LIG-FeOOH-60, and (**d**) LIG-FeOOH-90 electrodes, measured at various current densities ranging from 0.5 to 10 mA cm^{-2} within a potential window of 0 to –0.8 V (*vs*. Ag/AgCl).

To achieve optimal performance in AMSC, the mass loadings of the negative and positive electrodes must be carefully balanced. Therefore, the areal energy and power densities of LIG-CoNi-$X_{(v)}$ and LIG-FeOOH-Y electrodes were calculated according to Eqs. Eq.4.7 and Eq.4.9, and the results were presented in form of Ragone plots (**Figures IV.8g, h**). Analysis of the Ragone plots indicated that the combination of LIG-CoNi-$50_{(v)}$ and LIG-FeOOH-60 electrodes exhibited superior charge balance. Additionally, volumetric energy and power densities for these electrodes were calculated using Eqs. Eq.4.8 and Eq.4.10, with corresponding Ragone plots presented in **Figure IV.8i**. It is worth noting that both CoNi-LDH and FeOOH are typical pseudocapacitive materials, whose charge storage behavior is primarily governed by surface redox reactions. From a fundamental perspective, such materials should be evaluated using “capacity” (e.g., mC cm^{-2} or mAh g^{-1}), which more accurately reflects their intrinsic charge storage capability. However, for the sake of consistency with previously reported literature and considering that the present study relies mainly on CV and GCD data for energy density calculations, areal capacitance (mF cm^{-2}) is uniformly adopted throughout the main text. To enable direct comparison of charge balance between electrodes, the areal capacities values were calculated using Eqs. (4.**Erreur ! Source du renvoi introuvable.**) and **Eq.4.12**). The calculated results are summarized in **Table IV.1**. At a current density of 0.5 mA cm^{-2}, the areal capacities of the LIG-CoNi-$50_{(v)}$ and LIG-FeOOH-60 electrodes were determined to be 89.58 and 81.81 mC cm^{-2}, respectively, yielding a charge balance ratio of

approximately 0.91. This high level of charge compatibility confirms the excellent electrode matching and supports their integration into high-performance asymmetric supercapacitor systems.

The electrochemical performance of LIG-CoNi-LDH$_{(v)}$//LIG-FeOOH asymmetric micro-supercapacitors (AMSC) using LIG-CoNi-50$_{(v)}$ as the positive electrode, LIG-FeOOH-60 as the negative electrode, and PVA/LiCl as the gel electrolyte was further studied in a two-electrode system. Hereafter, this device configuration is referred to as LIG-CoNi-LDH$_{(v)}$//LIG-FeOOH AMSC for clarity and to avoid repetition. As shown in **Figure IV.14a**, the AMSC exhibited a working voltage window up to 2.0 V at a scan rate of 50 mV s^{-1}. However, to minimize electrode degradation due to polarization effects, a voltage window of 0–1.8 V was selected for subsequent tests. The operating voltage was successfully extended from 1.0 V (*vs.* Ag/AgCl) for the LIG-CoNi-LDH$_{(v)}$ electrode to 1.8 V for the LIG-CoNi-LDH$_{(v)}$//LIG-FeOOH AMSC, by constructing an asymmetric configuration, thereby broadening the electrochemical window. This significant enhancement not only improves the energy density of the device, but also expands its potential for practical applications. To demonstrate the feasibility of integrating the fabricated AMSC with an energy conversion-storage-consumption system, we designed a self-powered configuration using commercial polycrystalline silicon solar cells as the energy harvester. As illustrated in the simplified circuit diagram (**Figure IV.14b**), two solar cells (2 V, 100 mA) were connected in parallel with a LIG-CoNi-LDH$_{(v)}$//LIG-FeOOH AMSC and a red LED (1.8 V, 20 mA). A single-pole double-throw (SPDT) switch was employed to control the connection among these three components. As shown in **Figure IV.14c**, the fabricated LIG-CoNi-LDH$_{(v)}$//LIG-FeOOH AMSC was capable of

powering a commercial red LED after brief charging under simulated sunlight, thereby demonstrating its effective energy harvesting and storage capabilities. Due to ambient lighting conditions, the visibility of the red LED in the video may appear limited. To enhance clarity, the brightness and contrast of the video were adjusted, and the LED's activated state was highlighted for reference. This integrated system demonstrates the potential of the fabricated AMSC for real-world energy storage and self-powered device applications. **Figure IV.15a** illustrates the CV curves of the LIG-CoNi-LDH$_{(v)}$//LIG-FeOOH AMSC at various scan rates within this potential window, indicating excellent capacitive performance. GCD measurements were conducted at current densities ranging from 0.25 to 8 mA cm^{-2} (**Figure IV.15b**). Based on the GCD curves, the areal and volumetric capacitances of the AMSC were calculated using Eqs. Eq.4.5 and Eq.4.6. At 0.25 mA cm^{-2}, the AMSC achieved an area capacitance of 38.28 mF cm^{-2} and a volumetric capacitance of 5.60 F cm^{-3} (**Figure IV.15c**) (**Table IV.1**). EIS tests were conducted, as depicted in **Figure IV.15d**. The Nyquist plot of the CoNi-LDH//FeOOH AMSC exhibited a small semicircle in the high-frequency region and a linear region at low frequencies, representing charge transfer and ion diffusion processes, respectively. The internal resistance (R_s) was determined as 11.8 Ω and the charge transfer resistance (R_{ct}) was calculated to be 96.9 Ω, indicating moderate internal resistance and diffusion-controlled electrochemical processes. In addition to the good electrochemical performance, the LIG-CoNi-LDH$_{(v)}$//LIG-FeOOH AMSC displayed enhanced mechanical flexibility.

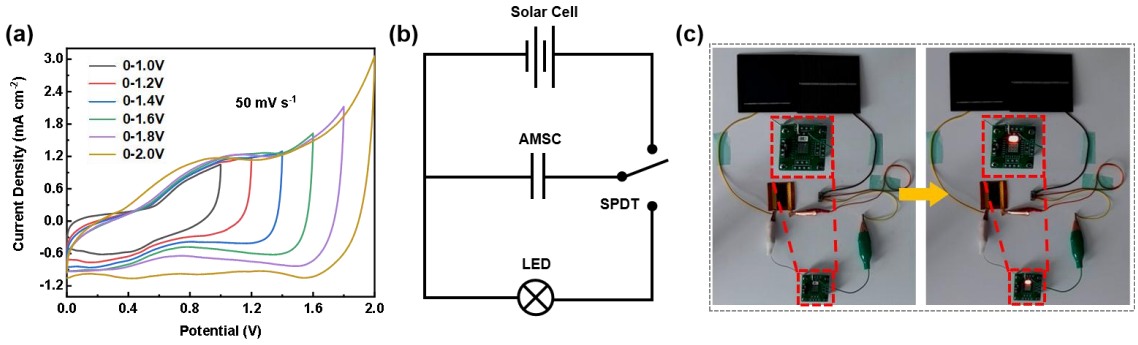

Figure IV.14. (a) CV curves of the LIG-CoNi-LDH$_{(V)}$//LIG-FeOOH AMSC collected under various potential windows at a scan rate of 50 mV s^{-1}. **(b)** Schematic illustration of the integrated self-powered system, comprising a solar cell as the energy harvester, an AMSC as the energy storage unit, and an LED as the energy consumer. **(c)** Optical image of the prototype system in operation, where the AMSC powers a commercial red LED after being charged by solar cells under simulated sunlight.

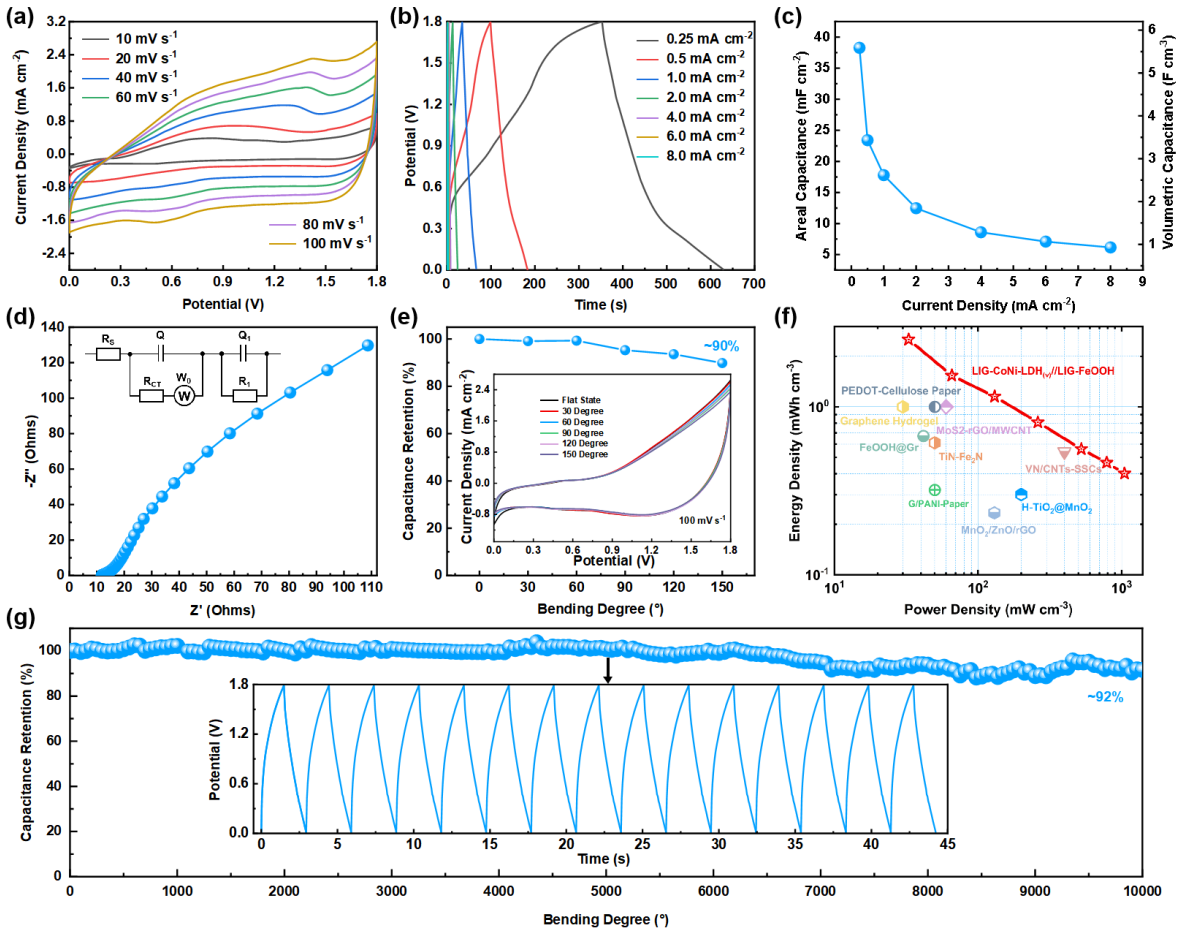

Figure IV.15. Electrochemical performance of LIG-CoNi-LDH$_{(v)}$//LIG-FeOOH ASC devices. (**a**) CV curves at scan rates from 10 to 100 mV s^{-1}. (**b**) GCD curves at current densities (0.25 to 8.0 mA cm^{-2}). (**c**) Areal and volumetric capacitance values at various current densities (0.25 to 8 mA cm^{-2}). (**d**) Electrochemical impedance spectroscopy (EIS) from 100 mHz to 100 kHz. (**e**) Comparison of capacitance retention under different bending states versus the flat state. Inset: CV curves at 100 mV s^{-1}. (**f**) Ragone plot comparing this work with other MSC systems. (**g**) Long-term cycling performance of LIG-CoNi-LDH$_{(v)}$//LIG-FeOOH at 4 mA cm^{-2}. Inset: Typical GCD curves showing capacitive behavior during cycling.

As shown in **Figure IV.15e** and **Figure IV.16**, the CV and GCD curves remained stable under bending angles from 0 to 150°, demonstrating high structural stability. Energy and power densities, critical for comparing energy storage systems, were calculated using Eqs. Eq.4.8 and Eq.4.10 and are shown in the Ragone plot (**Figure IV.15f**). A maximum volumetric energy density of 2.52 mWh cm^{-3} was achieved at a power density of 32.88 mW cm^{-3}, and the device provided an energy density of 0.40 mWh cm^{-3} at a high power density of 1047.68 mW cm^{-3} (**Table IV.1**). This performance is comparable to or surpasses that of previously reported MSC devices (**Table IV.2**). Furthermore, the cycling stability of LIG-CoNi-LDH$_{(v)}$//LIG-FeOOH AMSC was evaluated by extended GCD cycling, achieving a capacitance retention rate of 92% after 10,000 cycles, demonstrating good cycling stability (**Figure IV.15g**).

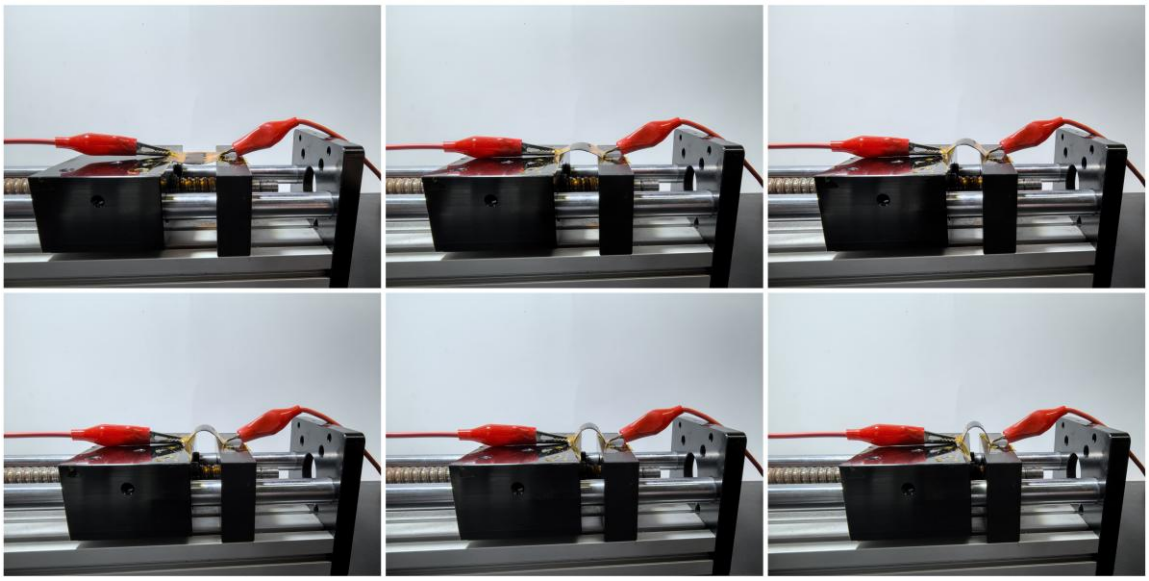

Figure IV.16. Photographs of LIG-CoNi-LDH$_{(v)}$//LIG-FeOOH AMSC with interdigital electrode design under various bending states.

To evaluate the ion storage capability of the LIG-CoNi-LDH$_{(v)}$//LIG-FeOOH AMSC in various electrolyte environments, neutral gel electrolytes containing different metal ions (Na^+, K^+, and Ca^{2+}) were prepared using a method analogous to that employed for the PVA/LiCl gel electrolyte. **Figure IV.17a** presents the CV curves of the AMSC recorded at a scan rate of 50 mV s^{-1} in NaCl-, KCl-, and $CaCl_2$- based gel electrolytes. The device exhibits slightly different electrochemical responses depending on the type of cation, yet consistently demonstrates favorable capacitive behavior, confirming its applicability in diverse neutral gel electrolytes. GCD measurements were further performed at a current density of 0.5 mA cm^{-2} (**Figure IV.17b**). The nearly symmetrical charge-discharge profiles observed in all three electrolytes reinforce the excellent capacitive characteristics of the AMSC. **Figure IV.17c** summarizes the areal capacitance values calculated from the GCD curves using Eq. (4.**Erreur ! Source du renvoi introuvable.**), across a range of current densities from 0.5 to 10 mA cm^{-2} and the corresponding areal capacities values

were calculated using Eq. (4.**Eq.4.15**). At a current density of 0.5 mA cm^{-2}, the AMSC exhibits areal capacitances of 15.83, 14.11, and 10.24 mF cm^{-2}, and corresponding areal capacities of 27.43, 24.92, and 17.67 mC cm^{-2} in NaCl, KCl, and $CaCl_2$ gel electrolytes, respectively. These results confirm the device's robust electrochemical performance across a variety of neutral gel electrolytes containing different cations, highlighting its multifunctionality and potential for broader practical applications.

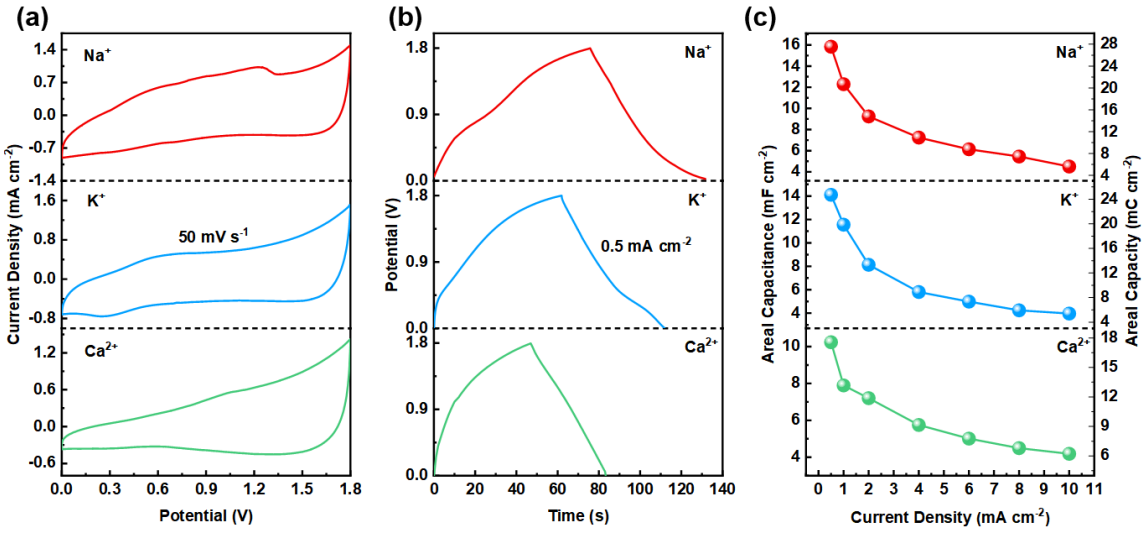

Figure IV.17. (**a**) CV curves of LIG-CoNi-$LDH_{(V)}$//LIG-FeOOH AMSC in NaCl-, KCl-, and $CaCl_2$-based gel electrolytes at 50 mV s^{-1}. (**b**) GCD curves of the same device recorded at 0.5 mA cm^{-2} in the respective gel electrolytes. (**c**) Areal capacitances and areal capacities calculated under various current densities (0.5–10 mA cm^{-2}) in NaCl, KCl, and $CaCl_2$ gel electrolytes.

Table IV.1. Summary of Electrochemical Performance Metrics for All Electrode Configurations.

Electrode Sample	Electrolyte	Capacitance		Capacity		Energy Density		Power Density	
		Areal ($mF\ cm^{-2}$)	Volumetric ($F\ cm^{-3}$)	Areal ($mC\ cm^{-2}$)	Volumetric ($C\ cm^{-3}$)	Areal ($\mu Wh\ cm^{-2}$)	Volumetric ($mWh\ cm^{-3}$)	Areal ($\mu W\ cm^{-2}$)	Volumetric ($mW\ cm^{-3}$)
$LIG_{(v)}$	5M LiCl	9.09	3.84	9.08	3.83	1.26	0.53	249.74	105.38
LIG-CoNi-$30_{(v)}$	5M LiCl	65.14	19.92	65.10	19.91	9.04	2.76	249.85	76.41
LIG-CoNi-$40_{(v)}$	5M LiCl	74.43	22.76	74.30	22.72	10.30	3.15	249.58	76.32
LIG-CoNi-$50_{(v)}$	5M LiCl	89.61	27.40	89.58	27.40	12.44	3.80	249.93	76.43
LIG-CoNi-$60_{(v)}$	5M LiCl	80.28	24.55	80.14	24.51	11.11	3.40	249.58	76.32
LIG	5M LiCl	1.93	0.81	1.44	0.61	0.15	0.06	187.58	79.15
LIG-FeOOH-30	5M LiCl	46.49	13.02	37.11	10.40	4.11	1.15	199.54	55.90
LIG-FeOOH-60	5M LiCl	102.34	28.67	81.81	22.92	9.08	2.54	199.86	55.98
LIG-FeOOH-90	5M LiCl	118.83	33.29	95.04	26.62	10.56	2.96	199.94	56.01
LIG-CoNi-$LDH_{(v)}$//LIG-FeOOH AMSC	PVA/LiCl	38.28	5.60	68.87	10.07	17.21	2.52	224.88	32.88

Notes:

1 The capacitance, capacity, energy density, and power density of the samples were calculated under the following conditions: 0.5 mA cm^{-2} for the LIG-CoNi-$LDH_{(v)}$ and LIG-FeOOH electrodes, and 0.25 mA cm^{-2} for the LIG-CoNi-$LDH_{(v)}$//LIG-FeOOH AMSC.

2 The capacitance reported for the LIG-CoNi-$LDH_{(v)}$//LIG-FeOOH AMSC refers to the total device capacitance, rather than the capacitance of individual electrodes.

3 The areal and volumetric capacities ($mC \cdot cm^{-2}$ and $C \cdot cm^{-3}$) were calculated using Eqs.11-16 based on GCD data.

Table IV.2. Comparative electrochemical performance of reported MSC devices and the current work, including electrode material, electrolyte, testing conditions, volumetric capacitance, energy density, and power density.

Electrode Material	**Electrolyte**	**Test Condition**	**Volumetric Capacitance ($F\ cm^{-3}$)**	**Energy Density ($mWh\ cm^{-3}$)**	**Power Density ($mW\ cm^{-3}$)**	**Refs**
MoS_2-rGO/MWCNT	PVA/H_2SO	2.0 A cm^{-3}	3.80	1.00	60.0	[75]
Graphene hydrogel	PVA/H_2SO_4	1 A g^{-1}	31.00	1.00	30.0	[76]
PEDOT-Cellulose Paper	PVA/H_2SO_4	0.5 A cm^{-3}	115.00	1.00	50.0	[77]
FeOOH@Gr	2 M KOH	-	-	0.67	41.7	[78]
TiN-Fe_2N	PVA/LiCl	2.0 A g^{-1}	60.00	0.61	50.0	[79]
VN/CNTs-SSCs	PVA/H_3PO_4	0.025 A cm^{-3}	7.90	0.54	400.0	[80]
MnO_2/ZnO/rGO	PVA/LiCl	10.0 mV s^{-1}	0.52	0.23	130.0	[81]
H-TiO_2@MnO_2	PVA/LiCl	0.5 mA cm^{-2}	0.70	0.30	200.0	[82]
G/PANI-Paper	PVA/H_2SO_4	0.05 A cm^{-3}	3.55	0.32	50.0	[83]
LIG-CoNi-$LDH_{(v)}$//LIG-FeOOH AMSC	PVA/LiCl	0.25 mA cm^{-2}	5.60	2.52	32.88	**This work**

IV.5. Conclusion

In summary, this study proposes a novel approach for constructing high-performance asymmetric micro-supercapacitors (AMSCs) by integrating laser-induced graphene (LIG) with hydrogen-vacancy-enriched layered double hydroxides ($CoNi\text{-}LDH_{(v)}$). The device architecture was realized through CO_2 laser patterning of porous interdigitated LIG electrodes on polyimide (PI) substrates, followed by electrodeposition of pseudocapacitive materials, with $CoNi\text{-}LDH_{(v)}$ and FeOOH serving as the positive and negative electrodes, respectively. The fabricated LIG-$CoNi\text{-}LDH_{(v)}$//LIG-FeOOH AMSC demonstrated a broad operating voltage window of 0–1.8 V, obviating the need for additional current collectors, binders, or separators. Moreover, the interdigitated electrode design effectively prevented short circuits, contributing to enhanced energy density, power density, cycling stability, and mechanical flexibility. Electrochemical analyses revealed that the optimized LIG-$CoNi\text{-}LDH_{(v)}$//LIG-FeOOH AMSC delivered superior areal and volumetric capacitances of 38.28 mF cm^{-2} and 5.60 F cm^{-3}, respectively, at a current density of 0.25 mA cm^{-2}. Significantly, the device exhibited robust electrochemical performance across various neutral gel electrolytes containing diverse cations (Li^+, Na^+, K^+, Ca^{2+}), highlighting its versatility and potential for broader applicability. Experimental insights further emphasized the critical role of hydrogen vacancies in enhancing the intercalation chemistry and energy storage capabilities of CoNi-LDH. This research not only introduces a scalable and environmentally friendly approach to fabricating high-performance AMSC, but also significantly extends the application potential of defect engineering strategies in advanced energy storage

materials. Moreover, the practical demonstration of LED lighting powered by the AMSC under solar charging illustrates its applicability in integrated and self-sustaining electronic devices.

References

[1] X. F. Lu, Y. Fang, D. Luan, X. W. D. Lou, Nano Lett. 2021, 21, 1555−1565.

[2] A. Noori, M. F. El-Kady, M. S. Rahmanifar, R. B. Kaner, M. F. Mousavi, Chem. Soc. Rev. 2019, 48, 1272−1341.

[3] A. Elgendy, N. M. El Basiony, F. El-Taib Heakal, A. E. Elkholy, J. Power Sources. 2020, 466, 228294.

[4] M. Li, A. Addad, P. Roussel, S. Szunerits, R. Boukherroub, J. Colloid Interface Sci. 2020, 579, 520−530.

[5] R.V. Noorden, Nature. 2014, 507, 26–28.

[6] D. P. Dubal, N. R. Chodankar, D. H. Kim, P. Gomez-Romero, Chem. Soc. Rev. 2018, 47, 2065−2129.

[7] L. Li, Z. Lou, D. Chen, K. Jiang, W. Han, G. Shen, Small. 2018, 14, 1702829.

[8] S. Zheng, Z.S. Wu, F. Zhou, X. Wang, J. Ma, C. Liu, Y.B. He, X. Bao, Nano Energy. 2018, 51, 613−620.

[9] C. Zhang, Z. Peng, C. Huang, B. Zhang, C. Xing, H. Chen, H. Cheng, J. Wang, S. Tang, Nano Energy. 2021, 81, 105609.

[10] S. Kumar, A. Misra, Nanoscale. 2021, 13, 19453−19465.

[11] C.W. Wu, B. Unnikrishnan, I. W. P. Chen, S. G. Harroun, H.T. Chang, C.C. Huang, Energy Storage Mater. 2020, 25, 563−571.

[12] H. Guo, M. Qiao, J. Yan, L. Jiang, J. Yu, J. Li, S. Deng, L. Qu, Adv. Funct. Mater. 2023, 33, 2213514.

[13] S. Xu, F. Xia, Z. Li, X. Wang, IEEE Electr. Device Lett. 2022, 43, 474−477.

[14] K.-H. Choi, J. Yoo, C. K. Lee, S.-Y. Lee, Energy Environ. Sci. 2016, 9, 2812−2821.

[15] J. Li, S. Sollami Delekta, P. Zhang, S. Yang, M. R. Lohe, X. Zhuang, X. Feng, M. Östling, ACS Nano. 2017, 11, 8249−8256.

[16] X. Li, H. Li, X. Fan, X. Shi, J. Liang, Adv. Energy Mater. 2020, 10, 1903794.

[17] Y. Li, M. Zhu, V. K. Bandari, D. D. Karnaushenko, D. Karnaushenko, F. Zhu, O. G. Schmidt, Adv. Energy Mater. 2022, 12, 2103641.

[18] Z. Qu, M. Zhu, Y. Yin, Y. Huang, H. Tang, J. Ge, Y. Li, D. D. Karnaushenko, D. Karnaushenko, O. G. Schmidt, Adv. Energy Mater. 2022, 12, 2200714.

[19] P. Zhuang, Y. Sun, L. Li, M. O. L. Chee, P. Dong, L. Pei, H. Chu, Z. Sun, J. Shen, M. Ye, P. M. Ajayan, Adv. Mater. 2020, 32, 1908072.

[20] Y. Chyan, R. Ye, Y. Li, S. P. Singh, C. J. Arnusch, J. M. Tour, ACS Nano. 2018, 12, 2176−2183.

[21] F. Wang, K. Wang, B. Zheng, X. Dong, X. Mei, J. Lv, W. Duan, W. Wang, Mater. Technol. 2018, 33, 340–356.

[22] A. Ladrón-de-Guevara, A. Boscá, J. Pedrós, E. Climent-Pascual, A. de Andrés, F. Calle, J. Martínez, Appl. Surf. Sci. 2019, 691–697.

[23] L. Cao, S. Zhu, B. Pan, X. Dai, W. Zhao, Y. Liu, W. Xie, Y. Kuang, X. Liu, Carbon. 2020, 163, 85–94.

[24] R. Ye, D.K. James, J.M. Tour, Adv. Mater. 2019, 31, e1803621.

[25] M. Abdulhafez, G.N. Tomaraei, M. Bedewy, ACS Appl. Nano Mater. 2021, 4, 2973–2986.

[26] W. Ma, J. Zhu, Z. Wang, W. Song, G. Cao, Mater. Today Energy. 2020, 18, 100569.

[27] T.S.D. Le, H.P. Phan, S. Kwon, S. Park, Y. Jung, J. Min, B.J. Chun, H. Yoon, S.H. Ko, S.W. Kim, Adv. Funct. Mater. 2022, 32, 2205158.

[28] Z. Peng, R. Ye, J. A. Mann, D. Zakhidov, Y. Li, P. R. Smalley, J. Lin, J. M. Tour, ACS Nano. 2015, 9, 5868–5875.

[29] R. Ye, Z. Peng, T. Wang, Y. Xu, J. Zhang, Y. Li, L. G. Nilewski, J. Lin, J. M. Tour, ACS Nano. 2015, 9, 9244–9251.

[30] X. Li, W. Cai, K. S. Teh, M. Qi, X. Zang, X. Ding, Y. Cui, Y. Xie, Y. Wu, H. Ma, Z. Zhou, Q. A. Huang, J. Ye, L. Lin, ACS Appl. Mater. Interfaces. 2018, 10, 26357–26364.

[31] P. Simon, Y. Gogotsi, Acc. Chem. Res. 2013, 46, 1094–1103.

[32] Y. Xie, J. Zhang, H. Xu, T. Zhou, Chem. Eng. J. 2022, 437, 135493.

[33] W. Zhang, R. Li, H. Zheng, J. Bao, Y. Tang, K. Zhou, Adv. Funct. Mater. 2021, 31, 2009057.

[34] C.-C. Liu, D.-S. Tsai, W.-H. Chung, K.-W. Li, K.-Y. Lee, Y.-S. Huang, J. Power Sources. 2011, 196, 5761–5768.

[35] W. Jiang, D. Yu, Q. Zhang, K. Goh, L. Wei, Y. Yong, R. Jiang, J. Wei, Y. Chen, Adv. Funct. Mater. 2015, 25 1063–1073.

[36] Y. Yang, H. Fei, G. Ruan, C. Xiang, J.M. Tour, Adv. Mater. 2014, 26, 8163–8168.

[37] Z. Chen, J.W.F. To, C. Wang, Z. Lu, N. Liu, A. Chortos, L. Pan, F. Wei, Y. Cui, Z. Bao, Adv. Energy Mater. 2014, 4, 1400207–1400216.

[38] N. Zhao, H. Fan, M. Zhang, J. Ma, Z. Du, B. Yan, H. Li, X. Jiang, Chem. Eng. J. 2020, 390, 124477.

[39] M. Li, A. Addad, M. Dolci, P. Roussel, M. Naushad, S. Szunerits, R. Boukherroub, Chem. Eng. J. 2020, 396, 125370.

[40] L. X. Du, D. Zhang, Y. Xing, W. Xue, Yan. Z, J. Mater. Chem. A. 2017, 5, 15460–15485.

[41] F. Wang, J. Xie, D. Zheng, F. Yang, H. Zhang, X. Lu, Adv. Mater. 2022, 34, 2200085.

[42] L. Ma, Q. Wang, S. M. Islam, Y. Liu, S. Ma, M. G. Kanatzidis, J. Am. Chem. Soc. 2016, 138, 2858–2866.

[43] J. Wang, Y. Zhang, J. Zhu, J. Hou, J. Liu and B. Van der Bruggen, J. Membr. Sci. 2016, 510, 27–37.

[44] F. Ning, M. Shao, S. Xu, Y. Fu, R. Zhang, M. Wei, D. G. Evans and X. Duan, Energy Environ, Sci. 2016, 9, 2633–2643.

[45] H. Liu, Y. Wang, X. Lu, Y. Hu, G. Zhu, R. Chen, L. Ma, H. Zhu, Z. Tie, J. Liu, Nano Energy. 2017, 35, 350–357.

[46] F. Yang, B. Wang, H. Su, S. Zhou and Y. Kong, Mater. Chem. Front. 2017, 1, 2065–2077.

[47] H. Li, Y. Gao, C. Wang, G. Yang, Adv. Energy Mater. 2015, 5, 1401767–1401775.

[48] Y. Zhao, G. Chen, T. Bian, C. Zhou, G. I. Waterhouse, L. Z. Wu, C. H. Tung, L. J. Smith, D. O'Hare and T. Zhang, Adv. Mater. 2015, 27, 7824–7831.

[49] J. A. Carrasco, A. Harvey, D. Hanlon, V. Lloret, D. McAteer, R. Sanchis-Gual, A. Hirsch, F. Hauke, G. Abellan, J. N. Coleman and E. Coronado, Chem. Commun. 2019, 55, 3315–3318.

[50] P. F. Liu, S. Yang, B. Zhang and H. G. Yang, ACS Appl. Mater. Interfaces. 2016, 8, 34474–34481.

[51] Y. Xie, B. Fei, D. Cai, Q. Chen, Z. Cui, Q. Wang, H. Zhan, Energy Storage Mater. 2020, 31, 27–35.

[52] W. Qiao, W. Xie, J. Li, B. Jin, K. Fan, J. Li, M. Shao, M. Wei, ACS Appl. Energy Mater. 2021, 4, 6302–6309.

[53] Z. Li, H. Duan, M. Shao, J. Li, D. O'Hare, M. Wei, Z. L. Wang, Chem. 2018, 4, 2168–2179.

[54] J. Meng, Y. Song, Z. Qin, Z. Wang, X. Mu, J. Wang, X. Liu, Adv. Mater. 2022, 32, 2204026.

[55] B. Jin, J. Gao, Y. Zhang, M. Shao, Smart Mol. 2024, 2, e20230026.

[56] L. Li, J. Zhang, Z. Peng, Y. L, C. Gao, Y. Ji, R. Ye, N. D. Kim, Q. Zhong, Y. Yang, H. Fei, G. Ruan, J. M. Tour, Adv. Mater. 2016, 28, 838–845.

[57] J. W. Gittins, Y. Chen, S. Arnold, V. Augustyn, A. Balducci, T. Brousse, E. Frackowiak, P. G. Romero, A. Kanwade, L. Kops, P. K. Jha, D. Lyu, M. Meo, D. Pandey, L. Pang, V. Presser, M. Rapisarda, D. R. Garcia, S. Saeed, P. M. Shirage, A. Slesinski, F. Soavi, J. Thomas, M. M. Titirci, H. Wang, Z. Xu, A. Yu, M. Zhang, A. C. Forse, J. Power Sources. 2023, 585, 233637.

[58] Y. Zhao, P. Zhang, J. Liang, X. Xia, L. Ren, L. Song, W. Liu, and X. Sun, Adv. Mater. 2022, 34, 2204320.

[59] S. Wei, X. Deng, W. Li, K. Liu, J. Wang, H. Zhao, X. Wang, Chem. Eng. J. 2023, 455, 140540.

[60] W. Guo, C. Dun, C. Yu, X. Song, F. Yang, W. Kuang, Y. Xie, S. Li, Z. Wang, J. Yu, G. Fu, J. Guo, M. A. Marcus, J. J. Urban, Q. Zhang, J. Qiu, Nat. Commun. 2022, 13, 1409.

[61] V. Kumar, H. S. Panda, Bull. Mater. Sci. 2022, 45, 25.

[62] S. Lin, T. Zhang, Y. Liu, H. Yang, J. Alloys Compd. 2022, 914, 165360.

[63] L. Zhu, H. Zhang, L. Zhong, J. Zheng, C. Yu, N. Zhang, B. H. Chen, Fuel. 2018, 216, 208–217.

[64] Q. Pan, P. Hei, Y. Song, J. Meng, C. Liu, X. Liu, Nano Res. 2023, 16, 2495–2501.

[65] Y. Zhang, B. Ouyang, J. Xu, G. Jia, S. Chen, R. S. Rawat, H. J. Fan, Angew. Chem. Int. Ed. 2016, 55, 8670–8674.

[66] H. Xing, X. Deng, X. Wang, J. Colloid Interface Sci. 2025, 679, 43–53.

[67] C. Wang, H. Shang, Y. Wang, H. Xu, J. Li, Y. Du, J. Mater. Chem. A. 2021, 9, 14601–14606.

[68] J. Chen, J. Xu, S. Zhou, N. Zhao, C. Wong, Nano Energy. 2016, 21, 145–153.

[69] J.G. Kim, D.L. Pugmire, D. Battaglia, M.A. Langell, Appl. Surf. Sci. 2000, 165, 70–84.

[70] Y.J. Wei, L.Y. Yan, C.Z. Wang, X.G. Xu, F. Wu, G. Chen, J. Phys. Chem. B. 2004, 108, 18547–18551.

[71] M.C. Biesinger, L.W. Lau, A.R. Gerson, R.S. Smart, Phys. Chem. Chem. Phys. 2012, 14, 2434–2442.

[72] X. Lu, Y. Zeng, M. Yu, T. Zhai, C. Liang, S. Xie, M.S. Balogun, Y. Tong, Adv. Mater. 2014, 26, 3148–3155.

[73] Q. Yu, X. Meng, T. Wang, P. Li, J. Ye, Adv. Funct. Mater. 2015, 25, 2686–2692.

[74] J. Chen, J. Xu, S. Zhou, N. Zhao, C. Wong, Nano Energy. 2016, 21, 145–153.

[75] G. Sun, X. Zhang, R. Lin, J. Yang, H. Zhang, P. Chen, Angew. Chem. Int. Ed. 2015, 127, 4734–4739.

[76] Y. Xu, Z. Lin, X. Huang, Y. Liu, Y. Huang, X. Duan, ACS Nano. 2013, 7, 4042–4049.

[77] B. Anothumakkool, R. Soni, S. N. Bhangea, S. Kurungot, Energy Environ. Sci. 2015, 8, 1339–1347.

[78] Li. N, Huang. X, Zhang. H, J. Alloys Compd. 2017, 712, 194–203.

[79] C. Zhu, P. Yang, D. Chao, X. Wang, X. Zhang, S. Chen, B. K. Tay, H. Huang, H. Zhang, W. Mai, H. J. Fan, Adv. Mater. 2015, 27, 4566–4571.

[80] X. Xiao, X. Peng, H. Jin, T. Li, C. Zhang, B. Gao, B. Hu, K. Huo, J. Zhou, Adv. Mater. 2013, 25, 5091–5097.

[81] W. Zilong, Z. Zhu, J. Qiu, S. Yang, J. Mater. Chem. C. 2014, 2, 1331–1336.

[82] X. Lu, M. Yu, G. Wang, T. Zhai, S. Xie, Y. Ling, Y. Tong, Y. Li, Adv. Mater. 2013, 25, 267–272.

[83] B. Yao, L. Yuan, X. Xiao, J. Zhang, Y. Qi, J. Zhou, J. Zhou, B. Hu, W. Chen, Nano Energy. 2013, 2, 1071–1078.

Chapter V: Conclusions and Perspectives

V.1 Conclusions

Electrochemical energy storage devices, particularly flexible micro-supercapacitors (MSCs), are increasingly recognized as critical components for powering next-generation flexible electronics, wearable devices, and integrated self-powered systems. Nevertheless, achieving high energy density, flexibility, and stability remains challenging. This thesis addresses these challenges through innovative fabrication approaches based on laser-induced graphene (LIG) as conductive three-dimensional porous frameworks, combined with advanced functional nanomaterials to enhance electrochemical performance.

Specifically, for the first project (**Chapter III**), a facile, programmable, and scalable fabrication strategy combining laser patterning with mask-assisted spray coating of additive-free MXene inks was developed. The LIG electrodes were precisely patterned on polyimide substrates, exhibiting excellent electrical conductivity and mechanical flexibility. Few-layer $Ti_3C_2T_x$ (MXene) nanosheets were deposited onto LIG electrodes via spray coating without additives, significantly enhancing electrochemical charge transport. The optimized symmetric LIG-MXene micro-supercapacitor demonstrated remarkable electrochemical performance, with an areal capacitance of 43.80 mF cm^{-2} and energy density reaching 2.103 μWh cm^{-2}. Moreover, this method proved highly advantageous in terms of simplicity, scalability, and reproducibility, requiring only a minimal quantity of MXene material to achieve high capacitance. However, the inherent limitation of symmetric MSC configuration constrained the operational voltage window

and, consequently, the achievable energy density. Additionally, the spray-deposited MXene nanosheets, primarily bonded through physical adsorption onto the LIG scaffold, exhibited limited flexibility and long-term cycling stability under mechanical deformation.

Building upon the first project, the second project (**Chapter IV**) aimed to substantially improve MSC performance by fabricating asymmetric MSCs and integrating defect-engineered nanomaterials. Specifically, electrochemical deposition was employed to fabricate CoNi layered double hydroxides enriched with hydrogen vacancies (CoNi-$LDH_{(v)}$) as the cathode material, providing excellent pseudocapacitive properties and extending the potential window to 0–1.0 V (vs Ag/AgCl). Additionally, by carefully selecting and depositing different pseudocapacitive materials onto the anode and cathode, the resulting asymmetric micro-supercapacitor (AMSC) featured significantly expanded voltage windows (up to 1.8 V) and superior energy density. The deposition conditions, including deposition cycles and time, were optimized to achieve the best charge-matching configuration between electrodes. Due to the electrochemical deposition approach, the deposited materials exhibited robust mechanical and chemical interactions with the LIG substrate, ensuring superior flexibility, excellent bending stability, and outstanding cycling performance over extended operation periods. This strategy effectively overcame the limitations identified in the first project, successfully achieving the intended design objectives.

Collectively, this thesis presents a systematic exploration of scalable, versatile, and efficient fabrication strategies for flexible MSCs, demonstrating significant advances in electrochemical performance, mechanical robustness, and practical applicability. These

findings provide valuable insights and technical foundations for future innovations in flexible, high-energy-density electrochemical storage devices, facilitating their integration into advanced flexible and wearable electronic systems.

V.2 Perspectives

Despite the noticeable progress in the design and fabrication of high-performance flexible micro-supercapacitors, significant challenges and opportunities remain to achieve industrial applications. To further enhance the development of flexible MSCs, perspectives for future research directions are outlined below.

From the perspective of electrode material design and mechanistic understanding: Current insights into energy storage mechanisms primarily focus on conventional capacitors and pseudocapacitive materials. There remains substantial room for the exploration of new composite materials and their synergistic effects, particularly regarding defect engineering and interface optimization. Advanced characterization techniques such as in-situ/operando spectroscopy (Raman, XPS, FTIR) and electron microscopy (TEM) combined with theoretical modeling (e.g., density functional theory) are crucial to elucidate the fundamental mechanisms governing charge storage and degradation processes at the nanoscale. This will facilitate targeted material engineering to improve the electrochemical performance and mechanical robustness of flexible MSCs.

From the industrial application perspective: Firstly, achieving large-scale and reproducible fabrication processes with consistent performance remains a critical challenge. Future studies should focus on refining the scalable laser-processing and deposition techniques, optimizing parameters to enhance uniformity, yield, and

throughput, which are essential for commercial viability. Secondly, the integration of flexible MSCs into real-world applications, such as wearable electronics and flexible sensors, requires systematic research on advanced encapsulation and packaging technologies to improve environmental stability, mechanical robustness, and long-term reliability. Thirdly, the exploration of green and sustainable materials, such as biodegradable substrates and non-toxic electrolyte systems, should be pursued to ensure environmental compatibility and sustainability. Finally, integrating MSCs with other electronic components (e.g., solar cells, sensors, wireless communication modules) into fully self-sufficient and multifunctional systems presents a promising avenue for future innovation, necessitating interdisciplinary collaboration and technological advancement.

These research perspectives aim to guide future developments toward realizing highly efficient, sustainable, and commercially viable flexible MSC technologies for widespread practical applications.

Publications

1.Zhihao Wu[#], Xiao-Lan Feng[#], Yong-Xiang Qu, Li-Xiu Gong, Kun Cao, Guo-Dong Zhang, Yong-Qian Shi, Jiw-Feng Gao, Pingan Song, Long-Cheng Tang*. Silane modified MXene/polybenzazole nanocomposite aerogels with exceptional surface hydrophobicity, flame retardance and thermal insulation, **Composites Communications**. 2023, 37, 101402.

2.Zhihao Wu, Min Li*, Guoxi Luo, Guodong Zhang, Longcheng Tang, Sabine Szunerits, Rabah Boukherroub*. High-Performance Flexible Micro-Supercapacitors Based on Laser-Induced Graphene Integrated with Hydrogen Vacancy-Rich CoNi Layer Double Hydroxide. (The manuscript has been submitted to **Journal of Energy Storage** and is currently under peer review**)**

3.Yu-Yue Wu[#], **Zhihao Wu**[#], Zuan-Yu Chen, Li-Dong Peng, Zi-Qi Guan, Yang Li, Cheng-Fei Cao, Guo-Dong Zhang, Jie-Feng Gao, Pingan Song, Yong-Qian Shi, Long-Cheng Tang*. Large-scale and facile fabrication of phenyl-containing silicone foam materials with lightweight, wide-temperature flexibility and tunable pore structure for exceptional thermal insulation, **Chemical Engineering Journal**. 2024, 492(15), 152183.

4.Guo-Dong Zhang[#], **Zhihao Wu**[#], Qiao-Qi Xia[#], Yong-Xiang Qu, Hong-Tao Pan, Wan-Jun Hu, Li Zhao, Kun Cao, Er-Yu Chen, ZhouYuan, Jie-Feng Gao, Yiu-Wing Mai, Long-Cheng Tang*. Ultrafast Flame-induced pyrolysis of poly(dimethylsiloxane) foam materials toward exceptional superhydrophobic surfaces and reliable mechanical robustness, **ACS Applied Materials & Interfaces**. 2021, 13, 23161−23172.